

eman ta zabal zazu



Universidad
del País Vasco

Euskal Herriko
Unibertsitatea

Optimisation of novel methods for pre-clinical imaging at 11.7T

Author: Géraldine PASTOR

Supervisor: Dr. Torsten REESE

Tutor: Dr. Eider SAN SEBASTIÁN

TESIS DOCTORAL

SAN SEBASTIÁN, 2017

AUTORIZACIÓN DEL DEPARTAMENTO

El Consejo del Departamento de QUIMICA APLICADA en reunión celebrada el día 30 de mayo de 2017 ha acordado dar la conformidad a la admisión a trámite de presentación de la Tesis Doctoral titulada: **“Optimisation of novel methods for pre-clinical imaging at 11.7 T.”**, dirigida por el Dr. Torsten Reese y presentada por Dña. GERALDINE PASTOR ante este Departamento.

En Donostia a 30 de mayo de 2017

VºBº DIRECTORA DEL DEPARTAMENTO

EL SECRETARIO DEL DEPARTAMENTO



Fdo.: Rosa García Arrona



Fdo.: José Manuel Seco Botana

**AUTORIZACION DEL/LA DIRECTOR/A DE TESIS
PARA SU PRESENTACION**

Dr/a. _____ TORSTEN REESE _____ con N.I.F. _____ X9233007W _____

como Director/a de la Tesis Doctoral: _____

Optimisation of novel methods for pre-clinical imaging at 11.7T

realizada en el Programa de Doctorado _____

Química Aplicada y Materiales Poliméricos

por el Doctorando Don/ña. _____ GÉRALDINE PASTOR _____,

autorizo la presentación de la citada Tesis Doctoral, dado que reúne las condiciones necesarias para su defensa.

En DONOSTIA a 24 de MAY de 2017

EL/LA DIRECTOR/A DE LA TESIS

Fdo.: Torb J

**AUTHORISATION OF THE THESIS TUTOR
FOR ITS PRESENTATION**

Mr/Ms. EIDER SAN SEBASTIAN LARZEBAL

In his/her capacity as Tutor of the Doctoral Thesis: _____

OPTIMISATION OF NOVEL METHODS FOR PRE-CLINICAL
IMAGING IN MRI

completed within the Doctoral Programme _____

QUÍMICA APLICADA / MATERIALES POLIMÉRICOS

by the PhD student Mr/Ms. GÉRDINE PASTOR,

and supervised by Dr.

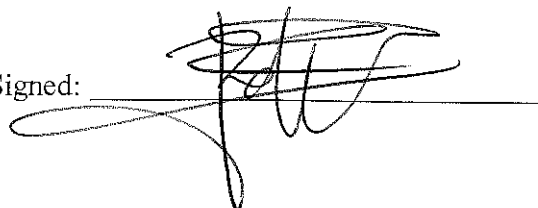
TORSTEN REESE

hereby authorises the presentation of the aforementioned Doctoral Thesis, given that it fulfils the conditions necessary for its viva.

In DONOSTIA on 25 of MAY, 2017

THE THESIS TUTOR
EIDER SAN SEBASTIAN

Signed: _____



ACTA DE GRADO DE DOCTOR O DOCTORA
ACTA DE DEFENSA DE TESIS DOCTORAL

DOCTORANDA DOÑA: Géraldine Pastor

TITULO DE LA TESIS:

Optimisation of novel methods for preclinical imaging at 11.7T

El Tribunal designado por la Comisión de Postgrado de la UPV/EHU para calificar la Tesis Doctoral arriba indicada y reunido en el día de la fecha, una vez efectuada la defensa por el/la doctorando/a y contestadas las objeciones y/o sugerencias que se le han formulado, ha otorgado por _____ la calificación de:
unanimidad ó mayoría

SOBRESALIENTE / NOTABLE / APROBADO / NO APTO

Idioma/s de defensa (en caso de más de un idioma, especificar porcentaje defendido en cada idioma):

Castellano _____

Euskera _____

Otros Idiomas (especificar cuál/cuales y porcentaje) _____

En _____ a _____ de _____ de _____

EL/LA PRESIDENTE/A,

EL/LA SECRETARIO/A,

Fdo.:

Fdo.:

Dr/a: _____

Dr/a: _____

VOCAL 1º,

VOCAL 2º,

VOCAL 3º,

Fdo.:

Fdo.:

Fdo.:

Dr/a: _____

Dr/a: _____

Dr/a: _____

EL/LA DOCTORANDO/A,

Fdo.: _____



Acknowledgements

First of all, I would like to thank all the people who have helped and encouraged me during my doctoral study.

I would especially like to express my sincere gratitude to my supervisor, Dr. Torsten Reese, for his mentorship, his never-fading interest in my work, and his support during these years. I am grateful for the many learning and studying opportunities he offered me. I would also like to thank my tutor from the University of Basque Country, Prof. Eider San Sebastian, for her benevolence and approachability.

I would like to deeply thank Dr. Daniel Padro, whose advices and encouragement helped me immensely during my doctoral study; Dr. Pedro Ramos-Cabrer to share his experiences with me; Dr. Sandra Plaza-García with whom it has been a real pleasure to work; and Eneko San Sebastian for his invaluable imaging analytic support.

I would also like to highlight the professionalism and support of Marta Beraza Cabrerizo and Dr. María Jiménez-González in conducting all the *in vivo* studies and for being there with me during every step of this emotional journey; I am also grateful to the Animal Facility and especially Ander Arrieta and Ainhoa Cano Garmendia for their unfailing support to animals.

Moreover, I would like to thank the president of my PhD committee, Prof. Jesús María Aizpurua Iparraguirre, and the secretary, Prof. María Iciar Martínez Galarza, for accepting this demanding role and agreeing to be part of my jury. I would like to thank Prof. Peter Morris CBE, Prof. Jesús Jiménez-Barbero and Prof. Mathias Hoehn for accepting to sit in the jury of this thesis. I am honoured and grateful for their time and effort.

I would also like to thank all the members of CIC biomaGUNE institute, which functions under the scientific leadership of Prof. Luis M. Liz-Marzán and Prof. Manuel Martín-Lomas. These years would not have been the same without all the other students, technicians and researchers I met. In particular, my thoughts go to Irati Markuerkiaga, Enrique Alonso Guerrero, Dr. Egoitz Conde Mendizabal, Ander Egimendia Tolaretxipi, and Dr. Susana Carregal Romero for their encouragement

and the pleasant working atmosphere they provided.

Enfin, je ne saurais oublier de remercier l'École de Lyon pour les interminables après-midi aux parcs de la BU et pour ne m'avoir jamais perdue; à la famille Dietrich pour m'avoir accueillie sur Biarritz; aux Guichard et Etcheverry sans qui ma vie au Pays Basque serait bien triste.

Une pensée à ma famille pour son soutien tout au long de ces années d'études et tout particulièrement à ma mère, ma soeur et mon père. A mes grand-parents si fiers de moi.

A Gloria y Bernard por ser familia en el País Vasco, con toda su delicadeza fueron capaces de poner interés en esta tesis y animarme cuando fue necesario.

Quelques mots enfin, pour Renaud qui fut tellement patient et compréhensif et qui a su m'encourager pour me permettre de mener à son terme cette aventure.

Contents

Summary	9
Resumen	17
Acronyms	23
1 Basic principles	27
1.1 Brief overview of Magnetic Resonance principles	27
1.1.1 Fundamental interaction between spins and magnetic field . .	28
1.1.2 Standard pulse sequences	32
1.1.3 Image characteristics	34
1.2 Gradient echoes sequences	36
1.2.1 Magnetic-field gradients	36
1.2.2 Signal localisation	37
1.2.3 Concise k-space formalism	38
1.2.4 Image weighting and contrast	39
1.2.5 Fast GE: the FLASH sequence	41
1.2.6 Echo Planar Imaging	42
1.3 Spin echoes sequences	44
1.3.1 SE sequences	44
1.3.2 Fast SE: the RARE sequence	45
1.3.3 Ultra-fast low-angle rapid acquisition and relaxation enhance- ment	46
1.4 The CIC biomaGUNE installation	49
1.4.1 Description of the installation	49
1.4.2 Animal preparation	53
2 Comparison of fast imaging methods for relaxometry	55
2.1 Implementation of fast imaging methods	56
2.1.1 Preparation experiments	56
2.1.2 Imaging sequences	57
2.1.3 Models	61
2.1.4 Data processing	62
2.2 Results	63
2.2.1 Agar phantom	63
2.2.2 Comparison of fast imaging methods for relaxometry	65
2.2.3 U-FLARE suitable for abdominal relaxometry <i>in vivo</i>	68
2.3 Discussion	69
2.4 Conclusion	72

3	High resolution MR Angiography of six rat strains	73
3.1	Magnetic Resonance Angiography	74
3.1.1	Time of flight technique	74
3.1.2	Studies of cerebral ischemia	76
3.2	Methods	76
3.2.1	<i>In vivo</i> model	76
3.2.2	Imaging methods	77
3.2.3	FRE simulation	78
3.2.4	Data processing	80
3.3	Results	80
3.4	Discussion	86
3.5	Conclusion	88
4	Functional brain imaging	91
4.1	Functional imaging	91
4.1.1	Neuro-imaging techniques	91
4.1.2	BOLD functional MRI	95
4.2	Differences between α and β glucose through an fMRI study	99
4.2.1	Coupling of neural activity, blood flow and energy metabolism	99
4.2.2	Method	101
4.2.3	Results	103
4.2.4	Discussion	106
4.3	Cinematographic FLASH	107
4.3.1	Method	108
4.3.2	Results and Discussion	111
4.4	Conclusion	118
	Bibliography	118

Summary

This thesis is based on the work performed at the Molecular Imaging Unit of CIC biomaGUNE (Donostia - San Sebastián, Spain), recognised by the Spanish Government as a unique scientific and technical infrastructure ('Infraestructura Científica y Técnica Singular' (ICTS)). The aim of this research project is to implement, optimise and develop magnetic resonance imaging (MRI) methods and protocols to improve the spatio-temporal resolution at high field strength.

A zoomed ultra-fast low-angle rapid acquisition and relaxation enhancement (U-FLARE) method was programmed and characterised. The method was validated in phantoms for relaxation time measurement. Additionally, zoomed U-FLARE was compared to echo planar imaging (EPI) and snapshot fast low angle shot (FLASH) to determine the relaxation time of the mouse kidney. Ultimately, the relaxation time for kidney, spleen, spinal cord, lymph nodes, muscle and subcutaneous tumour was successfully measured using the novel sequence.

Angiography protocol has been characterised to visualize the cerebral vasculature in the rat. Simulation of flow related enhancement (FRE) aided the optimisation of the protocol parameters to obtain angiograms within six minutes or up to a resolution of $62 \mu\text{m}$. The fast protocols were applied to determine the frequency of malformation in 45 Sprague Dawley rats. The ultra-high resolution protocols were suitable to obtain angiograms in six different rats strains as well as in rat subjected to cerebral ischemia.

Finally, functional MRI (fMRI) was used to study the influence of acute hypoglycaemia caused by the two main anomers of D-glucose. Difference in the blood oxygenation level dependent (BOLD) response upon somatosensory stimulation of the forepaw was observed. Surprisingly, it was observed that the hemodynamic response function (HRF) under medetomidine anaesthesia in a rat was delayed. Therefore, the cine FLASH method was utilised to analyse the HRF under high spatial and temporal resolution.

Nowadays, various distinct magnetic resonance (MR) techniques are available, which provide unique and non-invasive measurements for studying anatomy, basic functions of the body and diseases. **Chapter 1** gives a general introduction of MR

principles and describes the nuclear magnetisation as a function of time. An augmentation of the magnetic field strength increases the MR signal, allowing the use of pulse sequences to obtain high spatio-temporal resolutions.

Within the chapter, a standard MR imaging terminology has been introduced and defined. To help understand of the subsequent chapters, a special focus is laid on basic and fast imaging pulse sequences like gradient echo (GE), spin echo (SE) and EPI. A brief description of our high field installation has also been provided. Finally, as animal studies are indispensable for this work, general aspects applied for all *in vivo* studies have been discussed.

Chapter 2 emphasizes the advantages of fast SE sequences when using a high field system. A wide range of applications of U-FLARE method has been previously described in the literature. The imaging protocol can be adapted to acquire multiple parameter imaging, relaxation time, chemical-shift imaging, diffusion, etc. This in turn offers the possibility of obtaining multi-parameter maps, using exactly the same imaging protocol. The U-FLARE sequence can obtain high resolution images in a single shot. If the magnetisation is prepared from only a part of an object, the imaging matrix can be reduced. By zooming in, the signal potentially arising from outside of the area of interest is unaffected, thus severe motion artefact might be avoided. Examples of mapping relaxation times, T1 and T2, are presented in this chapter.

A zoomed extension of U-FLARE has been developed and utilised to rapidly map the relaxation time on a pixel-by-pixel distribution. The U-FLARE method is robust and does not require slice-selective shimming or pre- or post-processing. This method is remarkable for its insensitivity to susceptible artefacts and its high signal to noise ratio (SNR). The newly adapted zoomed U-FLARE sequence was then compared to standard EPI and snapshot FLASH methods. For the comparison, the measurement of relaxation times in agar phantoms and in *in vivo* mouse kidney were chosen. Advantages and disadvantages of the individual methods with respect to temporal and spatial resolution have been discussed.

For T1 measurements, a series of different T1 weighted images were acquired. Using this approach, fitting the data on a pixel-by-pixel basis yielded the relaxation maps. Zoomed U-FLARE utilises multiple inversion pulses whereby EPI and snapshot FLASH acquired the complete set of image following a single inversion. Thus, zoomed U-FLARE acquired the data more slowly than EPI and snapshot FLASH but with higher precision. Snapshot FLASH has a lower SNR when compared to

the zoomed U-FLARE sequence and EPI. The general advantage of the sequence over EPI is based on the fact that the imaging readout is sensitive to T2 rather than T2* ($T2^* < T2$). At high field, EPI is sensitive to B_0 heterogeneities. In fact, EPI is prone to a variety of artefacts like signal loss and geometric distortion. Moreover, the intra subject variability in the measurement of relaxation times is higher with the snapshot FLASH and EPI sequences than with the implemented zoomed U-FLARE sequence.

For T2 relaxation, the repetition of a single image with an increasing echo time (TE) enables the detection of the T2 relaxation time course. Importantly, both zoomed U-FLARE and EPI have relatively long minimum echo times. The achievable minimum TE for EPI and U-FLARE is most likely too long to separate relaxation times for intracellular and extracellular compartments. We acquire all TE increments with EPI in a single shot; eight times faster than U-FLARE. This leads to an inflexible TE spacing. The saved time can thus be used to either accumulate data to yield superior SNR or to segment the acquisition protocol to reduce the B_0 sensitivity of EPI at high field.

A high SNR in U-FLARE was achieved by reducing the spectral width leading to longer imaging time. Thus, blurring artefacts are evident in the phase-encoding direction. Furthermore, the current implementation of the zoomed-U-FLARE sequence is imaging a single slice. Using repeated acquisitions of different slices to cover the complete region of an organ would require an imaging time comparable to that of high-resolution contrast scans, and the temporal spatial advantages of this method would no longer exist.

This study demonstrates that the zoomed U-FLARE sequence offers a viable alternative to standard protocols for very fast mapping of the relaxation parameters *in vivo* at high field. Applications of abdominal imaging in a murine cancer model with good anatomical resolution are shown. Relaxation times of kidney (cortex and medulla), spleen, spinal cord, lymph nodes, muscle and subcutaneous tumour have been reported. In the future, this method might be used to characterise novel contrast agents for *in vivo* applications.

In **chapter 3**, a general protocol of three-dimensional time of flight (TOF)- magnetic resonance angiography (MRA) has been established to visualize non-invasively the cerebral vasculature in six different rat strains. The visualisation of the vascular structure is simply based on differences between in-flowing blood into the imaged slice (or slab) and the stationary tissue. TOF-MRA is sensitive to several factors

like the flow velocity, T1 and T2 of the blood and tissue, geometry settings like slice orientation and slab thickness, and pulse sequence settings like repetition time (TR) and flip angle. The study was initiated by the fact that at 11.7T, an improved contrast in TOF-MRA might be achievable due to the higher T1 relaxation time of the brain signal.

Several imaging protocols of 3D flow compensated gradient-recalled echo sequence were utilized to evaluate the influence of the parameter settings on the spatial and temporal resolution. FRE simulations highlight the importance of the selection of the flip angle and on the TR. The center of the field of view (FOV) can be adjusted to yield the highest contrast to noise ratio for a specific vessel close to the edge of the excited slab. If the MRA acquisition protocol centres a suitable FOV at the bregma as anatomical reference, all major brain arteries of the rat can be visualized. A nominal flip angle of 30 degree can be used to visualize distal branches of the posterior, anterior and middle cerebral arteries. Total imaging times ranged from 6 to 98 min for a 3D data set. Visualization of arterial trees within the cerebellum required special attention, as the lower flow velocities of the vertebral/ basilar arteries versus the carotid arteries has a strong influence. Thus, depending on the application and the desired spatio-temporal resolution, a wide range of scan protocols is available. Additionally, the visualization of the cerebral arteries was simplified and improved by removing extra-cranial vessels prior to the calculation of maximum intensity projection to obtain the angiograms.

The characterised TOF-MRA protocols are suitable to be used without a contrast agent, to produce high-resolution angiograms at 11.7T. Flow compensated angiograms of Sprague Dawley, Wistar Kyoto, Lister Hooded, Long Evans, Fischer 344 and spontaneous hypertensive rats strains were obtained with a resolution of up to $62 \mu\text{m}^3$. Smaller vessels branching off from the circle of Willis were also successfully identified. The dependence on the in-flow delay appears almost similar in all rat strains. Additionally, the MR protocol was then applied to obtain high-resolution angiograms to an experimental stroke model of 60 minutes transient middle cerebral artery occlusion (MCAO). Smaller vessels could be identified despite the occurrence of a large oedema 24 hours after the onset of stroke. Roughly 13% of our Sprague Dawley rats had a 'double branched' MCA, estimated by using a lower resolution TOF-MRA protocol in a large set of animals. Thus, the method is suitable to successfully detect one source of variability in the cerebro-vasculature subjected to transient MCAO. This finding might lead to a refinement in the study design to aid the development of novel therapeutics.

Chapter 4 discusses the functional imaging studies that have been performed in animals anaesthetized with medetomidine together with adequate isoflurane concentration and gas flow. This anaesthetic protocol is suitable for recovery anaesthesia required for future longitudinal studies. For fMRI studies, standard pulse sequences were adapted and modified to synchronise the timing of the data acquisition and peripheral electrical stimulator. In the future, these MR protocol implementations should serve as a suitable baseline to inspire mechanistic studies in naive rats, study drug action and will help in investigating long term neuroplasticity and recovery processes observed in ischemic animals.

A significant blood oxygenation level dependent (BOLD) response was observed during forepaw stimulation in the somatosensory cortex. The SE-EPI protocol was robust but the influence of anaesthesia, glucose level and other physiological parameters led to a variable response. The somatosensory cortex activation produced approximately an average 0.5% to 1.8% change in signal intensity.

Nevertheless, the setup was applied to study the BOLD response changes under the influence of acute hyperglycemia. At baseline, β -D-glucose is almost twice as abundant as α -D-glucose at anomeric equilibrium. Independently of the anomer administered, a large signal drop could be observed during injection. Following the injection of α -D-glucose, a larger BOLD response could be observed for around 30 minutes when compared to the administration of β -D-glucose. After the first anomer was injected, the average BOLD response is 40% higher than baseline following α -D-glucose injection, and 30% lower than baseline, following β -D-glucose injection. The difference is statistically significant ($p < 0.05$, Fisher test). The second injection of the alternative D-glucose anomer after 30 minutes showed a similar pattern. An injection of α -D-glucose showed an increased BOLD response in comparison to the integral response of the previous β -D-glucose injection. The anomer-specific trend was confirmed by the overall decrease in BOLD response when β -D-glucose was administered after α -D-glucose.

As indicated by the study of the glucose anomers, the peak onset of the HRF seems late when compared to previous reported values for the anaesthetized rat. Thus, to elucidate the finding, a new approach of the cine FLASH sequence was then implemented to estimate the HRF with an improved spatial and temporal resolution. Synchronised with repetitive electrical stimulations, the cinematographic FLASH sequence was acquired with a long TE (10 ms) and a spatial resolution of 250 μm per pixel. The temporal resolution between two images was 100 ms. Indeed, the onset of the HRF appears with a delay of a few seconds compared to

the start of forepaws stimulations. The amplitude of the response is not sustained during the complete stimulation duration. No clear signal undershoot could be detected following the stimulation. Thus, in collaboration with the imaging analysis platform, a single peak response was assumed and fitted by a gamma variate function on a pixel-by-pixel basis. A large variation in the single pixel HRF was calculated. Therefore, various parameter maps derived from the HRF were generated to visualize the spatial localization of the peak function characteristics. As the cine FLASH method is highlighting phase errors caused by movements or B_0 fluctuations, the time series data is often post-processed by filtering. In our experiments, the temporal signal stability was severely compromised by respiratory artefacts and the cold head induced vibrations, affecting the main field. As the application of low-pass and band-pass filters potentially has an influence on the shape of the HRF, a set of functions (Gamma, Gauss and Block) were simulated. Ultimately, if severe artefacts are present, it is advisable to choose the sequence parameter (*e.g.* TR) in such a way that they can be filtered without affecting the peak onset, shape, width and integral.

Resumen

Esta tesis presenta el trabajo realizado en la Unidad de Imagen Molecular del centro de investigación CIC biomaGUNE (Donostia - San Sebastián, España) reconocido por el Gobierno Español como una infraestructura científica y técnica singular (ICTS). Este proyecto de investigación se basa en la optimización y la caracterización de nuevos métodos rápidos de imagen por resonancia magnética (IRM) a 11.7 tesla (T), uno de los mayores intensidades de campo. Un nuevo método de adquisición de imágenes, al que denominamos zoom ultra-fast low-angle rapid acquisition and relaxation enhancement (U-FLARE), fue implementado y comparado con otros métodos con similares características ampliamente ya están probados como echo planar imaging (EPI) y fast low angle shot (FLASH). Así se logró obtener *in vivo* parámetros de relaxometría en la parte abdominal de un ratón. Luego, se adaptó métodos de angiografía de muy alta resolución para visualizar de manera inédita y no invasiva la vasculatura cerebral en cepas de ratas diferentes. Esta optimización se utilizó después en modelo de isquemias cerebrales. Y por último, se utilizó la resonancia magnética funcional a alto campo para investigar la forma de la respuesta hemodinámica. En un primer estudio, se investigó con una secuencia EPI la influencia de los dos principales anómeros de D-glucosa. En una segunda etapa, se desarrolló un método cinematographic FLASH mejorando la resolución espacial y temporal de métodos como EPI.

En el **capítulo 1**, se introducen de una forma general los fundamentos físicos de resonancia magnética a través de las ecuaciones de Bloch, que describen la trayectoria del vector magnetización en función de las constantes de relajación propias de cada entorno molecular. Se describe concisamente el equipo de IRM de alto campo magnético utilizado.

Los protocolos de adquisición siempre buscan el equilibrio entre tiempo de adquisición y calidad de la imagen (resolución espacial y relación señal/ruido). Aún hoy en día, se invierte mucho esfuerzo en desarrollar secuencias cada vez más rápidas que ofrezcan contrastes superiores o similares a los de las secuencias ya implementadas en resonancia magnética. Se considera 'ultra rápida' cualquier técnica que pueda generar una imagen con una resolución temporal por debajo del segundo. Se hizo un especial hincapié en la descripción de métodos de adquisición de imagen empleados a lo largo de los capítulos tales como los métodos versátiles y ultra rápidos U-FLARE, EPI and FLASH.

El **capítulo 2** presenta la implementación de la secuencia U-FLARE optimizada

a 11.7 T destacando la amplia versatilidad en cuanto a aplicaciones que ofrece dada su capacidad de medir diversos parámetros magnéticos como tiempo de relajación, difusión, desplazamiento químico etc. En este capítulo, se adaptó el protocolo de adquisición de imagen para medir tiempos de relajación, T1 y T2 .

En primer lugar, se desarrolló una secuencia zoom U-FLARE con objetivo de obtener rápidamente mapas de tiempo de relajación píxel a píxel. El método zoom se basa en una preparación espín-eco que consigue imágenes dentro de T2. La magnetización del campo de visión reducido se adquiere tras una sola excitación selectiva de un corte.

Entre las ventajas del método, destacando la posibilidad de adquirir imágenes de alta resolución en un tiempo relativamente corto, del orden de unos minutos, es destaca por su insensibilidad a variaciones de campo inducidas por cambio de susceptibilidad magnética así como su buena relación señal/ruido. El método es robusto y no requiere un 'shimming' adicional dentro del corte procesada tanta previo como posterior. Y pese a que U-FLARE presenta artefactos de borrosidad evidentes en la dirección de codificación de fase, la secuencia se ha utilizado para adquirir imagen de la parte abdominal de un modelo de cáncer ratón con una resolución espacial de 320 μm . Aunque la implementación actual de la secuencia zoom U-FLARE adquiere imagen de un único corte, ésta se podría modificar adquiriendo una serie de cortes que nos permitan cubrir un órgano en su totalidad. Sin embargo, esta modificación se repercutirá negativamente en la resolución temporal que sería entonces comparable a la obtenida mediante métodos clásicos de IRM de alta resolución. Se presenta la puesta en práctica metodológica a 11.7 T en un suplementario de datos.

En segundo lugar, se comparó la secuencia zoom U-FLARE con los métodos estándar EPI y snapshot FLASH resaltando las ventajas y desventajas en cuanto a la resolución temporal y espacial de dichos métodos a campos magnéticos altos. Se determinaron los tiempos de relajación longitudinal T1 and transversal T2 en fantomes de agar y después en un riñón de ratón *in vivo*.

En relación a la adquisición de mapas de relajación T1, la secuencia zoom U-FLARE ofrece la posibilidad de adquirir datos consiguiendo una mayor precisión y una mejor relación señal/ruido, per unidad de tiempo, que EPI y snapshot FLASH. No obstante, se logró un tiempo de lectura de imagen más largo com zoom U-FLARE que EPI or snapshot FLASH. Cabe destacar, la variabilidad en la medida de los tiempos de relajación fue mayor en las secuencias snapshot FLASH y EPI comparadas con la nueva secuencia desarrollada. La ventaja general de la secuencia

zoom U-FLARE sobre EPI se basa en el hecho de que la adquisición de ecos se realiza dentro de T2 en lugar de T2* ($T2^* < T2$). El tiempo de relajación T2* refleja la pérdida de señal causada por inhomogeneidades del campo B_0 , un factor esencial en el caso de altos campos magnéticos. Esta dependencia de T2* hace que las secuencias EPI sean propensas a presentar una variedad de artefactos en forma de distorsiones geométricas.

Referente a la adquisición de mapas de relajación T2, se puede adquirir EPI tras una única excitación ocho veces más rápido que la secuencia zoom U-FLARE. El tiempo ahorrado puede utilizarse para acumular datos dando lugar a una mejor relación señal/ruido o para segmentar el protocolo de adquisición, reduciendo así la sensibilidad del EPI en campo de alta potencia. Es importante destacar que tanto U-FLARE como EPI tienen tiempos de eco mínimos relativamente largos siendo el tiempo de eco mínimo es probablemente demasiado largo para estimar tiempos de relajación para compartimentos intracelulares y extracelulares. La implementación para adquirir mapas de relajación T2 con snapshot FLASH no es trivial y requiere especial atención fuera del ámbito de este trabajo.

Este estudio demuestra que la secuencia zoom U-FLARE ofrece una alternativa viable a los protocolos estándar para la obtención de mapas de parámetros de relajación *in vivo* a 11.7T particularmente en estudios longitudinales debido a su alta reproducibilidad. A continuación, se mostrarán los tiempos de relajación obtenidos por la secuencia zoom U-FLARE, distinguiendo riñón (corteza y médula), bazo, médula espinal, los ganglios linfáticos, músculo y tumor subcutáneo.

En el **capítulo 3**, se presenta un protocolo optimizado en 3D de angiografía por resonancia magnética (ARM) para obtener imágenes detalladas de los vasos sanguíneos cerebrales sin necesidad de usar ningún agente de contraste. A 11.7T, la señal vascular está favorecida con relación al tejido debido a la saturación de su señal. Así la magnetización longitudinal del tejido no tiene tiempo para relajarse y la señal se satura. Mientras que la sangre circulante que entra en el área explorada no se ha saturado, la magnetización longitudinal es máxima. El método consigue mejorar de forma general la señal del cerebro dado el aumento del contraste en time of flight (TOF) ARM en alto campo magnético.

Tras un proceso de optimización, los mejores resultados se obtuvieron con secuencias de gradiente eco en 3D con compensación de flujo hasta obtener una buena resolución espacial en las tres direcciones del espacio en un tiempo razonable. El protocolo de adquisición de ARM se centró en la bregma, una referencia anatómica

adecuada para todas las cepas de rata estudiadas. El centro del campo de visión se ajustó para visualizar la señal vascular de las principales arterias cerebrales posterior, anterior y media. Respecto a los parámetros de la secuencia, se escogió un ángulo de inclinación nominal de 30 grados para conseguir la mejor relación señal/ruido. Dependiendo de la aplicación deseada, el tiempo total de adquisición de imágenes osciló entre 6 y 98 minutos para un conjunto de datos 3D. Además, para obtener los angiogramas se mejoró la visualización de las arterias cerebrales mediante la eliminación de los vasos extracraneales antes del cálculo de maximum intensity projection (MIP).

Los angiogramas obtenidos por TOF 3D de las cepas Sprague Dawley, Wistar Kyoto, Lister Hooded, Long Evans, Fischer 344 y Spontaneous Hypertensive Rats fueron adquiridos sin el uso de agentes de contraste a 11.7T con una resolución isotrópica de hasta $62 \mu\text{m}^3$. Asimismo, se identificaron unas ínfimas ramificaciones de vasos del círculo de Willis. Se observó una dependencia del flujo muy parecida para todas las cepas de rata estudiadas. Posteriormente, se aplicaron estos métodos para obtener angiogramas de alta resolución de un modelo murino de isquemia cerebral por el método de middle cerebral artery occlusion (MCAO). El método ha sido exitoso en la detección de una fuente de variabilidad en la vasculatura cerebral en ratas Sprague Dawley sometidas a un MCAO transitorio. Aproximadamente el 13% de nuestras ratas presentaron una ramificación de la middle cerebral artery (MCA) influyendo el tamaño del infarto cerebral.

El **capítulo 4** expone aplicaciones de blood oxygenation level dependent (BOLD) a alto campo 11.7T en estudios de imagen funcional. La señal BOLD refleja las variaciones locales y transitorias en la cantidad de oxígeno transportado por la hemoglobina tras una actividad neuronal. Hoy en día, las técnicas de imagen ponderada $T2^*$ necesarias para BOLD siguen siendo un campo de investigación dinámico.

A continuación, se investigó la respuesta BOLD a estímulos cerebrales con la administración alternada de los dos anómeros principales de D-glucosa α - y β - D-glucosa. Los procedimientos se llevaron a cabo con ratas anestesiadas con medetomidina junto con un adecuado porcentaje de isoflurano. El protocolo espín-eco EPI utilizado fue robusto con una resolución spatial de $625 \mu\text{m}$ y una resolución temporal de 300 ms. Se observó una señal BOLD significativa en la parte anterior de la corteza somatosensorial, tras someter a los animales a estímulos eléctricos de las patas delanteras. Después, se inyectaron por vía intravenosa anómeros de D-glucosa que condujo a una respuesta BOLD diferente según el compuesto inoculado aunque la respuesta hemodinámica tuvo un perfil similar independientemente del anómero

inyectado. La activación de la corteza somato-sensorial produce entre un 0,5% y un 1,8% de cambio en la intensidad de la señal. La β -D-glucosa es casi dos veces más abundante que la α -D-glucosa en el equilibrio anomérico. Sin embargo, la α -D-glucosa parece ser más eficientemente metabolizada que la β -D-glucosa. Después de la inyección del anómero, la respuesta BOLD es un 30 % significativamente inferior ($p = 0,05$) tras de la administración de β -D-Glucosa que α -D-Glucosa. Tras una primera inyección de α -D-Glucosa, la siguiente inyección de β -D-Glucosa no tuvo un impacto significativo en la respuesta BOLD final.

En la última parte, se implementó un nuevo enfoque de la secuencia cine FLASH para estimar la respuesta BOLD tras una anestesia con medetomidina. La forma de una respuesta hemodinámica difiere en forma y magnitud entre sujetos y regiones cerebrales investigadas debido a factores como la estructura de los vasos sanguíneos, las diferencias en la actividad neuronal, las concentraciones de hematocrito... Se desarrolló una secuencia FLASH sincronizada con ciclos repetitivos de estimulación en modo de adquisición cine. Se obtuvo mapas de activación funcional con una mejor resolución espacial y temporal. El enfoque se basó en la sensibilidad de cine FLASH a la señal BOLD con tiempo de eco relativamente largo (10 ms) y con una alta resolución espacial, hasta 250 μm , y temporal de 100 ms.

Debido a esta alta resolución temporal, se detectó un retraso entre el estímulo y la señal BOLD que se extiende hasta varios segundos. Además conjunto a la señal BOLD, se detectó las frecuencias de la 'cabeza fría', de la respiración y del ciclo cardíaco traduciéndose en errores de fase de la señal. Sin embargo, el uso de filtros de bandas para aislar la señal BOLD fuera descartando ya que no contribuyen en una mejora del ajuste con una distribución Gamma. Este estudio permitió obtener mapas de diferentes parámetros hemodinámicos como el flujo sanguíneo cerebral (cerebral blood flow (CBF)) o el volumen sanguíneo cerebral (cerebral blood volume (CBV)), que son entre otros, parámetros cuantificables de la micro-circulación capilar cerebral. Finalmente, las mapas muestran unas respuestas hemodinámicas diferentes según los pixeles 'activados'.

Acronyms

ACA	anterior cerebral artery
AChA	anterior choroidal artery
AICA	anterior inferior cerebellar artery
ASL	arterial spin labeling
ATP	adenosine tri-phosphate
AUC	area under the curve
BA	basilar artery
BOLD	blood oxygenation level dependent
CBF	cerebral blood flow
CBV	cerebral blood volume
CCA	common carotid artery
CMR _{glc}	cerebral metabolic rates of glucose consumption
CMRO ₂	cerebral metabolic rate of oxygen consumption
CNR	contrast to noise ratio
CO ₂	carbon dioxide
CoW	circle of Willis
CPMG	Carr-Purcell-Meiboom-Gill
ECA	external carotid artery
EEG	electroencephalography
EPI	echo planar imaging
ETL	echo train length
FI	Fischer 344
FID	free induction decay
FLASH	fast low angle shot
fMRI	functional MRI
FOV	field of view
FRE	flow related enhancement
FT	Fourier transform
GE	gradient echo
GEFC	gradient echo flow compensated
HRF	hemodynamic response function
HTA	hypothalamic artery
ICA	internal carotid artery
IR	inversion recovery
LE	Long Evans
LH	Lister Hooded
LL	Lock Looker
M1	time to onset
MCA	middle cerebral artery
MCAO	middle cerebral artery occlusion

MEG	magnetoencephalography
MIP	maximum intensity projection
MR	magnetic resonance
MRA	magnetic resonance angiography
MRF	magnetic resonance fingerprinting
MRI	magnetic resonance imaging
MTT	mean transit time
NMR	nuclear magnetic resonance
PCA	posterior cerebral artery
PD	proton density
PET	positron emission tomography
PICA	posterior internal cerebellar artery
ppm	parts per million
PSF	point spread function
RARE	rapid acquisition with relaxation enhancement
RF	radio frequency
ROI	region of interest
rSE	refocused spin echo
SAR	specific absorption rate
SCA	superior cerebellar artery
SD	Sprague Dawley
SE	spin echo
SHR	Spontaneous Hypertensive Rats
SI	spectroscopic imaging
SNR	signal to noise ratio
SPECT	single photon emission computed tomography
SSFP	steady state free precession
StD	standard deviation
STE	stimulated echo
T	tesla
TCA	tricarboxylic acid
TE	echo time
TI	inversion times
TOF	time of flight
TR	repetition time
TTP	time to peak
U-FLARE	ultra-fast low-angle rapid acquisition and relaxation enhancement
WK	Wistar Kyoto

Introduction

Magnetic resonance imaging (MRI) is a medical diagnostic technique essential in the healthcare sector for the prevention, diagnosis and treatment of diseases and illnesses. A plethora of magnetic resonance (MR) techniques have been introduced to provide indispensable measurement abilities to study anatomy (skeletal system, vasculature) as well as functionalities of the human body (*e.g.* neuro-chemistry, perfusion and diffusion). MRI is still a hothouse for the development of new alternative methods with the most cost effective or highest achievable performance. New MR techniques are being developed and optimised to maximise desired factors such as sensitivity, and to minimise undesired ones such as the scanning time. This development has been possible due to advancements in the technique, including the increase in the field strength.

With the wide commercialisation of superconducting magnets, the strength of higher field is being continuously pushed. All MRI machines are calibrated in tesla (T), the unit of magnetic field's strength. In 1980, the highest field-strength magnet then available was a 1.5 T system. Nowadays, higher fields are more popular because of their increased sensitivity and resolution. In research laboratories, human studies have been performed at 9.4 T while animal studies have been performed at 21.1 T. In 2008, Center for Cooperative Research (CIC) biomaGUNE institute inaugurated the new Molecular Imaging Unit equipped with an ultra high field MRI of 11.7T . At the time, the 11.7T system that was installed was the third most powerful equipment in Europe, which was entirely dedicated to preclinical research.

The overall objective of this thesis is the designing of new sequences and the implementation of existing sequences in terms of signal to noise ratio (SNR), resolution and artefact reduction. Images obtained with a high resolution and an adequate contrast are indispensable for anatomical imaging as well as for *in vivo* functional applications. On the downside of an ultra-high field, problems such as spatial artefacts and field inhomogeneities are exacerbated due to a higher main magnetic field, and often need to be tackled with new or refined concepts. Indeed, it is not a trivial matter to obtain a satisfactory image quality with such systems. Artefact suscepti-

bility as well as high power deposition and severe field inhomogeneities might become a serious issue at high field strength. Various such problems will be addressed in this work and specific solutions will be proposed.

The basic principles of MRI have been introduced in the first chapter, along with a brief description of techniques applied in this thesis, such as gradient echo (GE), spin echo (SE) and echo planar imaging (EPI) . An improved method of U-FLARE is proposed in the second chapter and validated for relaxation time mapping at 11.7T. Snapshot fast low angle shot (FLASH) and EPI were also used to determine relaxation time in agar phantoms and in the mouse kidney. Advantages and disadvantages of the individual methods will be discussed with respect to temporal and spatial resolution, The third chapter focuses on ultra-high resolution magnetic resonance angiography (MRA). An optimization protocol was implemented and then employed in a stroke model. Finally, the fourth chapter is centred on functional MRI (fMRI) of rats anaesthetized with medetomidine. The metabolic efficiency of two anomers of glucose will be discussed. A cine FLASH method was implemented to study the blood oxygenation level dependent (BOLD) response for a high spatial and temporal resolution.

Chapter 1

Basic principles

1.1 Brief overview of Magnetic Resonance principles

The principle of nuclear magnetic resonance (NMR) was discovered simultaneously in 1946 by Purcell, Torrey and Pound at MIT (Cambridge), and Bloch, Hansen and Packard at Stanford University [1]. On these days, NMR spectra was recorded in a continuous wave mode as a purely physical experimentation to demonstrate that a nuclei within the same molecule absorbs energy at different resonance frequencies. Bloch was the first to describe the induced energy level difference of the nuclei by the external magnetic field. Spin echo was first detected in NMR by Hahn in 1950, and two years later, Carr produced a 1D-NMR spectrum. In 1966, NMR was revolutionized by Ernst and Anderson who introduced the combination of pulsed NMR with the Fourier transform (FT). From the 1960s, scientific literature has reported works on properties of water in biological tissues.

In the early 1970s, a major imaging application of NMR *in vivo*, namely MRI, is reported by Lauterbur who produced NMR images in 2D and 3D, using magnetic field gradients. At the end of the 1970s, Mansfield described the EPI technique as the earliest rapid MRI technique [2]. This new fast technique based on rapid oscillations of a magnetic field gradient provided scans in seconds rather than hours, and produced clearer images than Lauterbur had. Nowadays, EPI is widely used despite some severe disadvantages due to its strong sensitivity to field inhomogeneities.

In the middle of the 1980s, Haase et al. proposed the snapshot FLASH, a gradient echo method. The sequence uses a short repetition time combined with an optimise flip angle for spin excitation. Concurrently, Hennig et al. endeavoured to develop a new sequence, which was less sensitive to field inhomogeneities, and

discovered the technique for rapid acquisition with relaxation enhancement (RARE) sequence [3]. The RARE sequence encoded individually each spin echo following an excitation. The ultra-fast low-angle rapid acquisition and relaxation enhancement (U-FLARE) method is a single shot extension of RARE, and was initially published by Norris in 1991. Many other rapid imaging techniques have since been proposed.

The basic principles of MRI described in this chapter are selected to allow the understanding of the following chapters. For a broader overview, the reader might be redirected to some comprehensible and highly readable reference books [1][4][5][6].

1.1.1 Fundamental interaction between spins and magnetic field

Quantum mechanics

Magnetic resonance is based on the interaction of a nuclear spin with a static field B_0 . By convention, B_0 is defined parallel to the z axis. This work will focus on the hydrogen atom ^1H . The hydrogen atom is a single proton which has a property called spin, defined as a mass rotating with an angular momentum L and a magnetic moment μ . These two properties are linearly associated by:

$$\vec{\mu} = \gamma \vec{L} \quad (1.1)$$

with γ the gyromagnetic ratio (for ^1H , $\gamma = 42.58 \text{ MHz T}^{-1}$). In the absence of an external magnetic field, the nuclear magnetic moments are randomly oriented. When placed in a magnetic field, the nuclear magnetic moment aligns around B_0 . Then, the spin precesses at the Larmor frequency ω_0 :

$$\omega_0 = \gamma B_0 \quad (1.2)$$

For a proton with spin quantum number I equal to $1/2$ (figure 1.1), there are two energy configurations, a low energy state ($E_{-1/2} = -1/2 h \omega_0$) and a high energy state ($E_{1/2} = 1/2 h \omega_0$). The energy difference ΔE between the two states is proportional to B_0 and defined as:

$$\Delta E = E_{1/2} - E_{-1/2} = h \gamma B_0 = h \omega_0 \quad (1.3)$$

with h the Planck's constant ($h = 6.63 * 10^{-34} \text{ J s}$). The number of spins in the lower energy level N^+ slightly outnumbers the number of spins in the upper level

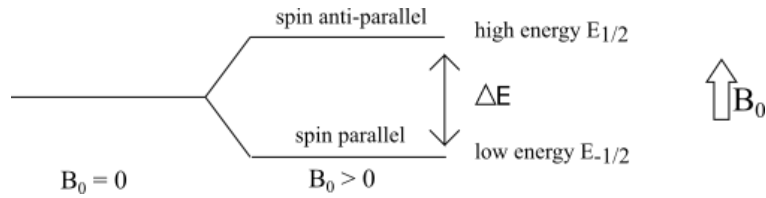


Figure 1.1: The effect of an external field B_0 on the energy levels of a proton. The two energy level states induced by B_0 are commonly referred to as parallel spin or spin up in the lower energy state, and anti-parallel spin or spin down in the higher energy state.

N^- at room temperature:

$$\frac{N^-}{N^+} = \exp\left(-\frac{\Delta E}{kT}\right) \simeq 1 + \frac{h \omega_0}{k T} \quad (1.4)$$

with k the Boltzmann's constant ($k = 1.38 \times 10^{-23} \text{ J K}^{-1}$) and T the temperature [K]. Due to this population difference, there is a net macroscopic magnetisation vector M_0 parallel to B_0 . At thermal equilibrium, M_0 is described by:

$$\frac{dM_z(t)}{dt} = 0 \quad M_0 = \sum_{i=1}^n \mu_i \quad (1.5)$$

NMR signal

To observe the nuclear magnetisation, the longitudinal magnetisation M_z has to be excited by a second magnetic field B_1 to create transverse magnetisation M_{xy} (figure 1.2). Oscillating at the Larmor frequency ω_0 , B_1 field is applied as a radio frequency (RF) pulse described by a pulse shape (amplitude and phase) and a duration t_p .

To simplify the complex motion of precessing spins, the rotating frame concept is often used [1]. The components of the magnetisation in the rotating frame are given by:

$$M'_z = M_z \quad (1.6)$$

$$M'_x = M_x \cos(\omega t) + M_y \sin(\omega t) \quad (1.7)$$

$$M'_y = M_y \cos(\omega t) - M_x \sin(\omega t) \quad (1.8)$$

The total magnetisation may be generalised as:

$$\frac{dM(t)}{dt} = \gamma B(t) M(t) \quad (1.9)$$

The temporal evolution of the transverse and longitudinal magnetisation is described

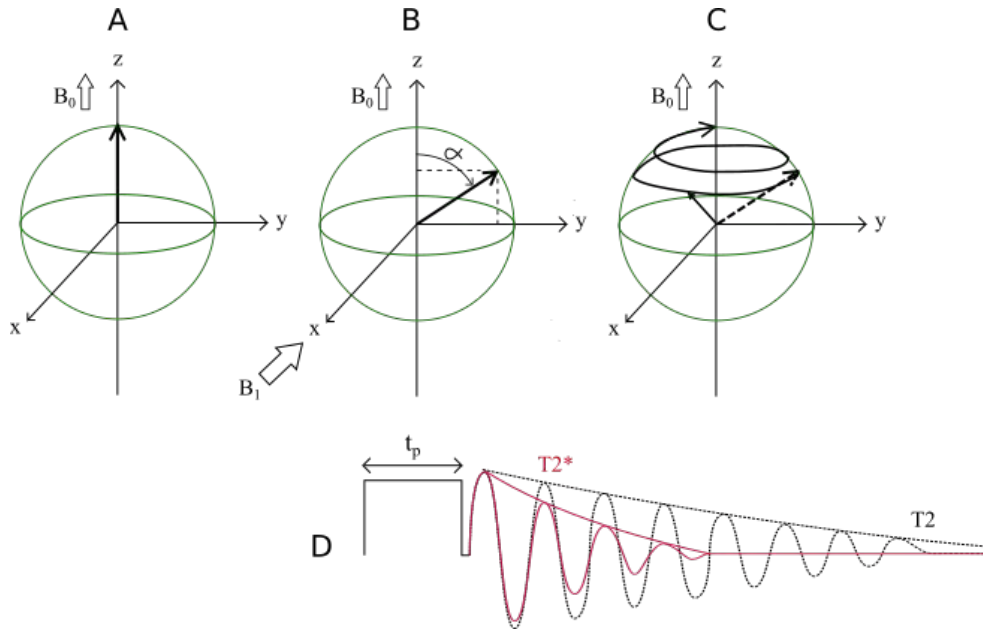


Figure 1.2: Generation of a magnetic resonance (MR) signal. At thermal equilibrium (A), the magnetisation vector is parallel to B_0 . For excitation (B), a short radio frequency (RF) pulse creates an orthogonal magnetic field B_1 which rotates the magnetisation M_z towards the transverse plane. The duration of the RF pulse t_p determines the flip angle α . For detection (C), the resonance frequency of M_{xy} is observed as a free induction decay (FID). As illustrated in (D), the transverse relaxation T_2 determines the relaxation decay. The signal might decay faster due to, for instance, field inhomogeneities with a time T_2^* .

by the Bloch equations:

$$\frac{dM_z(t)}{dt} = \frac{M_0 - M_z(t)}{T_1} \quad (1.10)$$

$$\frac{dM_x(t)}{dt} = -\frac{M_x(t)}{T_2} \quad (1.11)$$

$$\frac{dM_y(t)}{dt} = -\frac{M_y(t)}{T_2} \quad (1.12)$$

where T_1 and T_2 are the relaxation time. T_1 is the longitudinal relaxation time (also called spin-lattice relaxation time) and reflects the recovery of the magnetisation M_z . T_2 is the transverse relaxation time (also called spin-spin relaxation time) and reflects loss of phase coherence due to spin-spin interactions. M_{xy} might decay faster than T_2 due to factors such as local inhomogeneities and reported as T_2^* :

$$\frac{1}{T_2^*} = \frac{1}{T_2} + \frac{1}{A} \quad (1.13)$$

where A is the combination of external factors dependent of both system and sample [5].

Chemical shift

Until now, the description assumed only one type of nuclear spins. If protons associated with different molecules resonate at the same frequency ν because of a constant gyromagnetic ratio γ , NMR spectroscopy will not exist. The resonance frequency is sensitive to the chemical environment and is caused by electrons. The electrons thus shield the nuclei from the external magnetic field B_0 . As the electronic environment can be different within or between molecules, the small frequency difference can yield information about the structure of the molecule, resulting from the chemical shift δ . To be independent on the magnetic field B_0 , δ is defined in parts per million (ppm):

$$\delta = \frac{\nu - \nu_{ref}}{\nu_{ref}} * 10^6 \quad (1.14)$$

where ν is the frequency of the compound of interest and ν_{ref} is the frequency of the reference compound. In NMR spectroscopy, tetramethylsilane (TMS) is a generally accepted reference compound for protons with $\delta = 0$ ppm. *In vivo*, 1H NMR signal arising from tissues comes mainly from water and fat. Water shows a single resonance at 4.7-4.8 ppm, whereby the lipids in fat tissues have multiple lines due to different chemical groups. Additionally, the resonance frequency within molecules can have spin-spin coupling. Although NMR spectroscopy is an indispensable analytical tool for chemists [1][5], this aspect is out of the scope of this thesis.

Fourier transformation

As mentioned previously, the electromotive force detected is described in a time domain by the function $M_{xy} = M_x + iM_y$ (figure 1.3). The M_x and M_y components can be detected separately [1] and their projections are given by:

$$M_x(t) = M_0 \cos[(\omega_0 - \omega)t + \Phi] \exp\left(\frac{-t}{T2^*}\right) \quad (1.15)$$

$$M_y(t) = M_0 \sin[(\omega_0 - \omega)t + \Phi] \exp\left(\frac{-t}{T2^*}\right) \quad (1.16)$$

where Φ is the initial phase. Commonly, the analogue continuous signal received by the RF coil is converted to a digital signal. The time domain data $f(t)$ of multiple frequencies is difficult to interpret. Thus, the complex time domain data can be converted to a frequency domain data $F(\omega)$ [Hz] by a Fourier transform (FT) according to:

$$F(\omega) = \int_{-\infty}^{\infty} f(t) \exp(-i\omega t) dt \quad (1.17)$$

with $\exp(-i\omega t) = \sin(\omega t) + \cos(i\omega t)$.

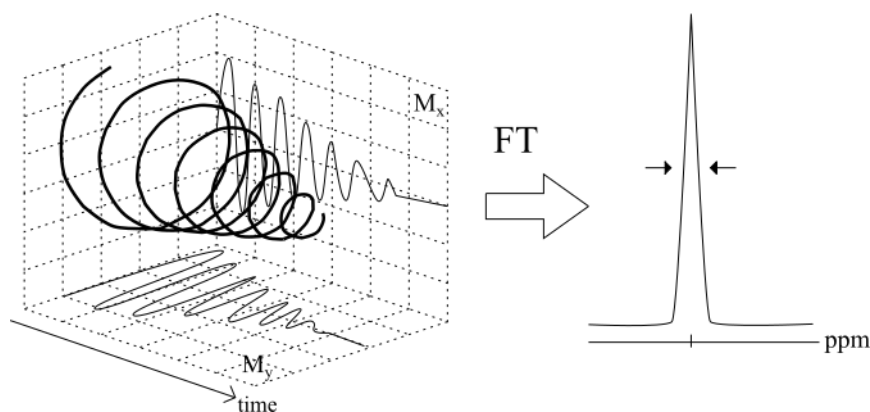


Figure 1.3: Following an excitation RF pulse, a free induction decay (FID) of the magnetization M_{xy} is completely described by two projections, M_x and M_y , on the x and y planes respectively. A Fourier transform (FT) of the time domain signal gives an NMR spectrum. The resonance frequencies are expressed in parts per million (ppm) (figure adapted from [1])

1.1.2 Standard pulse sequences

Free induction decay and T2*

The simplest MR experiment consists of an RF excitation pulse applied uniformly to the sample followed by data acquisition, known as free induction decay (FID). As illustrated in figure 1.2, the RF pulse flips the magnetisation M_z toward the transverse plane M_{xy} with the flip angle α defined as:

$$\alpha = t_p \gamma B_1(t) \quad (1.18)$$

where t_p is the pulse duration. Following the RF pulse, an electromotive force is produced by the transverse magnetisation and collected by a receiver coil. The transverse magnetisation will decrease with T2* relaxation due to a loss of phase coherence owing to field inhomogeneities.

Hahn echoes and T2

A pair of RF pulses creates a primary echo SE_{1,2} (figure 1.4). The excitation pulse, with a flip angle α_1 rotates the magnetisation M_z towards or into the M_{xy} plane. Therefore, a loss of phase coherence occurs due to field inhomogeneities. At a time τ_1 , an RF pulse α_2 rotates the magnetisation vector to refocus the inhomogeneities. A spin echo SE_{1,2} will arise at TE equals to $2\tau_1$. If the echo is followed by an additional RF pulse with a flip angle α_3 at the time τ_2 , different secondary echoes can be observed at distinct times as illustrated in figure 1.4. The individual echo amplitude depends on the flip angles and T2. Adapted from the original paper of Hahn [7], the expected amplitude of the signals are presented in table 1.1. A re-

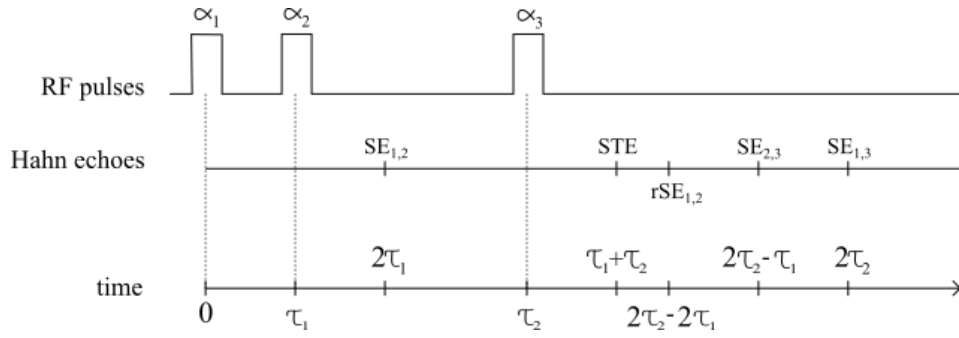


Figure 1.4: An experiment with three RF pulses with flip angle α_i may create three distinct spin echoes $SE_{1,2}$, $SE_{1,3}$ and $SE_{2,3}$, a refocused spin echo (rSE) and a stimulated echo (STE) (figure adapted from [7]).

Hahn echoes	time	$M(t)$
primary SE $SE_{1,2}$	$2\tau_1$	$M_0 \sin(\alpha_1) \sin^2\left(\frac{\alpha_2}{2}\right) \exp\left(\frac{-2\tau_1}{T_2}\right)$
stimulated SE STE	$\tau_1 + \tau_2$	$\frac{1}{2} M_0 \sin(\alpha_1) \sin(\alpha_2) \sin(\alpha_3) \exp\left(\frac{\tau_2 - \tau_1}{T_1} - \frac{2\tau_2}{T_2}\right)$
refocusing SE $rSE_{1,2}$	$2\tau_2 - 2\tau_1$	$-M_0 \sin(\alpha_1) \sin^2\left(\frac{\alpha_2}{2}\right) \sin^2\left(\frac{\alpha_3}{2}\right) \exp\left(\frac{2\tau_1 - 2\tau_2}{T_2}\right)$
primary SE $SE_{2,3}$	$2\tau_2 - \tau_1$	$M_{z(\tau_1)} \sin(\alpha_2) \sin^2\left(\frac{\alpha_3}{2}\right) \exp\left(\frac{2\tau_1 - 2\tau_2}{T_2}\right)$
primary SE $SE_{1,3}$	$2\tau_2$	$M_0 \sin(\alpha_1) \cos^2(\alpha_2) \sin^2\left(\frac{\alpha_3}{2}\right) \exp\left(\frac{-2\tau_2}{T_2}\right)$

Table 1.1: Expected amplitude of the signal for each echo created by the three pulse experiments illustrated in figure 1.4 [7].

focused spin echo (rSE) results from the magnetisation of $SE_{1,2}$ being recalled by the pulse α_3 . Additionally, a stimulated echo (STE) can be observed with a dependence of all three flip angles, T2 and importantly T1 between pulse α_2 and α_3 pulses.

To highlight differences in the spin-spin behaviour, a method sensitive to T2 called spin echo (SE) is available. The data might be sampled within a time series. The acquisition of single data point with different TE determined a T2 constant. The time between two excitation RF pulses is defined as the repetition time (TR). At the time nTE , the signal can be fitted by:

$$S(t) = S_0 * \exp\left(\frac{-TE}{T_2}\right) \quad (1.19)$$

where S_0 is the initial signal intensity. Data collection for more than one echo is possible by using multiple refocusing pulses after the single excitation. This aspect will be discussed further in the following section on Fast Imaging.

Inversion recovery and T1

To highlight the differences in the spin-lattice behaviour, a method sensitive to T1 called inversion recovery (IR) is available. The IR experiment consists of an initial inversion RF pulse (180°) to invert M_z to $-M_z$. Following the inversion, $-M_z$ recovers toward equilibrium. An excitation RF pulse is then applied in order to create transverse magnetization M_{xy} which is detectable by MR.

The amplitude of the signal is a function of the inversion times (TI) defined as the time between the inversion RF pulse and the excitation RF pulse. The signal can be fitted by:

$$S(t) = A - B * \exp\left(\frac{-TI}{T1}\right) \quad (1.20)$$

where A is the initial signal intensity created by the excitation RF pulse and B is the parameter evaluating the inversion.

1.1.3 Image characteristics

Differences in signal intensities

MR images should highlight a contrast differences between two tissues according to their relaxation properties as a function of B_0 [8]. The image contrast is a particularly complex function of instrumental and tissue relaxation parameters [9], diffusion or flow relaxation enhancement. Tissue contrast is created by adjustment of the sensitivity of the acquired signal by altering the acquisition parameters (*e.g.* flip angle, TE and TR) to differentiate various anatomical structures.

Proton density (PD) contrast is always present in MRI and refers to difference in signal intensity between tissues as a consequence of their relative number of protons per unit volume. Tissue with high proton density, such as brain tissue will appear brighter than tissue with low proton density as the cranial vault. To achieve only PD weighting, effects from T1 and T2 contrast must be minimised by using an appropriate choice of MR pulse sequence and adjusting their parameters.

A T1 weighted image demonstrates a contrast predominantly based on T1 differences. The time between two excitation RF pulses, TR, determines the amount of T1 longitudinal relaxation in the image according to the tissue (figure 1.5). For T1 weighting, the TR must be short. Similarly, the time between the excitation RF pulse and the acquisition sampling, TE, controls the amount of T2 weighting. For T2 weighting, the TE must be long concurrently with a TR long enough ($\simeq 5 * T1$)

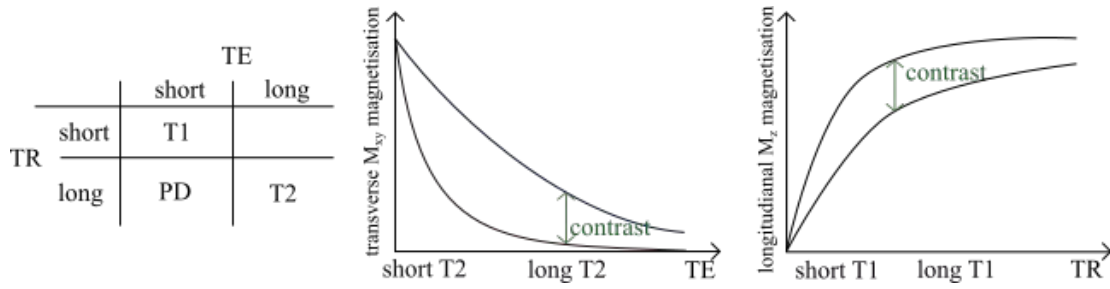


Figure 1.5: *In vivo* contrast can be visualised according to the differences in proton density (PD), and T1 or T2 relaxation of tissues. The choice of the echo time (TE) influences the contrast between tissues with different T2. Similarly, the repetition time (TR) influences the contrast for tissues with different T1.

If the requirement for full longitudinal relaxation is not fulfilled, some artefacts of blurring and smearing could occur.

Signal- and contrast-to-noise ratios

The signal to noise ratio (SNR) is a term commonly used when discussing image characteristics. This ratio calculates the difference between signal intensity in an area of interest and the background. The SNR increases linearly with the magnetic field strength B_0 [10] and can be defined as the intensity of the signal divided by the standard deviation (StD) of the noise:

$$SNR = \frac{S}{Std(N)} \quad (1.21)$$

where S is the signal and N is the noise. As a general assumption, bigger is the voxel, higher is the SNR.

The contrast to noise ratio (CNR) is defined as the difference between the SNR between two areas. CNR determines directly the ability to distinguish between areas with different signal intensities, that is to say, it has the sensitivity for detecting small signal changes.

Applications developed in this work relied on the advantage of high field strength for the improved SNR in order to reduce the voxel size. The following paragraph outlines different pulse sequence and methods to explain the basic principles of MR imaging.

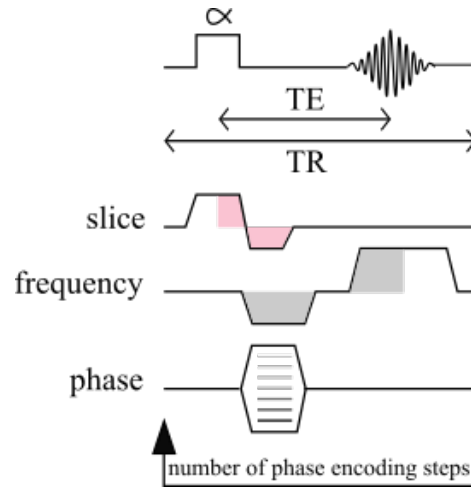


Figure 1.6: Gradient echo (GE) pulse sequence.

1.2 Gradient echoes sequences

A gradient echo (GE) pulse sequence consists of an RF excitation pulse, with a flip angle α , and two gradient pulses as displayed in figure 1.6. According to α , a part of the longitudinal magnetization M_z is converted to transverse magnetization M_{xy} . The transverse magnetisation is dephased by a magnetic phase gradient, and then rephased by an opposite gradient. At a time TE, a gradient echo signal is created.

1.2.1 Magnetic-field gradients

Imaging correlates MR signal with spatial locations, applying gradients through the object inside the magnet. Gradients G add an external magnetic field $B(r)$ according to a position r . Generated by RF coils within the bore of the magnet, the amplitude of this magnetic field gradient varies linearly with B_0 :

$$B(r) = B_0 + rG \quad (1.22)$$

Therefore, the resonance frequency ω becomes a function of the position r and might be rewritten as:

$$\omega(r) = \gamma B(r) = \gamma B_0 + \gamma rG \quad (1.23)$$

The strength of all gradients is null in the center of the magnet. Gradients can be modulated along the X, Y or Z axes, or any combination to achieve oblique slice orientation with the appropriate use of acquisition protocols. Signals with different frequencies correspond to different spatial position.

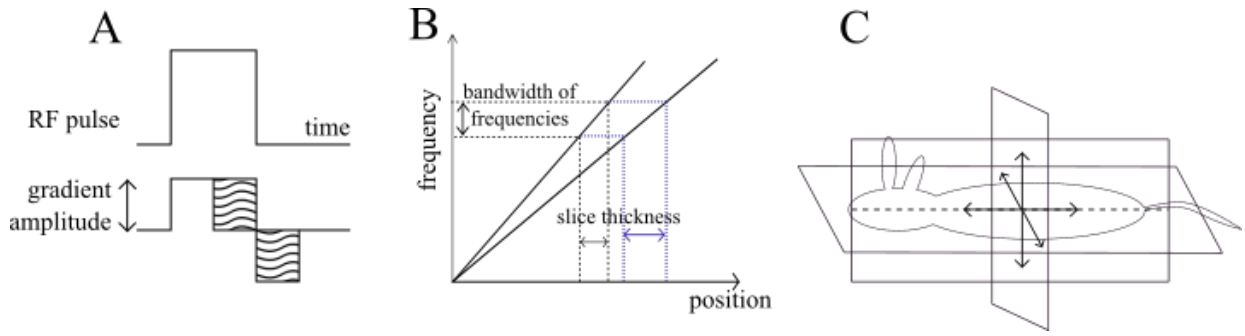


Figure 1.7: Slice selection can be achieved if a gradient is applied during an RF pulse (A). The slice thickness depends on the RF pulse bandwidth (which, in turn, depends on the shape and duration) as well as the gradient amplitude (B). The position of the slice is dependent on the transmitter frequency and on the strength. A gradient can be pulsed in any standard axes of the MRI magnet (C), or combined to achieve an oblique slice orientation (figure adapted from [4]).

1.2.2 Signal localisation

Slice selection

Slice selection can be achieved by using a gradient combined with an RF excitation to encode the location of the signal *e.g.* in the z direction. Each position r possess a specific resonance frequency. An RF excitation pulse with a certain bandwidth excite a selective frequency range $\Delta\omega$. The gradient is maintained during the RF pulse in order to excite the desired frequencies. The gradient strength determines a certain slice thickness and the slice position (figure 1.7 B) as:

$$G_z = \frac{\Delta\omega}{\gamma\Delta z} \quad (1.24)$$

To sum up, the slice thickness is determined by the magnetic field gradient strength and the bandwidth of the RF pulse. To achieve a thinner slice, either a stronger G can create a larger range of $\Delta\omega$ across the sample (steep slope of the slice gradient in figure 1.7) or a narrow bandwidth of the RF pulse (*e.g.* by increasing the pulse length) might be applied. The position of the slice is then determined by the magnetic field gradient strength and the frequency of the RF pulse. The Larmor frequency ω_0 leads to the possibility of tuning the RF pulse frequency to excite a slice at a desired spatial location. When the RF pulse frequency equals the Larmor frequency, spins in the center of the magnet are excited. To excite spins at a different position r'_z , the RF pulse frequency ω_z should be adjusted as:

$$\omega_z = \omega_0 + \gamma r'_z G_z \quad (1.25)$$

Frequency and phase-encoding

Once a slice has been selected, the signal can be encoded in 2D using a phase and a frequency gradient. The frequency encoding gradient, also called the readout gradient, corresponds to two gradient pulses, G_{freq} (figure 1.6). The first gradient G_{freq1} is applied prior to signal acquisition to generate a phase $\Phi(r)$. Spins at different spatial positions r rotate at different frequencies $\omega(r)$, which can be given as:

$$\omega(r) = \frac{\Phi(r, t)}{dt} \quad (1.26)$$

The second gradient G_{freq2} , which has an opposite sign of G_{freq1} , is active during signal acquisition. If the half of G_{freq2} compensates G_{freq1} , the maximum signal appears in the middle of the acquisition. Consequently, the acquired phase shift $\Phi(r)$ in the middle of the acquisition equals zero.

The field of view (FOV) is then determined by the gradient strength G_{freq} , the spectral width and the matrix. The frequency difference created by the gradients allows the spatial frequencies distribution of the signal and provides the spatial localisation of spins following an FT. In the presence of magnetic field inhomogeneity, an additional phase evolution is presented independently of gradients, leading to incorrect spatial position and geometrical distortions in the readout direction.

To obtain spatial information along the second dimension, the phase-encoding gradient can be used. A series of experiments have to be performed, changing the amplitude of gradient G_{freq} in the phase direction to encode M_{xy} as a function of position r . The constant increment of this encoding gradient determines the FOV. A FT converts the phase information of the signal into the spatial localisation of the spins distribution.

1.2.3 Concise k-space formalism

The k-space formalism reflects the spin density distribution under the influence of field inhomogeneities. An image is obtained after the FT of the data matrix of spatial frequencies. Each raw line corresponds to a single measurement of one phase-encoding step, but does not correspond with a line in the resulting MR image. In the k-space formalism, the abscissa axis k_x represents the frequency data, and the ordinate axis k_y represents the phase information.

Each created echo is assigned to a k-space line, which allows a high flexibility to reach the desired contrast and to minimize discontinuities in phase or ampli-

tude (figure 1.8 A and B). In linear encoding k-space scheme (figure 1.8 A), the k-space sampling starts sampling to one edge of the k-space. The frequency encoding gradient leads to the acquisition of the first echo along the k-space line k_{y0} . After the acquisition period, the frequency encoding increases or decreases k_{yi} linearly over time. K-space is then filled with spatially-encoded echoes according to parallel lines. With a linear k-space, the interval acquisitions of adjacent lines is the shortest, reducing potential image artefact, such as as blurring. Similarly, the centric encoding scheme starts the sampling of the data in the middle of the k-space. After the acquisition period, the frequency encoding alternates the k-space line $k_{y0} + 1$; $k_{y0} - 1$; $k_{y0} + 2$; *etc.* over time. Central phase-encoding may have larger blurring artefact in the phase-encoding direction.

Typically, when the k-space is filled, the scan is finished. An MR image is then created after a 2D-FT. In general, it can be said that the middle of k-space corresponds to the overall shape of the image. The central point of the k-space induces the contrast, and the edges of the k-space represent more detailed features in the final image.

1.2.4 Image weighting and contrast

The time taken to acquire the central point of the k-space is then fundamentally important to determine the contrast in the image. Thus, the image contrast is influenced by the effective TE of the pulse sequence, *i.e.* the interval between excitation RF pulse and the time at which the central k-space is acquired. Usually short for a GE sequence, the TE controls the amount of T2* decay that has occurred before the gradient echo is received by the coil. Further, as the TR controls the amount of T1 recovery that occurs before the application of the next RF pulse, a short TR usually produces a T1 weighting.

To make GE imaging more flexible, the flip angle α is usually reduced to less than 90° . The full recovery of the longitudinal magnetization occurs sooner with lower flip angle than with higher flip angle, and the TR can be shortened. For each combination of T1 and TR, an optimal flip angle called Ernst angle α_{Ernst} produces the highest signal amplitude. The transverse magnetisation M_{xy} is maximised for a given TR and a certain T1:

$$\cos(\alpha_{Ernst}) = \exp\left(-\frac{TR}{T1}\right) \quad (1.27)$$

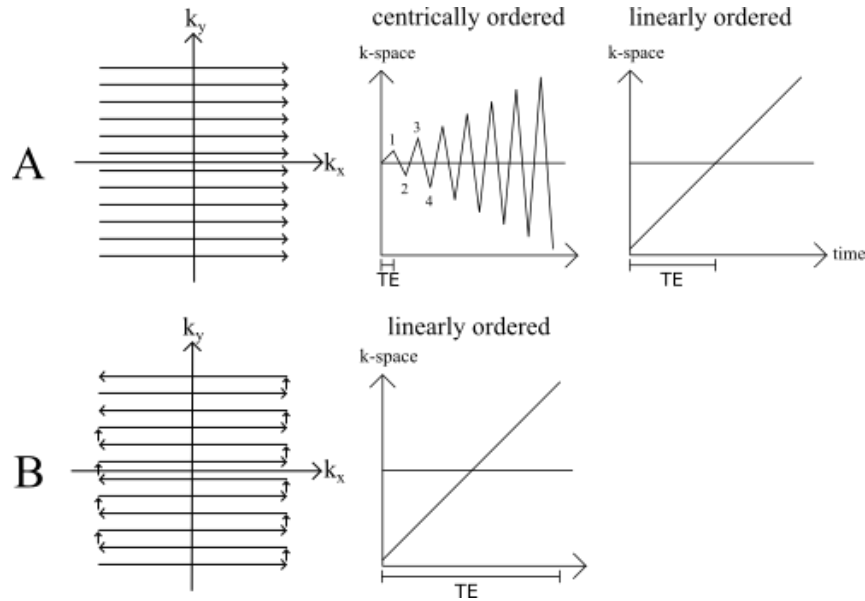


Figure 1.8: The uniform k-space trajectory for a gradient echo sequence is presented in (A). If the highest positive phase-encoding gradient is linearly decremented prior to subsequent repeated acquisition of frequency encoded profiles, linear phase-encoding is achieved. Alternatively, the central k-space line can be acquired first, with an alternating increase/decrease of the phase-encoding step to cover the k-space linearly. The signal intensity of the central k-space line determines the contrast. The signal intensity between the different k_y lines has an influence on the point spread function (PSF). Single shot sequences acquire the complete k-space through a single excitation. The uniform k-space sampling for echo planar imaging (EPI) is shown in (B). As the method consists of number of alternating frequency encoding gradients, the read-out direction changes accordingly. Thus, prior to Fourier transform for reconstruction, every second line k_y should be reversed.

To obtain a T1 weighted image, the difference in T1 is maximized while the differences in T2 or T2* of the tissues are minimized. To avoid full recovery, the flip angle is kept large and the TR, short, so spins are still relaxing when the next RF is applied. To minimize T2* differences, the TE should be short so that signal arising from fat or water should have time to decay. Similarly, to obtain a T2* weighted image, the difference in T2* is maximized and the difference in T1 is minimized. The TE should be long to maximize T2* decay. To minimize T1 recovery, the flip angle should be small and the TR long enough to permit full recovery. To obtain a PD weighted image, both T1 and T2* processes are minimized. The TE is short, the flip angle is small and the TR long enough to permit full recovery.

1.2.5 Fast GE: the FLASH sequence

Fast low angle shot (FLASH) method is one of the more employed sequences [11]. FLASH is a GE sequence with a low angle excitation RF pulse and a short TR, which produces an image fast. FLASH is a very versatile method; the schematic description is illustrated in figure 1.6. At high field, the biggest advantage of FLASH over other rapid pulse sequences is its reduced RF power deposition due to the low flip angle [12]. With a short TE ($TE < T2$) and long TR ($TR > T1$), the contrast is relatively independent of T1 and T2. If TE is longer ($TE > T2$), T2* contrast is dominant, whereas a moderate T1 contrast can be achieved with a relatively high excitation flip angle, a short TR ($TR < T1$) and a short TE ($TE < T2$).

Snapshot FLASH

Introduced at the end of the '80s, snapshot FLASH refers to the implementation of the original FLASH [11] that highly decreases the acquisition time [13]. The main applications for snapshot FLASH sequences are in abdominal imaging [14], cardiac studies [15] and brain imaging [16][17]. In the basic snapshot FLASH sequence, no spoiler or refocusing gradients are used. Performed by a slice-selective RF pulse has to have a very small flip angle of about 5° , TR might be drastically reduced in this method in comparison to T1. The signal amplitude can then be assumed constant over the time required to acquire all k-space lines. The intensity of each snapshot FLASH depends mainly on the amplitude of the GE acquired when the phase-encoding gradient is zero. Often, the phase-encoding gradient has a centric scheme [18].

A contrast in the image can be created by preparation experiments, which modifies the longitudinal magnetisation prior to the excitation of the snapshot FLASH

imaging. For example, snapshot FLASH can be easily adapted to measure T1 [19][14]. The snapshot FLASH sequence requires the magnetization to be prepared along M_z , in the longitudinal plane. A simple way to do this is to combine an inversion RF pulse with a single snapshot FLASH image with different delays. This approach will be discussed in the chapter 2.

Cinematographic FLASH

The movie data acquisition, called cinematographic FLASH or cine FLASH, was developed for the evaluation of cardiac motion [20] and functional imaging [21] to achieve higher temporal and spatial resolution [11]. Series of N images can be collected during a cycle and for each image, the same k-space line is acquired for every TR. The phase-encoding gradient is then incremented to cover an entire k-space. In order to do this rigorously, the collection of data must be synchronised to the physiological motion (respiratory and cardiac phase). This option will be used in the latest functional study presented in this work.

1.2.6 Echo Planar Imaging

Echo planar imaging (EPI) is one of the fastest MRI pulse sequences [2] (figure 1.9). EPI generates an image T2-T2* weighted, with a moderate T1 weighting, depending on the TR and the excitation flip angle. The contrast is determined by the effective TE, defined from the middle of the excitation RF pulse to the central k-space line. In EPI, the minimum effective TE achievable is fairly long. After an excitation RF pulse, the data is generally acquired during T2* and the amplitude of the corresponding echo is:

$$S_n(t) = S_0 \cdot \exp\left(\frac{-TE_n}{T2^*}\right) \quad (1.28)$$

with n being the echo index in the echo train and S_0 the initial signal amplitude.

Each echo is generated after either a gradient echo (GE-EPI, figure 1.9 A), or a spin echo (SE-EPI, figure 1.9 B). For GE-EPI, the echoes are formed under the envelope of an FID leading to a T2* contrast. For SE-EPI, the echoes are generated under the envelope of an SE typically by an excitation RF pulse of 90° and a refocusing RF pulse of 180°. When acquiring an image with a T2 contrast, SE-EPI is less affected by system imperfections such as magnetic susceptibility variations and magnetic field inhomogeneities, and presents less artefacts than the corresponding GE-EPI.

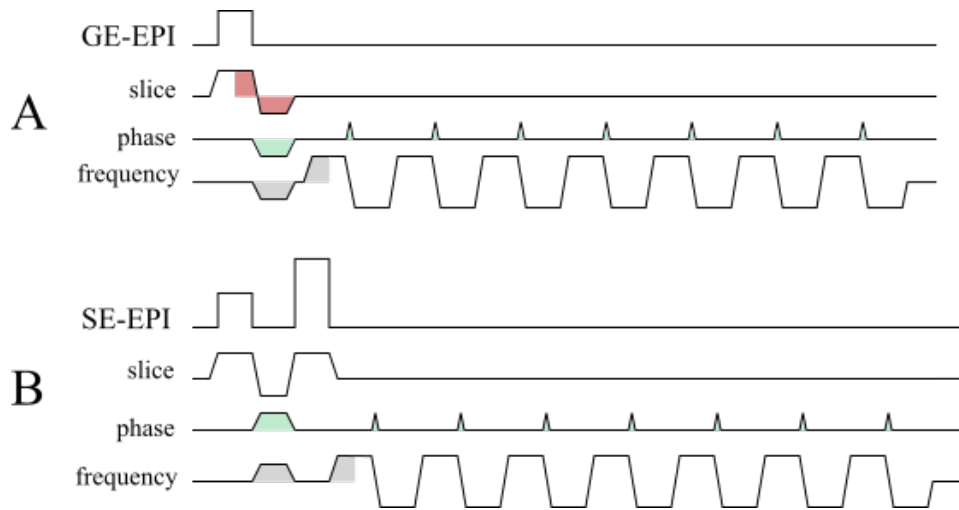


Figure 1.9: Blipped echo planar imaging (EPI) sequences, gradient echo (GE) EPI (A) and spin echo (SE) EPI (B).

EPI differs from conventional pulse sequences in that each echo is spatially encoded by a periodic inversion of the readout gradient after a single RF excitation. To accelerate data acquisition, EPI produces a series of GE with an oscillating readout gradient in the frequency encoding direction. In the phase-encoding direction, various options lead to different trajectories in k-space: a weak gradient of constant intensity, a blipped EPI option where the gradient is briefly switched on between acquisition periods while the read gradient changes polarity, or a spiral EPI option [22] where both phase and frequency gradients oscillate.

SNR depends on the transverse relaxation, the matrix, the spectral bandwidth and the flip angle. Thus a wide receiver bandwidth should be used for a decreased SNR as well as a reduced effect of T_2^* . A good compromise should be found between echo spacing, SNR and image artefacts of the increased gradient strength (*e.g.* distortion, signal loss and blurring). The effects of magnetic field inhomogeneity on the MR signal, such as signal loss and image ghosting, are prominent. EPI is subject to various artefacts, mainly geometric distortion caused by the frequency shift of the MR signal (tissue-air interfaces or metallic materials) and $N/2$ -ghost, caused by the alternating acquisition of k-space lines. EPI artefact-free combination of all echoes requires really fine adjustment.

To summarise, single-shot EPI provides excellent temporal resolution, high SNR and low spatial resolution. Single-shot EPI can be easily adapted for T_1 measurement: an inversion pulse followed by multiple EPI acquisitions. Successive EPI images might be acquired without interleaved delays between acquisitions; this modulation is then described by the Look-Locker theory [23]. The entire T_1 relaxation

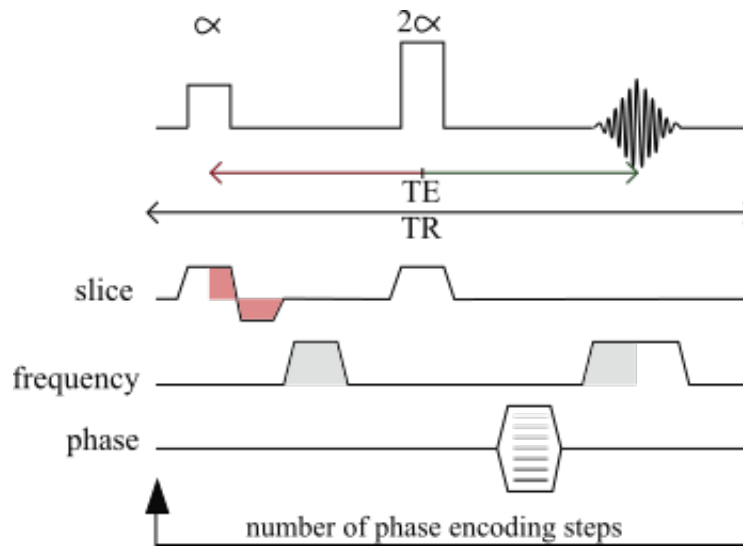


Figure 1.10: Pulse sequence of spin echo (SE) imaging

curve can be then acquired extremely rapidly with a multiple slices option.

1.3 Spin echoes sequences

1.3.1 SE sequences

The spin echo (SE) pulse sequence uses an excitation RF pulse α of 90° usually to flip the magnetisation into the transverse plane (figure 1.10). After the 90° RF pulse, spins start to dephase due to T_2^* and the signal decays. The refocusing RF pulse 2α (commonly 180°) rotates the magnetisation vector, from M_{xy} to $-M_{xy}$, to refocus the dispersing spins.

At a specific time TE, a signal with the maximal amplitude called spin echo is created. As spins are gradually coming back into phase, the signal builds step-by-step until it reaches a maximum at TE, when all the spins are in phase. As the dephasing is still an endless process, the signal decreases gradually. TR is the time between each excitation RF pulse while TE is the time between the 90° RF pulse and the middle of the acquired SE signal. The time required to dephase the spins between the 90° and the 180° RF pulse is equal to the time required to rephase the spins after the 180° RF pulse to the middle of the acquisition. Data acquisition for more than one echo is possible by using multiple refocusing pulse after the single excitation.

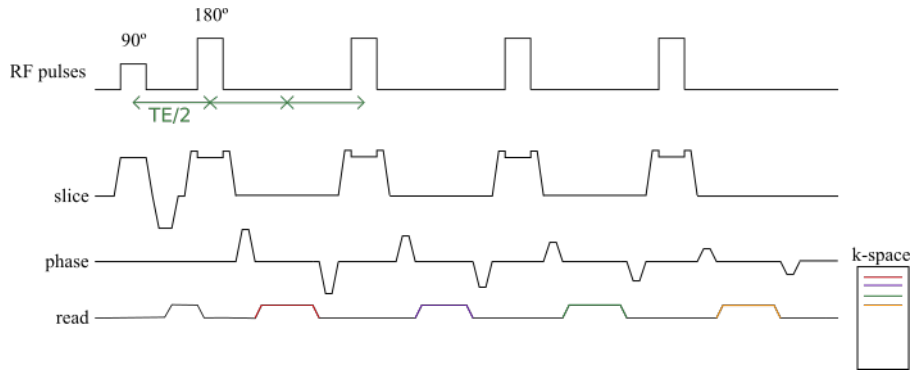


Figure 1.11: Pulse sequence of rapid acquisition with relaxation enhancement (RARE) imaging (figure adapted from [4]).

1.3.2 Fast SE: the RARE sequence

Rapid acquisition with relaxation enhancement (RARE) is a fast and versatile SE imaging sequence [24]. An RF excitation pulse is followed by a train of refocusing pulses to produce multiple RF spin echoes (figure 1.11). For multiple slice option, RF excitation pulse and refocusing pulses are both slice selective. Each echo is distinctly and independently phase-encoded [3]. Refocusing RF pulses are equally spaced in time. If the flip angle of every refocusing RF pulse is 180° , the SE signals are maximised and these amplitudes are:

$$S_n(t) = S_0 * \exp\left(\frac{-nTE}{T_2}\right) \quad (1.29)$$

with n being the echo number. Furthermore, the time interval between two adjacent refocusing pulses is defined as the echo spacing; echoes associated with refocusing pulses form the echo train length (ETL). As ETL is determined by the lifetime of the T_2 magnetization and the echo spacing, it is inversely proportional to the acquisition time. ETL should be maximised to improve the temporal resolution by shortening the echo spacing, reducing the slice profile by a smaller refocusing pulse width or by increasing the receiver bandwidth.

RARE might be accelerate by sampling only a fraction of the k-space data after each RF excitation pulse [25]. Each excitation can sample a segment of k-space and then the k-space lines can be interleaved. The RARE factor defined the number of echoes acquired after each excitation and measures the scan time acceleration. For example with a RARE factor of 4, the scan time is four times faster than a SE sequence with comparable parameters.

The timing of a RARE sequence should be correlated with the phase of the RF pulse to satisfy conditions known as the Carr-Purcell-Meiboom-Gill (CPMG) con-

ditions [26]. First, positions of the echoes should be very well defined within the pulse sequence to improve the robustness with respect to B_1 field non-uniformities. Refocusing RF pulses, which are evenly positioned, must be phase shifted by 90° with respect to the phase of the excitation RF pulse. The second condition requires the same phase for every signal at each temporal position. Between two consecutive refocusing RF pulses, the phase must be the same for all echoes.

A major disadvantage of RARE sequences is the requirement to encode a wide range of frequencies with different T2 weightings; as the spatial encoding should not show any discontinuities leading to multiple ghosts. In addition, practical attention such as RF power deposition, measured by specific absorption rate (SAR), might be taken into consideration. SAR is defined as the total RF energy dissipated in a sample. In RARE, SAR can be particularly high as multiple RF pulses are produced over a very short time. The use of lower refocusing flip angle is often required.

1.3.3 Ultra-fast low-angle rapid acquisition and relaxation enhancement

The ultra-fast low-angle rapid acquisition and relaxation enhancement (U-FLARE) technique has been published by Norris in 1991 [27] and is illustrated in figure 1.12. The U-FLARE sequence is comparable to the T2 weighted snapshot FLASH sequence discussed previously. While snapshot FLASH requires the magnetization to be prepared along M_z , the U-FLARE sequence requires the magnetization to be prepared in the M_{xy} plane [27]. The transverse magnetisation is then refocused by a train of slice selective low angle RF pulses. A more detailed description of each part of the sequence is then presented.

PREPARATION OF THE TRANSVERSE MAGNETISATION

First, the excitation pulse switches on the RF field modulation envelope for a short time, along the X axis. The magnetisation flips away from the direction of B_0 , in the M_{xy} plane according to the flip angle of 90° . The refocusing pulse rotates the magnetisation vector by 180° , from M_{xy} to $-M_{xy}$, to refocus the dispersing spin. The duration of the refocusing RF pulse must be minimum to enable a minimum TE. A slice selective excitation RF pulse is used with a slice selection gradient to produce an excited section. A supplementary gradient is needed for the selective excitation pulse to refocus the slice dispersion. The transverse magnetisation does not lie exactly along the M_{xy} axis in the rotating frame due to some phase dispersion across the slice caused by the slice selection gradient.

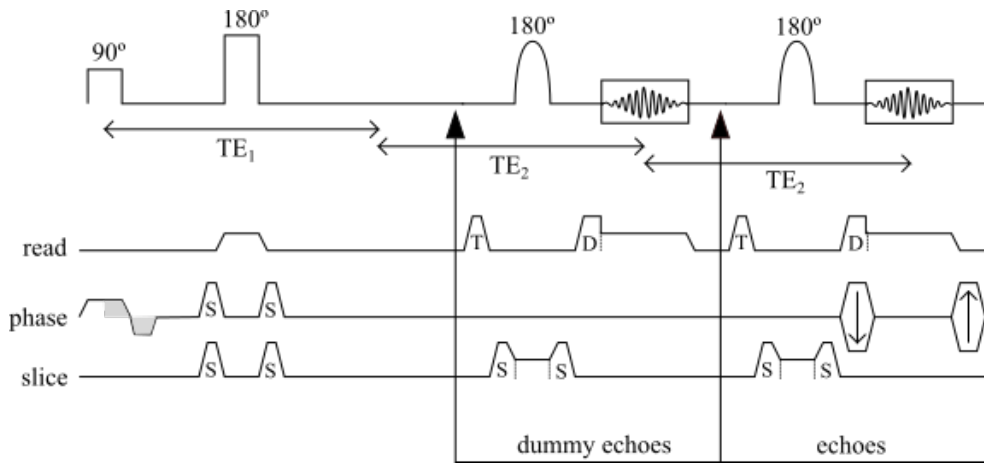


Figure 1.12: Zoomed displaced U-FLARE pulse sequence with a spin echo preparation experiment during TE_1 . The gradient D shifts one of the echo groups out of the acquisition window. The gradients labelled 'S' and 'T' are spoiler gradients and trim gradients, respectively.

U-FLARE sequence should image only the magnetisation prepared in the transverse plane [25]. Various SE, refocused and stimulated echoes are produced (table 1.1), which carry non-consistent spatial information due to the phase dispersion and leading to errors in the k -space data [24]. The contribution of these artefacts, which does not fulfil the CPMG conditions, should be spoiled off the acquisition window. The first option is to add the RF pulses phases in a destructive fashion; the second option is to use some crusher gradient as a correction gradient that preserves the desired signal while eliminating the unwanted by manipulating the signal's phase. A crushed gradient has two lobes with the same polarity, and as close to the RF pulse as possible to avoid diffusion weighted contrast: one immediately before a refocusing RF pulse and the other immediately after. It can be applied to any gradient axis without effecting on the longitudinal component of the magnetisation. As the left and right gradient have equal areas, the phase dispersion introduced by the left gradient is exactly cancelled by the right gradient. The right crusher is necessary to eliminate the unwanted signals, and the left crusher is needed to counteract the effect on the wanted signals.

ZOOMED U-FLARE

The zoomed U-FLARE sequence used in this work is a straightforward high resolution extension of the U-FLARE technique [27]. The implementation of the single-shot zoomed displaced U-FLARE sequence is illustrated in figure 1.12. Gradient combined with RF excitation are used for slice selection to encode the location of the NMR signal. An RF pulse turned on the Larmor frequency ω_0 is used concurrently with a slice selection gradient to produce an excited section. The field of

view (FOV) is selected when the resonance between the frequency of the RF pulses matches with the precession frequency of the tissue within a specific plane. Hence, the position of the FOV depends on the frequency of the RF pulses.

REFOCUSING THE TRANSVERSE MAGNETISATION

The spatial distribution is achieved by refocusing the transverse magnetisation. The slice thickness depends on the bandwidth of the RF pulse and the amplitude of the gradient section. The position of the slice depends on the frequency of the pulse. In the present implementation, eight dummy pulses preceded the acquisition of the image in order to allow echoes to equilibrate in signal intensity.

To minimise this T2 contrast, the sequence should start with the weakest phase-encoding gradient. Hence, a centric phase-encoding scheme is preferred [25]. After the slice gradient, the signal excited has to be encoded before the read of the signal. The phase-encoding gradient starts at zero phase encoding and then the strength and alternate polarity between two slices refocusing gradients increases. The phase-encoding gradient must be rewound between the end of data acquisition and the next refocusing.

DIFFERENT VERSION OF U-FLARE

The train of refocusing pulses generates two groups of echoes. The wide choice of using only one echo group has already been discussed for proton [28] and fluorine imaging [29] applications. Different variants of U-FLARE have been developed depending on the use of these two echo groups:

1. The phase variant version:

In the same acquisition window, both odd and even echoes are acquired with an arbitrary phase between the echoes [30]. To separate parities in the two echoes, a two-step phase cycle is used, and each parity is reconstructed independently to provide an odd and an even data set [25]. Signals from these two data sets can be added together to increase the SNR. The SNR is then reasonably high per unit of measuring time. The major drawback of this technique is the time consumed, because two complete scans are needed to finish a phase cycle and severe movement artefacts may arise.

2. The coherent version:

In this version, odd and even echoes are superposed in the acquisition window by careful adjustments in the sequence parameter. Their phase should be in harmony, and their temporal positions should necessarily coincide with careful adjustments of the sequence parameters. Any inconsistency in the echoes' pathways will cause signal cancellation, leading to ghosting artefacts and de-

creasing the SNR. Compared to the phase variant option, the SNR is increased by a square root of two.

3. The displaced version:

Either odd or even echoes are acquired in this version; the other echo group is shifted out of the acquisition window by an appropriate gradient scheme to surmount the obligation to satisfy the CPMG conditions. Compared to the phase variant option, the SNR is reduced by a square root of two. For *in vivo* application, the displaced version presents higher reproducibility and was therefore implemented in the next chapter.

For the displaced U-FLARE, an additional spoiler gradient in the read direction shifts one of the two echo groups out of the acquisition window (gradient 'D' in figure 1.12). Echoes are not balanced and do not appear at the same time. Only spins with N number of TE periods in the transverse plane can rise to an echo signal in the middle of the acquisition window. The (N+1) echoes are destroyed outside the acquisition window. The displaced gradient is also accompanied by a trim gradient in the read direction (trim gradient 'T' in figure 1.12). The trim gradient is required to centre the echo in the first readout window and has to be adjusted experimentally.

1.4 The CIC biomaGUNE installation

1.4.1 Description of the installation

In 2008, a Bruker BioSpec 11.7T scanner (500 MHz) was installed in CIC biomaGUNE, as the third system in the world. The ultra-shield refrigerated (USR) magnet has a 16 cm bore (Bruker BioSpin, Ettlingen, Germany). Figure 1.13 provides an overview of the installation. The system is based on helium zero-boil-off and nitrogen-free magnet technology for reduced maintenance and longer service intervals. The technology AVANCE III HD MRI RF architecture has eight receivers and four parallel transmitter channels, one 1 kW 1H amplifier, four 300 W 1H amplifiers and 1 kW BB-amplifier for heteronuclear experiments.

The system possesses different RF coils and RF coil combinations, whereas in this work, two RF coil configurations have been used:

- An RF surface coil (RF 500 1H - Rat Brain SUC) as a receiver coil associated to a RF volumetric transmission coil (RF 72 mm - Vol coil 500 1H). The reception specification should be superior to 6750 SNR mm^{-3} . Surface coils are used to

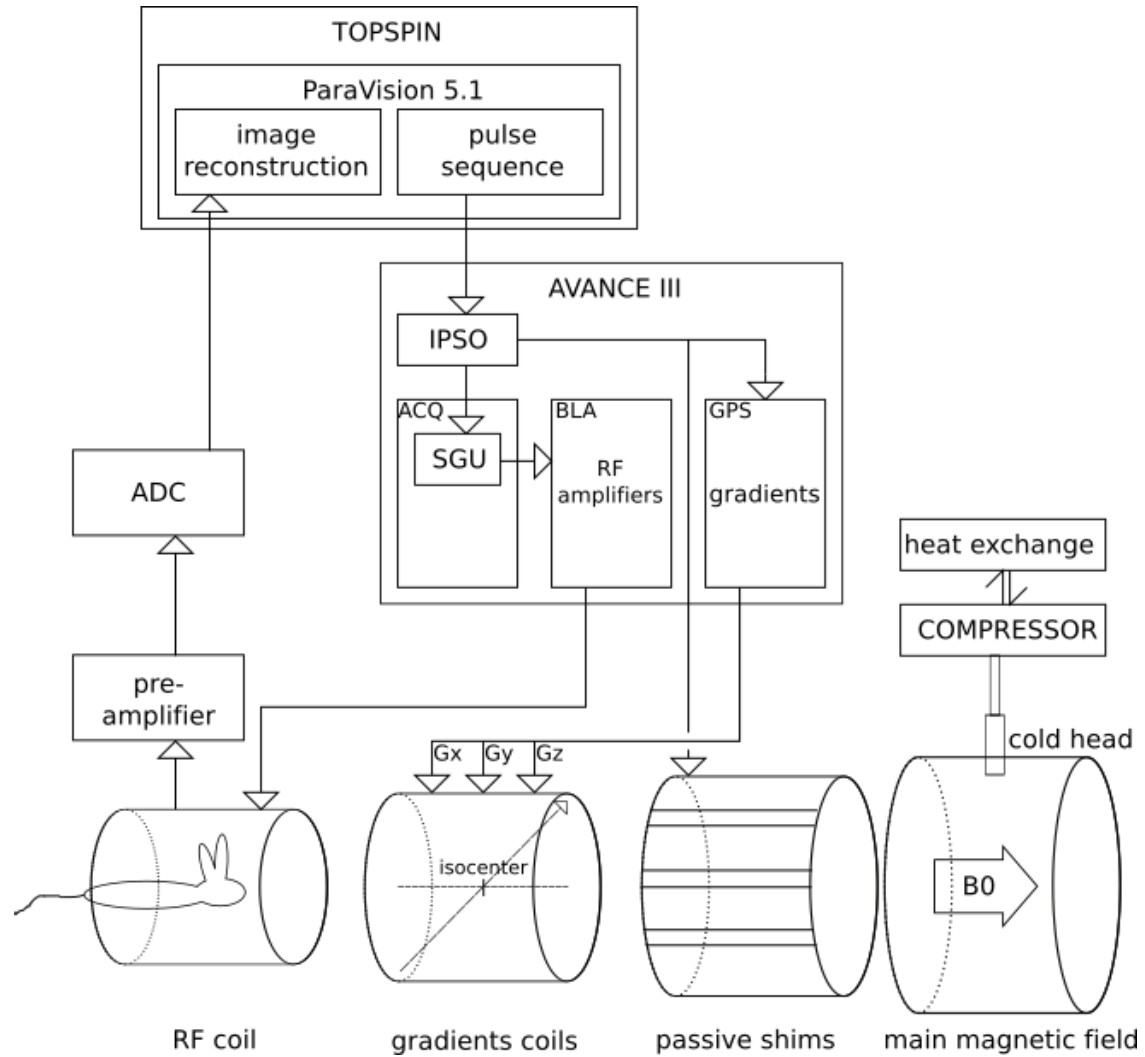


Figure 1.13: Schematic overview of a Bruker Avance MRI scanner. The main magnetic field B_0 is produced by a superconducting magnet that is liquid helium cooled (4 Kelvin). To prevent loss of helium, the helium is re-liquefied by a cold-head. The Paravision software is inter-phased to the intelligent pulse sequence organizer (IPSO) that controls the timing of the pulse-sequence, mainly RF transmission and reception and gradient pulsing. The passive shims are preheated by a gradient thermostat unit.

improve the SNR because they only detect noise from a small area as they are positioned close to the subject.

- An RF volumetric coil (RF Res 500 1H 40 mm - Mouse Body/Rat Head) with a specification superior to 4360 SNR mm^{-3} . Body and head coils, built as birdcage, are used to image relatively large areas and yield homogeneous SNR over the imaging volume. However, due to their large diameter, they generally produce images with lower SNR than the other coil configuration.

The quality of the MR signal and hence the spatial distribution of the signal varies significantly with position, size and design of the RF coil. Surface coils require a higher RF power than volumetric coils, since a larger area is exposed to the RF power. Comparisons between field strengths must also take into account comparisons between coil configurations.

High-performance gradient coil

The system is equipped with a nine cm ultra-shielded gradient coils (BFG-150/90-S gradient insert, Resonance Research Inc. Billerica, MA, USA). Within $90 \mu\text{s}$, 750 mT m^{-1} gradients can be switched. Magnetic field strength varies linearly, depending on the direction of gradients in the three directions of space as a function of position. Gradient coils $\{ \langle Gx \rangle \mid \langle Gy \rangle \mid \langle Gz \rangle \}$ are used for spatial encoding and specified in the pulse sequence by $grad\{ \langle read \rangle \mid \langle slice \rangle \mid \langle phase \rangle \}$. Each gradient can be activated to create a linear slope in the static field across the imaging volume in the X, Y or Z axes, respectively. For all gradients, zero is the magnet isocenter.

The settings allow faster and intense gradient use, potentially enabling the execution of MR protocols. However, this process is limited by the duty cycle, defined as the percentage of time the gradient is permitted to work to prevent gradient burn-out. The high-power gradients require circulation of cooling water to stay at a constant temperature and thus water is pumped through the system at a rate of 5 L min^{-1} by a gradient chiller (Affinity Chillers, Lydall Industrial Thermal Solutions Inc., Ossipee, NH, USA). The temperature of the cooling water is set at 18° C ; a compromise between cooling efficiency and the appropriate working of the gradient thermostat unit. The gradient amplifiers, operating at $300 \text{ V} / 200 \text{ A}$, generate the desired currents for Gx , Gy and Gz . Nine additional shim coils (Z_0 , X, Y, Z, Z_2 , ZX, ZY, X_2 - Y_2 , 2XY) are integrated into the gradient close to the object, and thus are powerful enough to achieve excellent field homogeneities.

Gradient thermostat control unit

During the execution of MR pulse sequences, water-cooled gradients are used. Due to the compact system design, their operation produces heat, which can dissipate, to heat the passive shims. Thus, local changes occur in the field, leading to inhomogeneities, especially if the system is driven hard for a long time period. The gradient thermostat control unit (GCTU) is a device that pre-heats the outside of the gradient coil, and indirectly the passive shims, to smooth out field drift effects caused by extensive gradient use. In our set-up, the gradients are heated to a pre-set temperature of 42.5°C within the bore of the magnet. The heaters are independently switched 'on' or 'off', and with the appropriate feedback, the desired temperature is reached. The unit successfully dampens temperature fluctuations, resulting in a reduction of the negative effect on the homogeneity caused by gradient heating [31].

The cold-head

The nitrogen-free magnet technology relies on a cold-head to re-liquefy helium and prevent its loss to the atmosphere. Therefore, a cryostat (Cryomech Syracuse NY USA, Helium compressor CP 2800) is used to enable the cold-head to re-liquefy the helium, and a heater is used to keep the Dewar pressure close to atmospheric pressure (1030 kPa). The cold-head pulses with a frequency of 1.41 Hz, roughly once every 709 ms. Importantly, the cold-head is known to cause vibrations, which has a more pronounced effect at high field. As the frequency is potentially matched with MR acquisition protocols, the cold-head may give rise to specific artefacts in single images and may affect the temporal stability of the experiments. Examples of the cold-head effect for specific MR experiments are discussed in chapter 4. According to the recommendation of the manufacturer, the cold-head should not be switched off as there is a significant risk of shortening the lifetime of the unit. In our experience, however, switching off the cold-head for up to 30 minutes, a short enough time interval to prevent helium blow-off through the release valve, and preventing large temperature changes in the seals, had no adverse effect on the lifetime of the unit. The cold-head has been changed every two years at regular service intervals.

AVANCE III, Paravision 5

One of the advantages of operating a Bruker MRI system is the modular software that controls the pulse-program, its commands, timings, etc. The intelligent pulse sequence organizer (IPSO) controls the signal generation unit (SGU) for the RF-generation of frequency, amplitude and phase, as well as the Bruker linear amplifier

(BLA) for the timing of the gradient switching and data acquisition (figure 1.13). Therefore, with a few exceptions, such as the restriction on the gradient duty cycle, the system is open and the user can optimize protocols, settings of timings in RF transmission and gradient pulsing. When appropriate, Bruker standard protocols were used or adapted. During this thesis, several test sequences were implemented, such as the zoomed U-FLARE sequence (chapter 2), an interfaced EPI sequence with an electrical stimulator to acquire the functional MRI and a cinematographic FLASH sequence for functional images.

1.4.2 Animal preparation

One of the most important aspects of *in vivo* success experiment is the animal preparation. All animal procedures in this research met the requirements of the European Union directive 2010/63/UE in accordance with the Spanish policy for animal protection (RD53/2013) and were authorised by the Basque government. Animal experiments were conducted at CIC biomaGUNE, an institution that holds a full accreditation from the American association for accreditation of laboratory animal care (AAALAC) international. A careful attention was paid to the key aspects of animal handling, including anaesthesia and physiological monitoring, positioning and maintenance through the MRI.

ANAESTHETIC CONDITIONS

Respiration leads to undesirable motion artefacts in MRI. In all our protocols, animal imaging is always performed under anaesthesia or sedation in a particular case of functional MRI (discussed in detail in chapter 4). Isoflurane, delivered in either 100% oxygen O_2 or combined with nitrogen N_2 (30:70 $O_2:N_2$), is a common breathable anaesthetic, characterised by a rapid anaesthetic effect, a rapid recovery time and a relative low cost. Prior to any MRI sequence, animals were anaesthetised using an initial high induction dose of up to 5% isoflurane in the induction chamber. The isoflurane percentage is controlled by a vaporizer that mixes vapour of isoflurane with the breathable gas of choice. Not all laboratories would have taken the same approach, but the implemented solutions were carefully administered as per our specific needs, based on the research presented in the present work and the imaging protocols used at the animal facility.

ANIMAL POSITIONING

To guarantee the smallest animal-to-animal variability and a good image quality, the animal positioning is one of the most critical aspects of *in vivo* MRI (figure 1.14).



Figure 1.14: Animal laying on its belly in sphinx position in a MRI-compatible 'bed'. On the left, the nose cone for gaseous anaesthesia is visible. The cables on the right are for measuring the rectal temperature; the blues lines are connected to a pressure sensor (under the animal's chest) to monitor the respiration rate. The animal's head can be fixated with the red ear-bars on the left.

A 'bed' that is MRI-compatible, a rigid platform with a specific placement for the coil, was used. The animal was usually positioned in sphinx position. Position of the animal inherently affects the RF tuning and matching and the RF pulse power, as well as the local susceptibility gradients and magnetic field inhomogeneities. For precise brain imaging, stereotactic fixation devices were necessary. However, it is always preferable to aim for symmetry. Animals were kept warm using a heated water blanket. Throughout the image acquisition, rectal temperature and respiration rate were controlled using an MRI-compatible animal monitoring system (SA Instruments Inc.).

START OF THE IMAGING SESSION

The MRI session always started with automated parameter adjustments for reference pulse gain and resonance frequency, a global shim (x, y, z, and z2), and a pilot scan of 1-mm thick slices in axial, sagittal, and coronal orientations.

Chapter 2

Comparison of fast imaging methods for relaxometry

The purpose of the following experiments was to investigate the U-FLARE sequence [25] using improved MR system hardware. This opened up a new field for U-FLARE experiments and had to be considered in relation with its ability to measure various parameters. Examples of inversion-recovery T1 and spin-echo T2 have been presented in this chapter.

An extension of U-FLARE was developed and utilised to map relaxation time distributions more rapidly than the gold standard described in the previous chapter. The following section describes the characterisation of a versatile single-shot method suitable at 11.7T for imaging relaxation times. We utilised snapshot FLASH and EPI to determine relaxation time in agar phantoms and in the mouse kidney. Advantages and disadvantages of the individual methods with respect to temporal and spatial resolution have also been discussed. The results were compared to those obtained with the newly implemented zoomed displaced U-FLARE sequence, which was adapted to map T1 and T2 at high spatial resolution. Its applications for abdominal imaging in a murine cancer model has been demonstrated.

Multi-parameters imaging methods

Since decades, fast MRI techniques have been described and optimised for applications requiring spatial and temporal resolution. Augmentation of the magnetic field strength provides a higher sensitivity and specificity in theory, but not practically, resulting in observable improvements *in vivo*. The advantages of high field strength are accompanied by specific properties, such as a longer T1 and a shorter T2. Among the factors impeding the improvements in sensitivity is the increased difficulty in eliminating B_0 and B_1 non homogeneities over time and from subject

to subject [32]. As direct comparisons between intensity values are difficult to interpret, multi-parameter imaging has to be considered. The use of the same imaging methodology might be beneficial to enable a precise co-registration and then to overcome intra- and inter-subject variability [32]. Different readout directions, spectral widths and imaging slice profiles yield different image resolutions and characteristics.

Differences in MR parameters determine the basis of all medical and biological applications of MRI. T1 and T2 weighted MR images provide valuable information for the detection and diagnosis of pathology in physiological alterations on pre-clinical models. In kidney pathologies, T1 measurement was already made [33]. Despite the lack of specificity in these T1 measurements to discriminate between scarring and kidney oedema, it provided an index of renal injury, which was more sensitive than the conventional method. Abdominal imaging always requires particular attention. Long imaging times were frequently required and severe motion artefacts might arise [9].

2.1 Implementation of fast imaging methods

All experiments were performed using a Bruker Avance 11.7 Tesla (500 MHz), which has been described previously. The 40-mm ^1H birdcage resonator (Bruker GmbH, Karlsruhe, Germany) was used for signal transmission and reception.

2.1.1 Preparation experiments

As already established in the first chapter, the fast imaging sequences have different intrinsic contrast. U-FLARE is basically determined by T2, EPI by T2* and snapshot FLASH by T1 contrast. In this chapter, MR methods have been developed to map relaxation time distributions rapidly by combining preparation experiments with single-shot or ultra-fast methods.

Longitudinal relaxation T1

As gold standard, T1 relaxation times are imaged using inversion recovery (IR) or saturation recovery. Recovery methods are limited by considerably long times, required for the partial recovery of longitudinal magnetisation between the measurement of successive points along T1 relaxation curve. According to Crawley and Henkelman, IR method is superior to the saturation recovery method due to a better

SNR [34]. This work focused on IR method for T1 measurements.

Longitudinal magnetisation is inverted and sampled as it recovers toward equilibrium. In T1 mapping, subsequent to an inversion pulse, repetitions of single-shot images may be acquired while increasing inversion delays to enable the detection of the inversion recovery time course (figure 2.1 A). This allows the fitting of the data on a pixel-by-pixel basis and provides T1 maps.

Single shot's biggest advantage is that it requires a much shorter time than conventional IR method. Lock Looker (LL) methods [23] are conventionally used for accelerating the acquisition protocol with a sufficient SNR and a relatively short TR [34]. This was applied to EPI and snapshot FLASH (figure 2.1 B). Following a 5-ms Sech inversion RF pulse ($BW = 4050$ Hz), repetitions of single-shot images were acquired. Sech pulses are known as hyperbolic secant-shaped pulses and show excellent inversion profiles due to its frequency selective inversion.

Separated by inversion delays (TIs), the first RF pulse inverts M_z to $-M_z$. IR measurements have been performed without selective inversion. No assumptions have been made about the effective inversion or the excitation depending on the B_1 uniformity [35]. During these inversion delays, spoiling gradients were applied to destroy any unwanted transverse magnetization due to imperfections of the RF pulse.

Transverse relaxation T2

The repetition of a single image with an increasing TE enables the creation of the T2 maps that fit the data pixel-by-pixel. Similar to the acceleration philosophy used in T1 mapping, multiple single-shot echo images can be acquired in quick succession following excitation. Once the transverse magnetization is created, its lifetime is governed by the spin-spin relaxation time T2.

2.1.2 Imaging sequences

New opportunities for U-FLARE

The zoomed U-FLARE sequence used in this work is a straight forward high resolution extension of the U-FLARE technique [27]. The implementation of the single-shot zoomed displaced U-FLARE sequence is illustrated in figure 1.12 (matrix= 64 * 64, spectral width= 100 kHz).

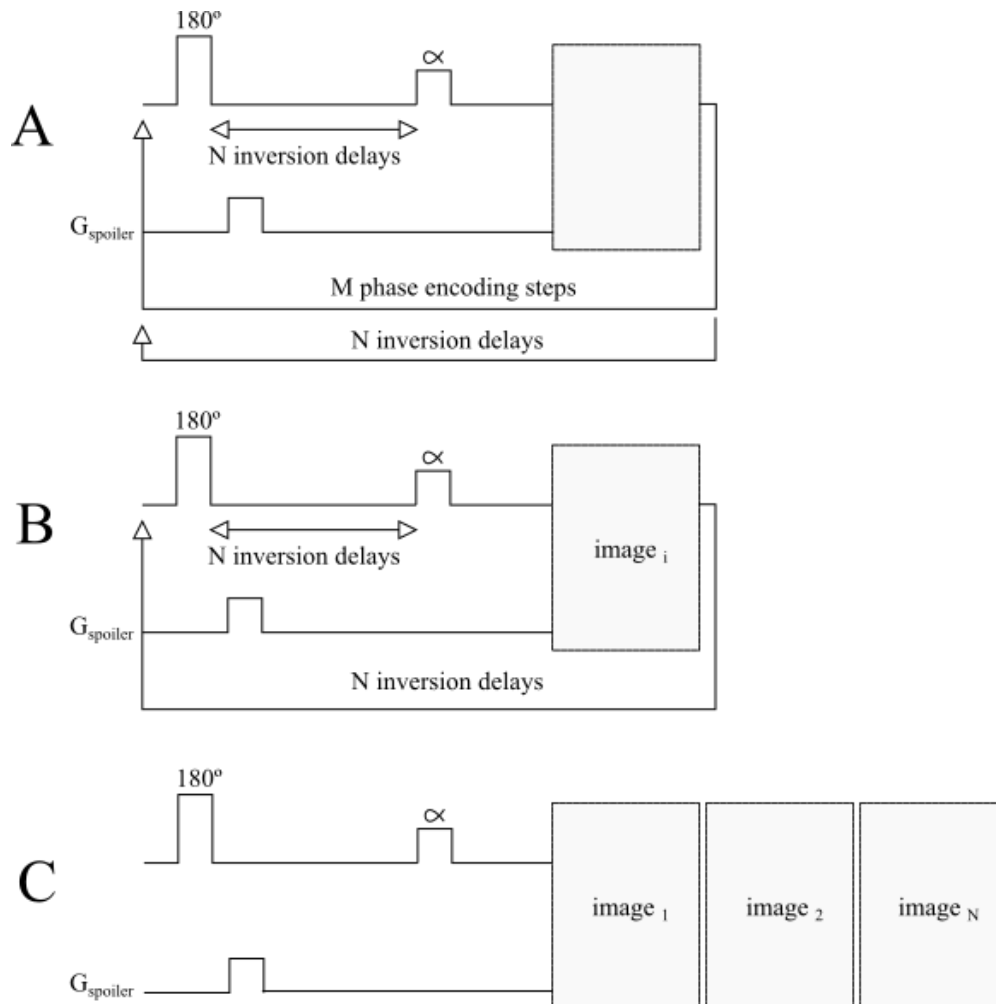


Figure 2.1: Different imaging protocols for T1 mapping. An inversion pulse is followed by the acquisition of a phase-encoding step of either a gradient echo or spin echo imaging method (A). The second phase-encoding step requires an additional inversion pulse after the repetition time (TR). Once the image is completed, the inversion times (TI) is incremented and another weighted image is acquired. Following the inversion pulse, a single-shot or snapshot image is obtained at TI (B). Following the relaxation delay TR, TI is incremented and a second T1 weighted image is acquired. In the last experiment (C), images are acquired in succession for Lock Looker (LL) EPI and snapshot FLASH.

PREPARATION OF THE TRANSVERSE MAGNETISATION BY AN HERMITE PULSE

The Hermite pulse, with low power requirements and a good slice profile, is a good compromise as a simple pulse shape, defined by the equation $f(x) = (1 - bx^2).exp(-x^2)$. The excitation pulse switches on the RF field modulation envelope for a short time, along the x axis. Compared to Gauss RF pulse, the Hermite RF pulse provides improved slice profile. Moreover, the Hermite RF pulse requires a bigger attenuation of 7 dB compared to a Gauss RF pulse of the same duration. However, the Hermite pulse shape consists still enough power to potentially be utilised with larger RF coils in future application.

In the present work, a pair of 1-ms Hermite RF pulses (BW= 5400 Hz) were used to prepare the magnetisation of an 18 * 18 mm square prism in the transverse plane. The magnitude of the signal was determined by the pulse shape, the attenuation [dB] and the pulse delay [μ s]. As excitation and refocusing pulses have the same bandwidth and the same pulse duration, the refocusing pulse requires a bigger attenuation than the excitation pulse. Doubling the flip angle corresponded to an superior attenuation of 6,02 dB ($20 * \ln(2)/\ln(10)$). The use of the Hermite pulse shape is limited by the side-bands of its profile; thus a larger FOV of 20.5 mm was selected to safeguard against potential folding artefacts.

REFOCUSING THE TRANSVERSE MAGNETISATION DONE BY A GAUSS PULSE

The spatial distribution is achieved by refocusing the transverse magnetisation. The slice thickness depends on the bandwidth of the pulse and the amplitude of the gradient section. The position of the slice depends on the frequency of the pulse.

The Gauss RF pulse is one of the simplest shape pulse described by the equation $f(x) = exp(-x^2)$. It was chosen because of its low power requirement and its insensitivities towards distortions. Short RF pulses are needed to implement the shortest TE possible and to limit the RF power. Gaussian RF pulse is preferable for rapidly refocusing a narrow slice. The transverse magnetisation was refocused perpendicular to the plane of the FOV using a train of 0.5-ms Gaussian RF pulses (bandwidth = 5480 Hz) to image an orthogonal 1-mm slice. The phase of the Gauss RF pulse was kept constant.

As a slice profile is a distribution of flip angles, this influences the slice profile and the relaxation time during the complete echo train. The effective decay of the transverse magnetisation depends on the refocusing angle [25]. A pure T2 decay is observed only in the middle of the slice acquired when the flip angle is equal to 180°. Only SE and refocused spin echoes are observed [7]. A 180° refocusing pulse

is required for maximum signal intensity. When the flip angle is not equal to 180° , the slice profile is influenced during the acquisition of the complete echo train. The signal decay over the ETL influences the point spread function (PSF) in the phase-encoding direction [25].

DUMMY SCANS AND CENTRIC PHASE-ENCODING

Eight dummy pulses preceded the acquisition of the image in order to allow echoes to equilibrate in signal intensity. To minimise the T2 contrast, the sequence should start with the weakest phase-encoding gradient. Hence, a centric phase-encoding scheme was used [25].

TIMING

The two Hermite RF pulses prepare the magnetisation in the transverse plane with a minimum TE_1 of 3.3 ms required. The transverse magnetisation is then refocused using a train of Gaussian RF pulses with a TE_2 of 2 ms. The loop is repeated for 64 echoes. The total acquisition time is done in 147 ms.

RELAXOMETRY

Sixteen inversion times ranging from 12 ms to 5 s were used for T1 mapping using the zoomed displaced U-FLARE sequence (figure 2.1 A). A relaxation delay of 20 s yields a total acquisition time of 340 s ($16 * TI + 16 * 20$) with an echo train duration of 128 ms ($64 * TE_2$). The protocol was slightly altered for *in vivo* experiments. Two experiments were averaged and a relaxation delay of 5 s resulted in a total acquisition time of 200 s.

For T2 mapping using the zoomed displaced U-FLARE sequence, the total acquisition time was 160 s ($8 * 20$) with eight echo times ranging from 21 ms to 77 ms ($TE_1 + SE$ preparations + 8 dummies echoes). The T2 mapping sequence was triggered by respiration for the *in vivo* application. The protocol was slightly altered for *in vivo* experiments. During the T2 mapping sequence, a relaxation delay of 10 s resulted in a total acquisition time of 80 s.

Gold standard for relaxometry

As a gold standard, T1 relaxation times are imaged using inversion recovery IR-SE ($TE = 8$ ms, $TR = 20$ s, 16 TIs ranging from 20 ms to 15 s, figure 2.1 B). T2 relaxation times are based on SE protocols ($TR = 5$ s, 10 TEs ranging from 8 ms to 80 ms).

EPI at high field

All EPI images were acquired with the following parameters: FOV= 32 mm, matrix= 96 * 96, SW= 357 kHz, and 1-mm slice. For LL-EPI (figure 2.1 B), 16 gradient echo EPIs ($\alpha = 20^\circ$) with a TE of 17 ms were acquired to cover a range from 22 ms to 6 s. Thus, the total acquisition time to acquire the T1 map was 6 s with an echo train duration of 25.8 ms. The respiration-triggered ME-EPI required the acquisition of 8 images with TEs ranging from 33 ms to 264 ms. This resulted in a total acquisition time of 300 ms for the T2 map.

Snapshot FLASH

LL-snapshot FLASH (figure 2.1 D) maps were acquired with the following parameters: TE= 1.2 ms, TR= 5 ms, FOV= 32 mm, matrix= 96 * 96, SW= 100 kHz, 1-mm slice, $\alpha = 5^\circ$ and centric phase-encoding. We acquired 8 images for the LL-snapshot FLASH following a 5-ms Sech inversion RF pulse with TIs of 0.01 s, 0.05 s, 1 s, 1.5 s, 1.9 s, 2.4 s, 2.9 s, and 3.4 s to map T1 within 5 s.

2.1.3 Models

AGAR PHANTOM

The use of agar phantoms is convenient because they have a T2 relaxation time comparable to that of *in vivo* tissue. Agar solutions of 1%, 2%, 3%, 5% and 10% were prepared. Agarose (Sigma-Aldrich, USA) in 750 μ L of milliQ water and 750 μ L of deuterated water (Eurisotop, J2971) was dissolved in a bain-marie at 90°C for 30 min and then degassed to remove air bubbles for another 30 min. The T1s and T2s of the agar samples were measured using the zoomed displaced U-FLARE sequence described above and compared to gold standard experiments.

Subsequently, to evaluate potential smearing in the phase-encoding direction, we also measured the apparent T2 decay of the magnetisation during the imaging part of the U-FLARE sequence. The phase-encoding was switched off, and the mono-exponential signal decay of the 64 echoes yields to the apparent T2. Additionally, in the 5% agar sample, we assessed the influence of the Gauss refocusing flip angle on the apparent T2.

In vivo MODEL: NAIVE MICES

Comparison of the MRI methods was performed in naïve male CD-1 athymic-nude Foxn1 nu/nu mice (n = 6, Charles River). Following the pilot scans already described in a previous section, a T1-weighted RARE image (TE = 6.7 ms, TR = 780 ms, FOV = 40 mm, matrix = 256 * 128, spectral width = 60 kHz, slice thickness = 800 μ m, 36 continuous slices, RARE factor = 2, number of average = 8, fat-suppressed) was acquired over a period of 6 min 40 s.

In vivo MODEL: A XENOGRAFT TUMOUR MODEL

The human pancreatic tumour cell line PANC-1 was obtained from and certified by the European Collection of Cell Cultures (ECACC, Sigma Aldrich) and was maintained in RPMI-1640 (Lonza, 12-702) supplemented with 10% foetal calf serum (Sigma-Aldrich, F7524), 100 units.ml⁻¹ of streptomycin, 100 μ g.ml⁻¹ of penicillin (Invitrogen, 15140-122) and 2 mmol.l⁻¹ of glutamine (Lonza, 17-605E). Cultures were grown at 37°C in a humidified atmosphere of 5% CO₂ for no longer than six months and were regularly tested for the presence of mycoplasma using a commercial kit (Lonza, LT-518).

Seven-week-old male CD-1 athymic-nude Foxn1 nu/nu mice (Charles River) were injected subcutaneously with 100 μ L of PANC-1 cells at a concentration of 20 * 10⁶ cells per millilitre of Dulbecco's phosphate buffered saline (Lonza, 17-213F) and Matrigel (Becton Dickinson, 354.234) in a 1:1 ratio. The injection was administered in the upper left flank approximately 1-2 cm below the armpit.

The suitability of the U-FLARE zoomed sequence was tested in tumour bearing animals 12 weeks after the injection of the cells (n = 4). Following the pilot scan already described in the animal preparation section, a T1-weighted RARE image (TE = 6.7 ms, TR = 780 ms, FOV = 40 mm, matrix = 256 * 128, spectral width = 60 kHz, slice thickness = 800 μ m, 36 continuous slices, RARE factor = 2, number of average = 8, fat-suppressed) was acquired over a period of 6 min 40 s.

2.1.4 Data processing

To calculate relaxation times in tissue, region of interest (ROI) were manually drawn on the images by using the ROI manager of ImageJ (ImageJ 1.48k) or the ISA tool package (Paravision 5, Bruker). For relaxation mapping, the data processing was performed using in-house developed software running under Python (Python 2.7.6). Example of the resulting T1 map are presented in figure 2.2.

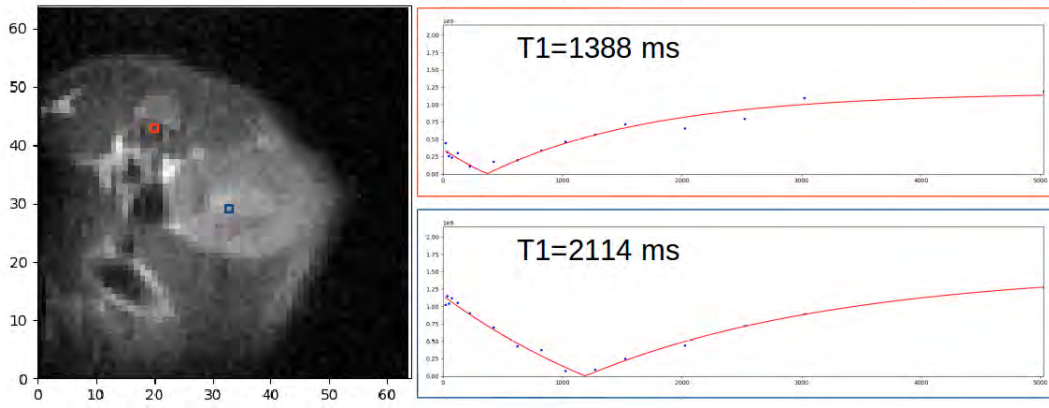


Figure 2.2: Example of inversion recovery (IR) method for T1 measurements using the U-FLARE sequence in the abdominal part of a naive mice

The longitudinal relaxation T1 was determined on a pixel-by-pixel basis using the Levenberg-Marquadt non-linear least squares three-parameters curve-fitting algorithm. The signal was fitted by:

$$S(TI) = \left| A - B * \exp\left(\frac{-TI_n}{T1}\right) \right| \quad (2.1)$$

with A the signal intensity ($A \simeq 1$) and B the signal compiling all the information concerning the inversion quality ($B \simeq 2$).

Similarly, the signal from the LL experiments was fitted by:

$$S(TI) = \left| A * \left(1 - B * \exp\left(\frac{-TI}{T1^*}\right) \right) \right| \quad \text{with} \quad T1 = (T1^*)(B - 1) \quad (2.2)$$

The transverse relaxation T2 was calculated by fitting pixel-by-pixel, the standard SE attenuation function as:

$$S(TE) = A * \exp\left(\frac{-TE}{T2}\right) \quad (2.3)$$

with A the signal intensity.

2.2 Results

2.2.1 Agar phantom

We successfully implement a displaced zoomed U-FLARE sequence at 11.7T. The readout window was centred on an echo to reduce sensitivity to the system imper-

Agar concentration	T1	T1	T2	T2	T2 apparent
	standard SE	U-FLARE	standard SE	U-FLARE	U-FLARE
1 %	4172	3969	122	124	155
2 %	4083	3862	72	71	93
3 %	3996	3831	50	54	71
5 %	3830	3660	35	36	47
10 %	3381	3303	19	19	27

Table 2.1: Relaxation times [ms] for different agar solutions measured by gold standard spin echoes (SE) and the implemented U-FLARE method.

fections.

The displaced version split odd and even echoes in time according to their parity due to the extra dephasing gradient. For the selected echo coherence pathway, each refocusing pulse had the same phase. This made it independent from the CPMG condition. The phase from the two echo groups did not have to be cancelled and the k-space did not have to be modulated. The centric encoding scheme minimised the effect of the PSF in the phase-encoding direction. However, with this phase-encoding scheme, the line-broadening was double because of the temporal resolution of the two consecutive lines in the k-space.

The echo train amplitude was stabilised by dummy scans and by adjusting the flip angle of the refocusing pulses to reduce the ghosting and some blurring artefacts [25]. However, the use of dummy refocusing pulses led to a delay in achieving maximum signal intensity.

We then determined the dependence of the Gauss refocusing flip angle on the signal decay over the lengths of the echo train (figure 2.3). A 180° refocusing flip angle presents a signal intensity that is 26% higher than that obtained at a 90° flip angle, and 41% higher than that obtained at a 45° flip angle. The apparent relaxation over the complete echo train length increased substantially with respect to the T2 values, with the largest increase observed for the fastest relaxing T2 agar phantom (figure 2.4 and table 2.1). Since a nominal 180° flip angle of the Gauss pulse in the imaging sequence process provided the highest SNR, the 180° flip angle was used for the single-shot *in vivo* experiments.

The suitability of the U-FLARE method was evaluated to image T1 and T2 relaxation times. We determined the relaxation times of different agar solutions using

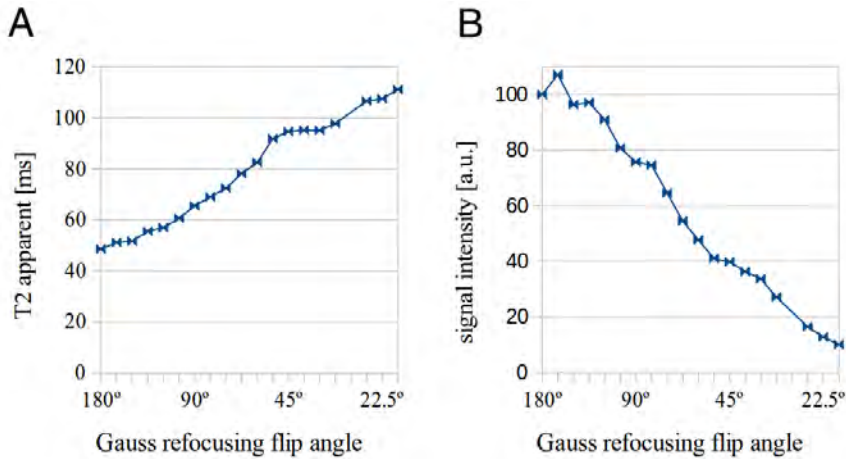


Figure 2.3: Dependencies of nominal refocusing flip angles on the apparent T2 (A) and the signal intensity (B) when imaging the 5% agar phantom.

the U-FLARE method and gold standard experiments (table 2.1). As expected, the T1 values only slightly decreased ($< 10\%$) with increasing agar concentration. Higher agar concentrations decreased water mobility and thus led to a substantial shortening of T2, in agreement with values known from literature [36].

In the 5% agar phantom, the observed SNRs were 43 for U-FLARE, 38 for LL-EPI, and 28 for LL-snapshot FLASH using the provided acquisition parameters for the individual fast imaging sequence.

2.2.2 Comparison of fast imaging methods for relaxometry

To evaluate the *in vivo* accuracy of the measurements, we measured T1 and T2 using U-FLARE, EPI, and snapshot FLASH in 6 naïve animals. In figure 2.5, the first column presents the raw image and on the second and third columns highlight the T1 and T2 maps, respectively. As outlined previously, no special pre-scanning or localised shimming was performed, which in turn made it impossible to obtain an EPI image of the kidney of two animals. The derived T1 and T2 maps compensate for the differences in SNR across the kidney and thus appear more homogeneous. As the lengths of the echo train are substantially longer than those of T2 and T2* for U-FLARE and EPI respectively, one has to assume that the provided resolution is only nominal. Some signal intensities were projected into the neighbouring pixel in the phase-encoding direction.

EPI is prone to a variety of artefacts like signal loss and geometric distortion. As highlighted in the first row of figure 2.5, EPI shows some sensitivity to B_0 heterogeneities in the abdomen at 11.7 Tesla. EPI also has noteworthy signal drop-out

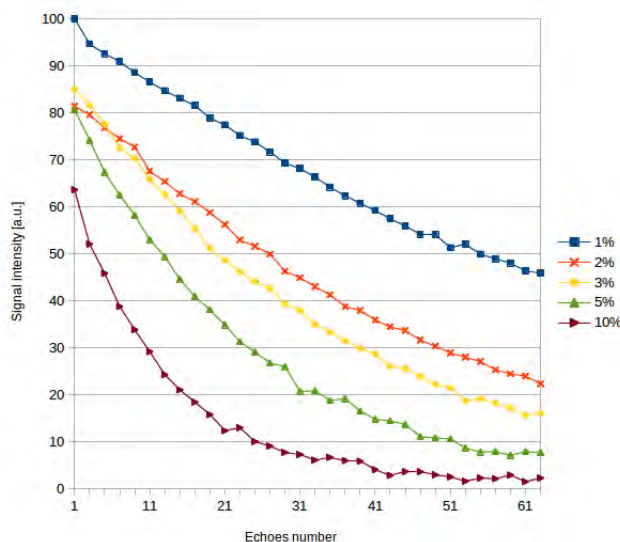


Figure 2.4: Signal decay curves for 180° flip angle during the imaging part (after the 8 dummy scans) of the zoomed U-FLARE sequence using agar phantoms with different concentrations, ranging from 1% to 10%. A mono-exponential decay fitted to the decay curve was used to obtain the apparent T2 (table 2.1).

in the kidney. Image distortion can be produced in regions of field inhomogeneities or magnetic susceptibility variations. Image blurring was caused by the $T2^*$ decay during the formation of the echo train, where each k-space line has a different $T2^*$ weighting.

U-FLARE is an attractive sequence for high field application. EPI is sensitive to stronger susceptibility gradients, significantly reducing $T2^*$ and thus reducing the time available for EPI. Time available for U-FLARE is determined by T2 and remains unchanged. However, in U-FLARE images, blurring artefact is evident along the phase-encoded (vertical) direction. Tissues with a shorter T2 produce more blurring than those with a longer T2. This can be aggravated with longer ETL or greater echo spacing.

As expected, LL-snapshot FLASH was observed to be well-suited for obtaining anatomical images of the kidney, even though the lower SNR of the imaging method translates directly into an apparent increase in noise within the T1-map. Relaxation times acquired *in vivo* for mouse kidneys using U-FLARE, EPI, and snapshot FLASH are presented in table 2.2. The measured T1 relaxation times are comparable while the standard deviations in both the kidney cortex and medulla in the mouse for the U-FLARE and LL-snapshot FLASH sequences are lower than those for LL-EPI.

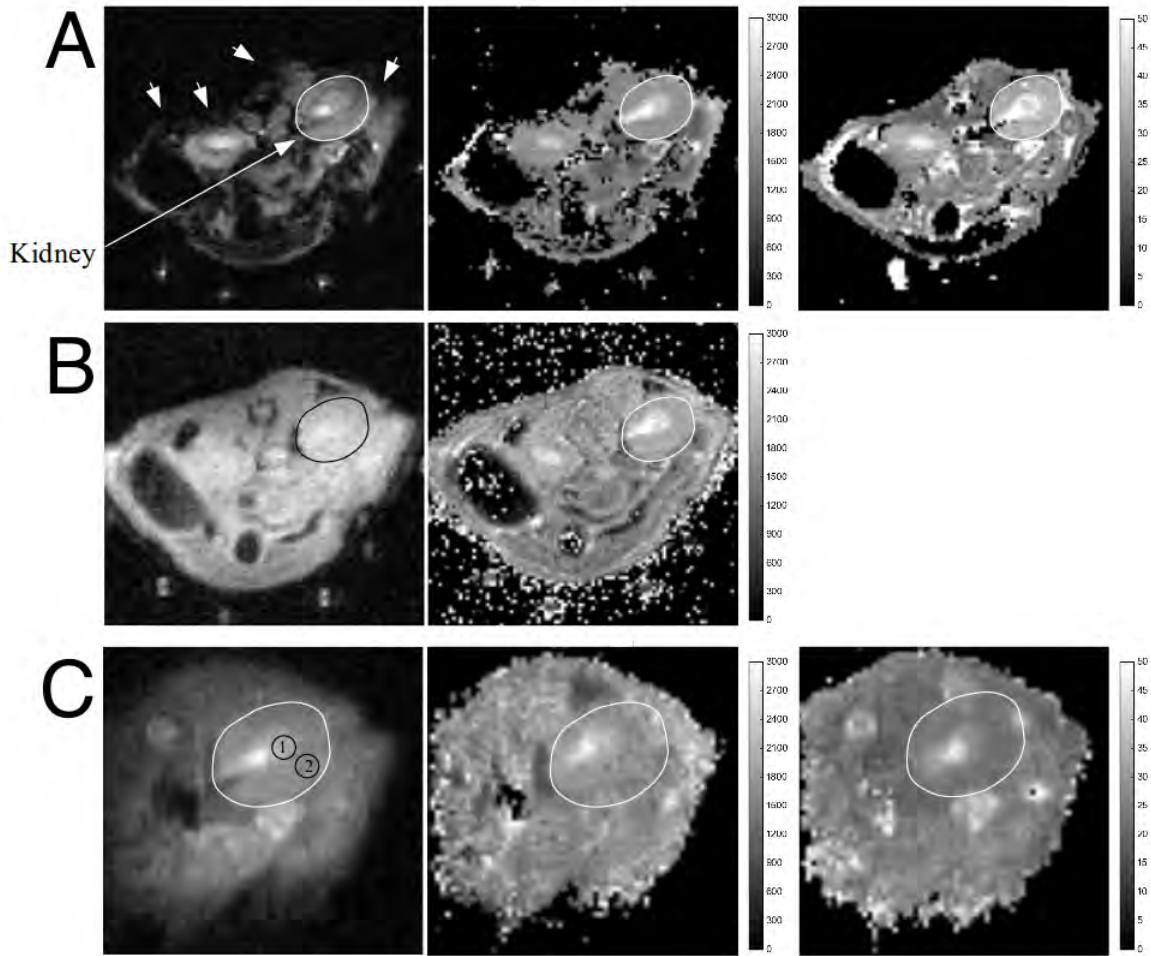


Figure 2.5: Comparison of *in vivo* images using EPI (A), snapshot FLASH (B), and zoomed displaced U-FLARE (C). The first column displays the raw images for each sequence. The arrow-heads indicate the image distortions in EPI. Regions of interest 1 and 2 (C, first image) indicate the area of data extraction for the medulla and the cortex, respectively. The second and third columns show the corresponding T1 and T2 maps.

	U-FLARE	EPI	snapshot FLASH
T1 cortex [ms]	1630 \pm 90	1610 \pm 420	1820 \pm 170
T1 medulla [ms]	2030 \pm 75	2150 \pm 520	2590 \pm 180
T2 cortex [ms]	25 \pm 4	30 \pm 4	
T2 medulla [ms]	29 \pm 5	36 \pm 7	

Table 2.2: Relaxation times (mean \pm standard deviation) acquired *in vivo* for mouse kidneys (n = 6) using U-FLARE, EPI, and snapshot FLASH.

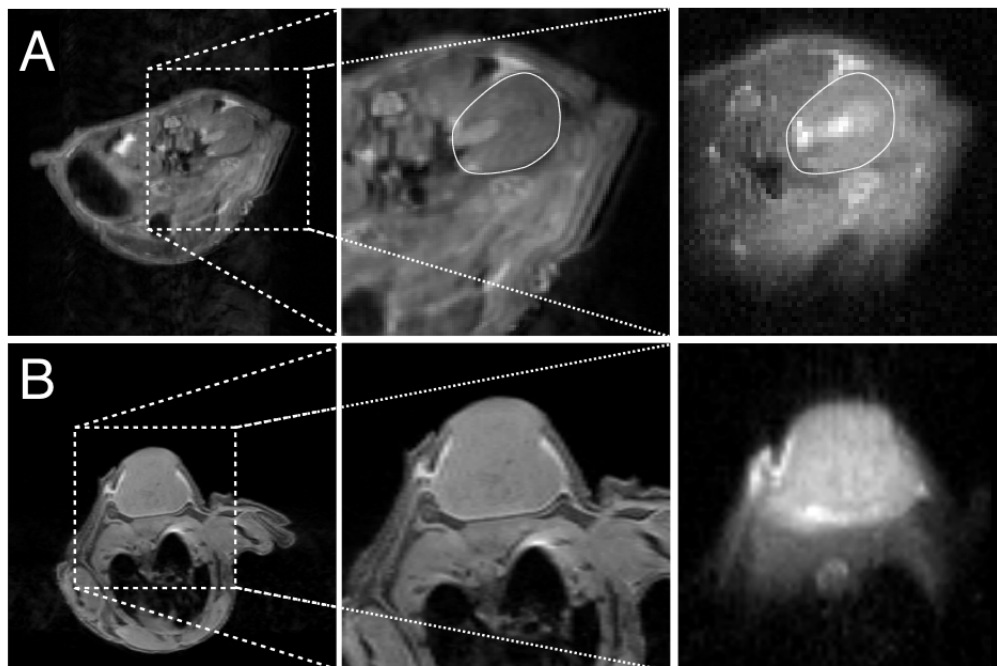


Figure 2.6: Comparison of the acquired high-resolution RARE scan (first column and second column) with the zoomed U-FLARE sequence for the kidney (A) and the tumour model (B).

2.2.3 U-FLARE suitable for abdominal relaxometry *in vivo*

The zoomed U-FLARE sequence was used for abdominal imaging at 11.7T. A comparison with a high-resolution RARE image highlights the insensitivity of the single-shot method to field heterogeneities of the kidney and the tumour (figure 2.6). In abdominal imaging, freedom from respiratory artefact clearly represents a major advantage. As already discussed, blurring artefacts are evident along the phase-encoded (vertical) direction in the U-FLARE image. Tissues with a shorter T2 produce more blurring than those with a longer T2. It can be further aggravated due to longer echo train length or greater echo spacing. When imaging the tumour model, two experiments were averaged. The blurring artefact is thus less visible.

A repeated acquisition of four slices demonstrates the robustness of the method for the acquisition of off-centre data (figure 2.7). This insensitivity to B_0 heterogeneities makes the U-FLARE sequence ideally suited for test-retest experiments at high field, where the subjects or objects would have to be imaged longitudinally over several hours, days, or weeks.

The determination of *in vivo* relaxation times was performed in the murine cancer model. The T1 relaxation times ranged from 1530 ms in the spleen up to 2365 ms in tumour tissue (table 2.3). This is in good agreement with the values known from literature and with the idea that the spin-lattice relaxation time becomes slightly

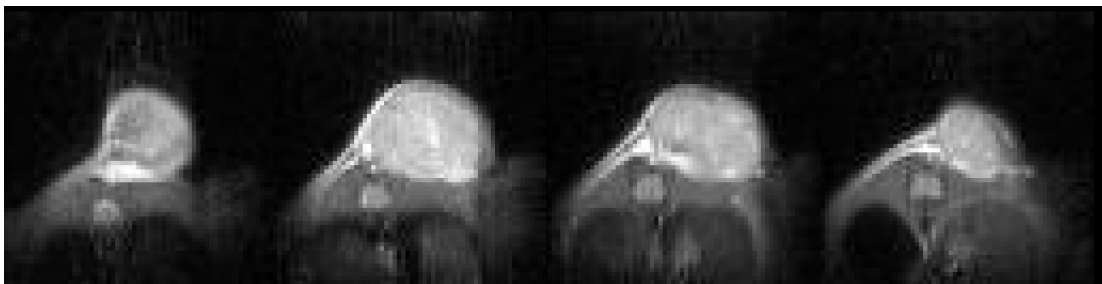


Figure 2.7: Multi-slices obtained *in vivo* demonstrate the robustness of the U-FLARE method.

	kidney cortex	kidney medulla	spleen	spinal cord	lymph nodes	muscle	subc. tumour
T1	1810±195	2100±185	1530±150	1845±95	1865±75	1800±290	2365±40
T2	29 ±2.5	25 ±2	20±2.5	28 ±0.2	20 ±1	16 ±2	28 ±1

Table 2.3: T1 and T2 values (mean ± standard deviation) obtained in various tissues *in vivo* in the subcutaneous tumour cancer model (n = 4) using the U-FLARE method at 11.7 Tesla.

longer at higher field [37]. Unsurprisingly, the spin-spin relaxation times ranged from 16 ms in the muscle to 29 ms in the cortex of the kidney. These T2 values are significantly lower than those reported at lower field strengths [38][39]. The results obtained in the spinal cord are in agreement with those obtained at 11.7T by Callot et al. [40].

2.3 Discussion

Generally, as outlined, single-shot imaging methods are the methods of choice for fast imaging of relaxation times. The acquisition of a complete image following the preparation of the magnetisation in the longitudinal or transverse plane can be utilised to map T1 and T2. To obtain high resolution images in a relatively short time, single shot can be used with a magnetisation prepared to image only part of an object by zooming in.

At high field, we successfully implemented the zoomed displaced U-FLARE accordingly. The U-FLARE method is remarkable for its insensitivity to susceptibility artefacts and its high SNR. The total acquisition time should not exceed $mTE = 1,26 * T2$ as discussed by Norris [25]. According to our results and as per the literature, the T2 values measured in mouse kidney at 11.7T are less than 30 ms [38]. With a TE of 147.3 ms, we did not reach the spatial resolution of the sequence.

In the U-FLARE sequence, blurring artefact is evident in the phase-encoding direction. The T2 image blurring can be reduced by deconvolution of the image. This requires at least an estimated T2 value along the phase-encoded direction or a T2 map [4]. The use of variable refocusing flip angle may also improve the sequence with relatively high SNR while limiting blurring due to relaxation [41].

Given its suitability for imaging both T1 and T2, the method may be used to characterise novel contrast agents *in vivo*. The zoomed U-FLARE method can also be easily adapted to image T2* or chemical shift imaging. Extending the use of this method to arterial spin labelling experiments might be challenging, as the zoom feature (implemented by selecting a cylinder) affects magnetisation outside the imaging slice. As future refinements, one could easily foresee the use of 2D excitation pulses [42] that provides spatial selective inversion in 2D following a single RF pulse. They are directly applicable to restricted FOV with high resolution imaging and to improve aliasing signal artefacts.

One major disadvantage of the current implementation of the zoomed-U-FLARE sequence is that it is only capable of imaging a single slice. Using repeated acquisitions of different slices to cover the complete tumour region would require an imaging time comparable to those of high-resolution contrast scans and the temporal spatial advantages of this method would no longer exist. Nevertheless, a single shot multi-slice U-FLARE has been already described for fMRI studies [43].

Another approach compatible with the refocusing pulse angle manipulation is the acquisition schemes using power independent number of slices (PINS). As its name implies, PINS is independent of the number of slices acquired, and it is considerably reduced compared to conventional multi-slice imaging. These methods have already been implemented in SE for rapid imaging of a large volume [44]. Norris et al. describe the generation of periodic RF pulses capable of exciting and refocusing multiple slices simultaneously as spatially selective and applicable to any 2D pulses sequences. Particular gain can be expected at high magnetic field strength and for sequences that have a non-negligible SAR like the RARE sequence. In 2014, Norris et al. explored the possible power reduction in simultaneous multi-slice imaging in turbo-SE [45].

Zoomed ultrafast low-angle RARE, LL-snapshot FLASH and EPI are techniques that have been utilised in this study. For T1 relaxation, a series of single images have to be acquired following an inversion pulse. For T2 relaxation, the repetition

of a single image with an increasing TE enables the detection of the T2 relaxation time course. Using this approach, fitting the data on a pixel-by-pixel basis yields to relaxation maps. U-FLARE utilises multiple inversion pulses and offers the possibility to acquire data more slowly than EPI and snapshot FLASH but with higher precision. A longer imaging readout time and a higher SNR are allowed by a reduced spectral width. The general advantage of the sequence over EPI is based on the fact that the imaging readout is sensitive within T2 rather than T2*.

LL-EPI and LL-snapshot FLASH are ideally suited to rapidly map T1 images. The magnetic susceptibility effect considerably increases the difficulty in performing rapid imaging at 11.7T. The assumption of a mono-exponential signal decay might be violated in some areas suffering from susceptibility artefacts [32]. At high field, LL-snapshot FLASH has inferior SNR compared to U-FLARE. Snapshot FLASH based sequences [13][46] are gradient echo sequences with very low flip angles and read out magnetisation in the longitudinal plane. The measurements of apparent diffusion coefficient distributions or T2 mapping may require special attention [18]. Conventional FLASH method is at least 30 times slower than EPI [13]. As demonstrated, FLASH experiment suffers from a lower SNR than RARE or EPI. The effects of susceptibility artefacts on the signal decay may be reduced by a higher spatial resolution. The precision of the LL-snapshot FLASH maps may be improved by increasing the echo time, but this would also prolongate the total acquisition time [32].

EPI is a versatile method using high SNR but is limited by T2* [32][47]. It can be used to image magnetisation prepared in the transverse or longitudinal planes. At high field, LL-EPI is sensitive to B_0 heterogeneities. Detailed knowledge of the B_0 field distribution is necessary to select an adequate corrective technique. The effects of magnetic field inhomogeneity on the EPI signal include frequency shifts, causing geometric distortions, and distortion of T2* relaxation, leading to signal loss and image blurring artefacts. Furthermore, EPI images are typically acquired with a long acquisition trajectory during which rapid imaging becomes inherently vulnerable to magnetic field inhomogeneity artefacts. The signal loss artefact can be understood as a result of signal drop-out at effective TE when the signal at the centre of the k-space is sampled.

Independently, the Look and Locker approach is sensitive to B_1 heterogeneities and to pulse imperfection, and especially to inversion quality and excitation pulse [48]. Thus, the non-uniformity of the signal intensities may give rise to errors in quantifying T1 MRI parameters [49]. This may result in large standard deviations for T1 values obtained through repeated experiments. Improved T1 estimation can

be achieved through the use of the B_1 field and therefore through flip angle mapping, although this increases the scan time. Relaxation maps may need to be corrected for RF transmit and receive field inhomogeneities.

When the two T2 mapping methods are compared, it can be observed that ME-EPI can be acquired in a single-shot eight times faster than U-FLARE. The saved time can thus be used to either accumulate data to yield superior SNR or to segment the acquisition protocol to reduce the B_0 sensitivity of EPI at high field [40]. Segmenting the sequence would shorten the minimum TE and yields higher resolution images and less smearing. However, the use of variable refocusing flip angle to improve the U-FLARE sequence, such as segmented FLASH or EPI, has generally led to reductions in SNR per unit time [41][50]. This may be undesirable if one wishes to acquire multiple parameter images and maps rapidly.

Importantly, both U-FLARE and EPI have relatively long minimum echo times. The achievable minimum TE for EPI and U-FLARE is most likely too long to estimate relaxation times for intracellular and extracellular compartments. Steady state free processing (SSFP) methods [51] are very fast, and offer high SNR and flexible contrast with short TEs. They thus remain the gold standard for magnetic resonance fingerprinting (MRF) [52]. Ma et al. introduce the new method called MRF using a pseudo randomized data acquisition of a unique signal evolution or ‘fingerprint’ of different materials/tissues. One should understand it as a function of multiple material properties. This function should be then post-processed to match the fingerprints to a predefined pattern of predicted signal evolutions. A combination of T1, T2, magnetisation transfer preparation or diffusion weighting or mapping may be used for MR fingerprinting [53].

2.4 Conclusion

This work demonstrates that the zoomed U-FLARE sequence yields single shot single slice images with good anatomical resolution and high SNR at 11.7T. We successfully implemented a displaced zoom U-FLARE sequence and adapted it to map T1 and T2 in a murine cancer model. Generally, the method is robust, does not require slice selective shimming, pre- or post-processing and is thus ideally suited to obtain fast multi-parameter images or maps from a single slice longitudinally with a high resolution at high field.

Chapter 3

High resolution MR Angiography of six rat strains

Vascular malformations or abnormalities and many brain pathologies such as strokes, neuro-degenerative diseases, and brain tumours influence the cerebral vascular network. A wide range of imaging modalities have been used to investigate the cerebrovascular system with a limitation either on their spatial resolution or on their allowed time. Vascular imaging can be performed using ultrasound Doppler imaging, or by computed tomography or magnetic resonance angiography (MRA) [54]. Nuclear imaging modalities (positron emission tomography (PET) and single photon emission computed tomography (SPECT)) have never been used at high-resolution to image the vascular network due to reconstruction limitations of the scanners [55]. X-ray imaging-based techniques such as computed tomography is usually evaluated *in vivo* as it is able to exclude stroke mimics such as brain tumours and subdural hematomas and can separate brain ischemia from haemorrhage [54]. Contrast-enhanced computed tomography imaging enables 3D visualisation with a high spatial resolution and good SNR. However, these techniques need the injection of contrast agents based on iodine, gold and bismuth for use in *in vivo* imaging.

Computed tomography techniques, such as brain imaging with MRA, can localize the regions of brain infarction and haemorrhage. As it might be used completely in a non-invasive way [56], advances in MRA are essential to improve the accuracy of this technique. The purpose of this work is to establish a robust protocol of MRA suitable to image the arterial vasculature of the rat without the use of contrast agents in different strains. This chapter describes the implementation of robust MRA protocols with a high spatial resolution and its application in six different rats' strains to image the cerebro-vasculature at 11.7T. The methods were then applied to an experimental stroke rat model to derive the infarct size.

3.1 Magnetic Resonance Angiography

Three main MRA techniques based on different physical properties can be used. Based on physical properties of flowing blood, the first two methods, the time of flight (TOF) method and the phase contrast angiography alternative, allow the direct visualisation of the vascular structure. The TOF technique, which was used in this study, is based on the principle of in-flow of unsaturated blood into the imaged slice, whereas the phase contrast is a method that images moving magnetisation by alternating flow encoding gradients [57]. The third technique called black blood angiography produces images that attenuate or eliminate the blood signal intensity [4]. Ultra-high resolution MRI has been already investigated at 9.4T [58] with a resolution of less than 100 μm in less than one hour.

3.1.1 Time of flight technique

Direct visualisation of the vascular structure can be done by the TOF technique. TOF method relies on the principle of in-flow of unsaturated blood into the imaged slice of blood flowing, leading to an increase of vessel intensity compared to the stationary tissue background. This effect is known as flow related enhancement (FRE). The signal from stationary tissue is saturated by using a GE sequence with a short TR, a large flip angle and the use of repetitive excitation. Meanwhile, non-saturated blood flows into the imaging plane and will appear bright in the image.

Typically, TOF MRA is sensitive to several tissue parameters like the T1 of the blood and the flow velocity, the thickness and the orientation of the slice, and sequence parameters like TR and the flip angle. As flow is generated by heart pulsation, fluctuations of the blood signal intensity may appear during the scan, generating artefacts. Performing a synchronised acquisition with the heart would be an effective way of avoiding these kind of artefacts, but it will lead to an unacceptable scanning time.

Gradient echoes with flow compensation

TOF MRA can be acquired in different modes. The mode which is especially suited for straight vessel section, a 2D MRA excitation of very thin slices, might be sufficient to suppress the stationary tissue at very low replacement velocities. However, as spins are moving into the excited volume, repeated RF excitation could be necessary, resulting in saturation and a loss of blood signal.

In vessels with higher blood flow velocities and in small intracranial vessels, a 3D MRA method using smaller flip angle (usually between 15° and 25°) might overcome the saturation in the excitation volume even though the background contrast is somewhat lower in the 3D technique. The protocol based on the sequence called gradient echo flow compensated (GEFC) improves the signal of moving spins by compensating the signal loss. In fact, this method compensates the dephasing effects of the spins during TE. Although the saturation of the signal is lower with a smaller slab thickness, the slab should be as thick as possible and adjusted to the region being studied.

Maximum intensity projection

The images can be viewed one slab at a time or post processed as maximum intensity projection (MIP), the most common way. For the visualisation of angiography data, a 2D projection is performed from the 3D dataset. Only the pixel with the highest intensity is projected onto the imaging plane.

Flow related enhancement

The selection of the flip angle and on the TR should be done according to some FRE simulations. For a GEFC sequence following N RF-pulses with the flip angle α , the longitudinal magnetization is defined as [4]:

$$M_z(t_{n+1}) = M_z(t_n) \cos(\alpha) \exp\left(-\frac{TR}{T_1}\right) + M_0(1 - \exp\left(-\frac{TR}{T_1}\right)) \quad (3.1)$$

where $M_z(t_n)$ is the longitudinal magnetization after N pulses and M_0 is the magnetization at equilibrium. At steady state, the longitudinal magnetization $M_z(t_{n+1})$ equal $M_z(t_n)$.

Similarly, the transverse magnetization M_{xy} following N RF-pulse is defined at steady state as:

$$M_{xy}(TR) = M_z(t_n) \sin(\alpha) \exp\left(-\frac{TE}{T_2^*}\right) \quad (3.2)$$

In TOF MRA with a GEFC sequence, the signal S_j from the blood is dependent on j the number of experienced RF-pulses at a given TR [4]:

$$S_j = M_0 \left(\frac{M_z(t_n)}{M_0} + \left(\cos(\alpha) \exp\left(-\frac{TR}{T_1}\right) \right)^{j-1} \left(1 - \frac{M_z(t_n)}{M_0} \right) \right) \sin(\alpha) \exp\left(-\frac{TE}{T_2^*}\right) \quad (3.3)$$

3.1.2 Studies of cerebral ischemia

In theory, MRA can be performed on naïve animals before, as well as during and/or after middle cerebral artery occlusion (MCAO). Generally, when animals arrive at the imaging facility, they could be pre-screened by MRI to evaluate their suitability for the experimental stroke models. Hereby, animals with abnormal cerebral arteries or enlarged ventricles, or hydrocephalus could be identified and excluded from the study prior to surgery to reduce the variability measure of outcome.

Immediately following a transient MCAO, a successful reperfusion might be visualized by MRA and confirmed by perfusion readouts to exclude animals and minimize experimental variability within the study cohort [56]. As putative treatment regimen might influence cerebral perfusion, a characterization of the middle cerebral artery (MCA) branching off from the circle of Willis might be the only direct measure to detect abnormalities in the cerebro-vasculature within a study cohort to justify an inclusion or exclusion of a specific animal.

The purpose of this work is to establish a robust protocol of 3D TOF MRA suitable to image the arterial vasculature of the rat without the use of contrast agents in different strains. Several imaging protocols differing in the required spatial and temporal resolution were utilized to improve upon previously reported protocols [56]. The methods were then applied to an experimental stroke model of 60 minutes transient MCAO using an intraluminal thread [59]. The 3D TOF MR angiograms were obtained in the rat 24 hours after reperfusion to derive the infarct size.

3.2 Methods

3.2.1 *In vivo* model

SIX DIFFERENT RAT STRAINS

Healthy male rats of six different strains (n=4, 240–345 g) were used in this study. Sprague Dawley (SD), Wistar Kyoto (WK), Spontaneous Hypertensive Rats (SHR) and Long Evans (LE) provided by Janvier Labs (Saint-Berthevin Cedex, France) and Fischer 344 (FI) and Lister Hooded (LH) rats by Charles River Laboratories (Calco, Italy) were allowed to rest in ventilated cages, with an enriched environment for animal welfare, for at least five days following transport and had free access to food and water.

TRANSIENT ISCHEMIA IN SPRAGUE DAWLEY RATS

The experimental procedure, done by Marta Beraza, was performed following criteria derived from the Stroke Therapy Academic Industry Roundtable (STAIR) group guidelines for preclinical evaluation of stroke therapeutics [60][61]. First, the vascular recirculation was confirmed by MRA, as an index of the reliability of the ischemic model. Standard sized occluder were used according to the animal strain and size. The temperature was controlled during the ischemic period.

Through a ventral midline neck incision the right common carotid artery (CCA) was exposed up to the bifurcation of internal (ICA) and external carotid artery (ECA) and clamped. The ECA was ligated with a 6-0 silk suture. A silicone rubber coated thread (Doccol, USA) was introduced into the ECA and advanced into the lumen of the ICA up to a length of 17-18 mm to occlude the MCA. Recirculation was initiated after 1 h by removing the thread and the CCA clamp. Using this procedure, the CCA is reopened and the blood flow to the brain is re-established. Only vascular branches fed by the ipsilateral ECA remained permanently occluded. The incision wound was closed with a 4.0 silk suture and the rat brought back to its home cage.

3.2.2 Imaging methods

The 40-mm ^1H -resonator was used for RF transmission and reception. Following the pilot scans already explained in a previous section, a high resolution RARE sequence was then used with the following parameter: FOV 40 mm, matrix 256*256, 24 slices of 1 mm thickness, pixel resolution 0.156 mm/pixel, either to determine the brain volume in naïve animals or to determine the stroke volume 24 hours of 60 min transient MCAO. No triggering by electrocardiogram or respiration was applied.

A slice selective 3D FLASH flow compensated method has been used. The first set of images was then acquired with the following parameter: FOV 32*32*32 mm (32 mm slab), matrix 256*256*256, TE of 3 ms (echo at 30% of the readout), TR of 30 ms, a spectral width of 50 kHz and a nominal 45° flip angle (1-ms Sinc RF pulse with 10 lobes). Using the olfactory bulb as a reference, six different MRA data sets were acquired. The center of the slice was varied in steps of 5 mm from the rostral (10 mm) to the inferior part (-15 mm bregma) of the brain.

The second set of images was then acquired with the following parameter: FOV 32*32*32 mm (32 mm slab), matrix 256*256*256, TE of 2.55 ms (echo at 30% of the readout), TR ranged from 7.51 (shortest time available with a spectral width of

100 kHz), 15, 30 and 60 ms and a nominal 30° flip angle (1-ms Gauss RF pulse). Ultra high resolution angiograms were then acquired with: FOV 32*32*32 mm (16 mm slab), matrix 512*512*256, TE of 4.45 ms and TR of 60 ms. Two animals of each strain were subjected to the study with the duration of all imaging sequence combined not exceeding 4 hours.

Twenty-four hours after MCAO, for a SD and SHR rat only, the high resolution protocol was also used to determine high-resolution angiograms. In 45 SD rats subjected to 60 min MCAO, the following MR protocol was used to determine the occurrence of larger cerebrovascular abnormalities: FOV 32*32*32 mm (32 mm slab), matrix 128*128*128, TE of 2.55 ms and TR of 15 ms.

3.2.3 FRE simulation

FRE simulations highlight the importance of the selection of the flip angle and on the TR. The normalized signal intensity of the partially saturated magnetization in dependence of the RF flip angle is illustrated in figure 3.1 (A). At 11.7 Tesla, the average relaxation time reported for nine different rat brain structures of SD rats is 2018 ms and 34.7 ms for T1 and T2, respectively [1]. For blood, the reported relaxation time for oxygenated arterial blood at 37°C is 2813 ms and 46.3 ms or T1 and T2, respectively [62]. In this FRE simulation, T2 values was used instead of T2*.

The FRE strongly suggests using a high flip angle for vascular structures with high flow velocity or thin slabs, and a lower flip angle for larger FOVs and lower velocities. For example, at a TR = 60 ms, for flip angle up to 15°, the contrast to detect the vessel is not optimal, but for up to $j = 11$, the signal intensity arising from any vessel is similar. Contrary, an optimized flip angle of 60° for a vessel that experiences only two RF-pulses ($j=2$) at the given TR, may show substantially higher signal intensity than a vascular structure. The resulting angiogram would display vessels with substantially different intensity. Therefore, in 3D-TOF that does not aim to image a specific part of a vessel, lower flip angles are a good compromise.

Figure 3.1 (B) compares the FRE of a TR = 60 ms ($j = 2$) with TR =30 ms ($j = 4$) and TR =15 ms ($j = 8$). Using this example, the gain in faster imaging time could potentially be used for averaging and to partially offset the contrast dependence on the flip angle (figure 3.1 (C)).

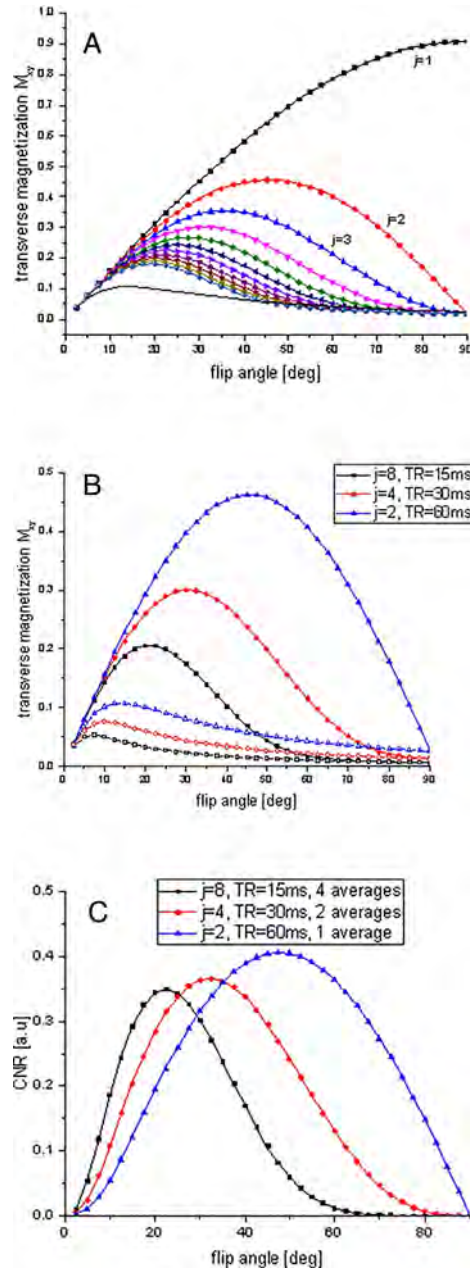


Figure 3.1: Normalized transverse magnetization M_{xy} of blood for j the number of experienced RF-pulses from 1 to 11 for a TR of 60 ms (A). Then, M_{xy} of blood is normalised for $j= 2, TR= 60$ ms; $j= 4, TR= 30$ ms and $j= 8, TR= 15$ ms (B). According to different flip angles, the contrast to noise ratio (CNR) for constant blood flow velocity is plotted in (C) (figure from [63]).

3.2.4 Data processing

The CNR was determined by subtraction the mean signal intensity of a vessel ROI from the background signal intensity of a brain ROI (without apparent blood vessels) derived from within the same slice and dividing it by the SD of the noise. The CNR for the ACA, MCA, the rostral part of the circle of Willis, the ICA and the basilar artery was determined.

No data preprocessing MR angiograms was needed except a potential zero filling in all three dimensions. The raw images were analysed by ImageJ (ImageJ 1.48k) after rescaling for further processing. Vessels are visualized using maximum intensity projection (MIP) algorithm. Additionally, for comparison, a manual segmentation of brain was performed selectively on slices of the cranium. The 'cleaned' raw images were combined with the slices from outside the cranium and then subjected to MIP to obtain the MR angiograms. This allowed the visualization of the intracranial blood vessels and the visualization of the connection to the extracranial vessels not affected by the pre-processing step.

3.3 Results

Optimal position of the FOV

Figure 3.2 displays six rat brain angiograms of a Sprague Dawley (SD) rat, obtained by centring the trans-axial imaging slab 10 to -15 mm from bregma. With the FOV centred at 5-10 mm bregma, the excitation of the frontal part of the head saturates all venous and arterial structures from the eyes and nose (figure 3.2 A and B). The bregma is usually used as anatomical reference, it is the intersection between the coronal suture and the sagittal suture on the skull. In figure 3.2 C to F, the venous structures are visible at the top of the FOV. The vertebral arteries are visible to a large extend (figure 3.2 F) if the FOV is centred well below the brain. The signal intensity of the basilar artery, measured at the height of the anterior inferior cerebellar artery (AICA), decreases if the excitation pulse continues to affect the rostral parts of the vertebral arteries (figure 3.2 D and E).

In the axial angiogram (figure 3.3 A), the anterior cerebral artery (ACA, 17.5 mm from the isocenter), the middle cerebral artery branch (MCA, 14.25 mm), the base of the circle of Willis at around the MCA branching (CoW, 12.13 mm), the internal carotid artery (ICA, 5.88 mm) as well as the basilar artery (BA, 1.75 mm) are indicated. Subsequently, in figure 3.3 B, a steady decrease of CNR from 77 to 10 was observed. Interestingly, the network supplied by the posterior internal cere-

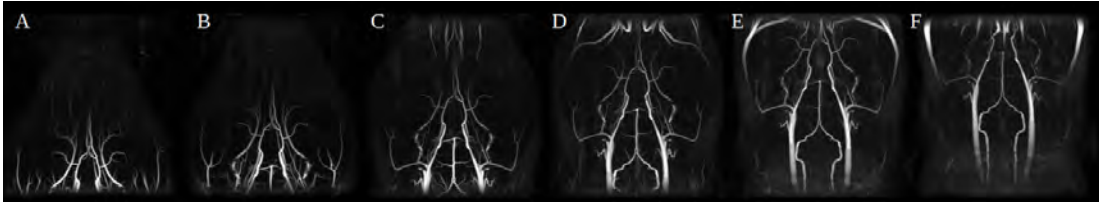


Figure 3.2: Figures A to F display the different MR angiograms of the same Sprague Dawley rat from centering the field of view (-15 mm to bregma, A) in steps of 5 mm towards the rostral part (10 mm bregma, F).

bellar artery (PICA), which originates from the vertebral arteries, becomes clearly visible only if the FOV is adjusted in such a way that the excitation of slowly moving blood from the vertebral arteries is minimal. Similarly, the other two main arteries that supply blood to the cerebellum, the AICA and the superior cerebellar artery (SCA), are most intense for choosing that FOV offset and flip angle.

Likewise, the optimal CNR for any blood vessel could be observed if the vessel of interest is just a few millimeter within the FOV, and thus avoid saturating the in-flowing blood (figure 3.3 B). It would require an offset of 10 mm to bregma to achieve the highest CNR for the MCA. Using this setting, all other main arteries like the cerebellar arteries, the BA, the posterior cerebral artery (PCA) and the ICA would not be detected as they are outside of the FOV (figure 3.2 F). Thus, to visualize all main brain arteries, the FOV was centred at bregma and the flip angle was reduced.

Optimisation of TR

Figure 3.4 displays the rat brain angiograms of a Fisher rat, showing the sagittal and axial views obtained at four different TR (7.5, 15, 30 and 60 ms), thus increasing in-flow delays between excitations. As can be seen with a resolution of $125 \mu\text{m}$, with the increase of total acquisition time from 6 to 50 minutes, the more distal parts of the middle cerebral artery (MCA) supplied vessel structure becomes visible. The extremely fast imaging time of 6 minutes was not able to reliably identify the branching of the MCA from the circle of Willis as the in-flow delay is minimal. Thus, for the subsequent experiments, evaluating the influence of the cerebro-vasculature on the infarct size evolution, a TR of 15 ms was used with lower resolution.

With an increase in resolution from $125 \mu\text{m}$ to $62.5 \mu\text{m}$, more details, especially larger branches in between the PCA and MCA arising from the circle of Willis or early MCA branches become detectable (figure 3.5 A). Given the increased complexity of the MRAs displaying all vessels of the head from within the FOV, we

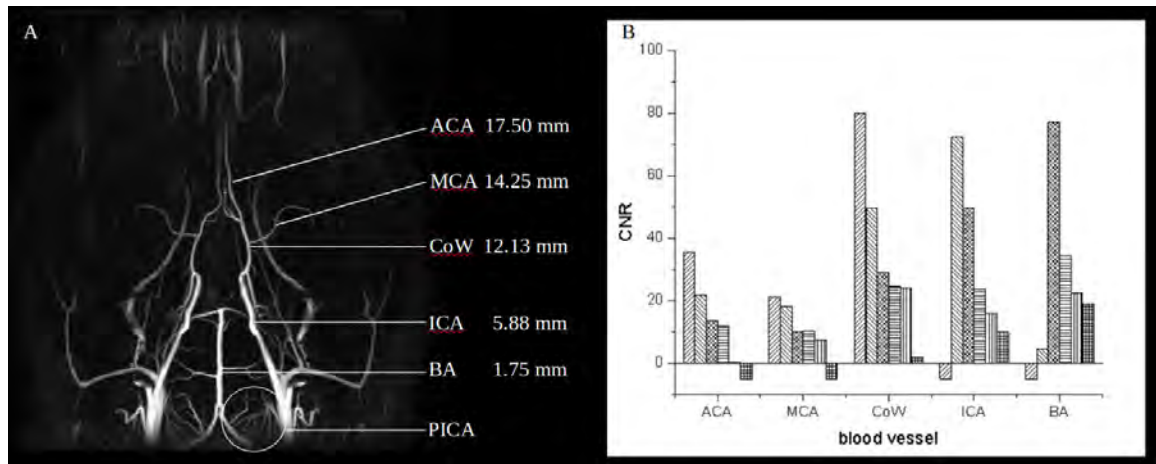


Figure 3.3: On the right (A), MR angiogram indicates the posterior internal cerebellar artery (PICA) region and the vessel regions that were analysed with respect to the isocenter of the magnet and the RF coil. On the left (B), contrast to noise ratio (CNR) depending on the center of the field of view (FOV) for the anterior cerebral artery (ACA), the middle cerebral artery (MCA), the circle of Willis (CoW), the internal carotid artery (ICA) and the basilar artery (BA). For each vessel, the left column represents the CNR of the most rostral FOV centre (10 mm to bregma), the right column highlights the most inferior centre below the brain (-15 mm to bregma).

manually segmented the images of all brain slices, set values outside of the skull to zero, and successfully reconstructed the angiograms with an improved SNR (figure 3.5 B). We were able to successfully identify smaller vessels like the hypothalamic artery (HTA), the anterior choroidal artery (AChA) as well as arterial branches of the peri-amygdoid complex and to the optical nerve (figure 3.5 C and D).

Visualization of the cerebro-vasculature of different rat strains

At baseline assessment, the average animal weight for the rat strains was different despite their similarity in age. Independently, the weight ranges for the different strain did not indicate the total brain volume, with Lister Hooded (LH) having the smallest and SD the largest brain sizes (figure 3.6).

All axial angiograms for the six different rat strains are displayed in figure 3.7. All strains have vessels branching off the circle of Willis in between the PCA and MCA. Generally, the SD and Spontaneous Hypertensive Rats (SHR) strain display a straight transition from the ICA towards the MCA that could potentially explain why these two strains are popular in transient ischaemia thread models. Without a significant meaning, we observed abnormal doubling branches from the circle of Willis in the left side of one SD rat, a very small circle in one Wistar Kyoto (WK)

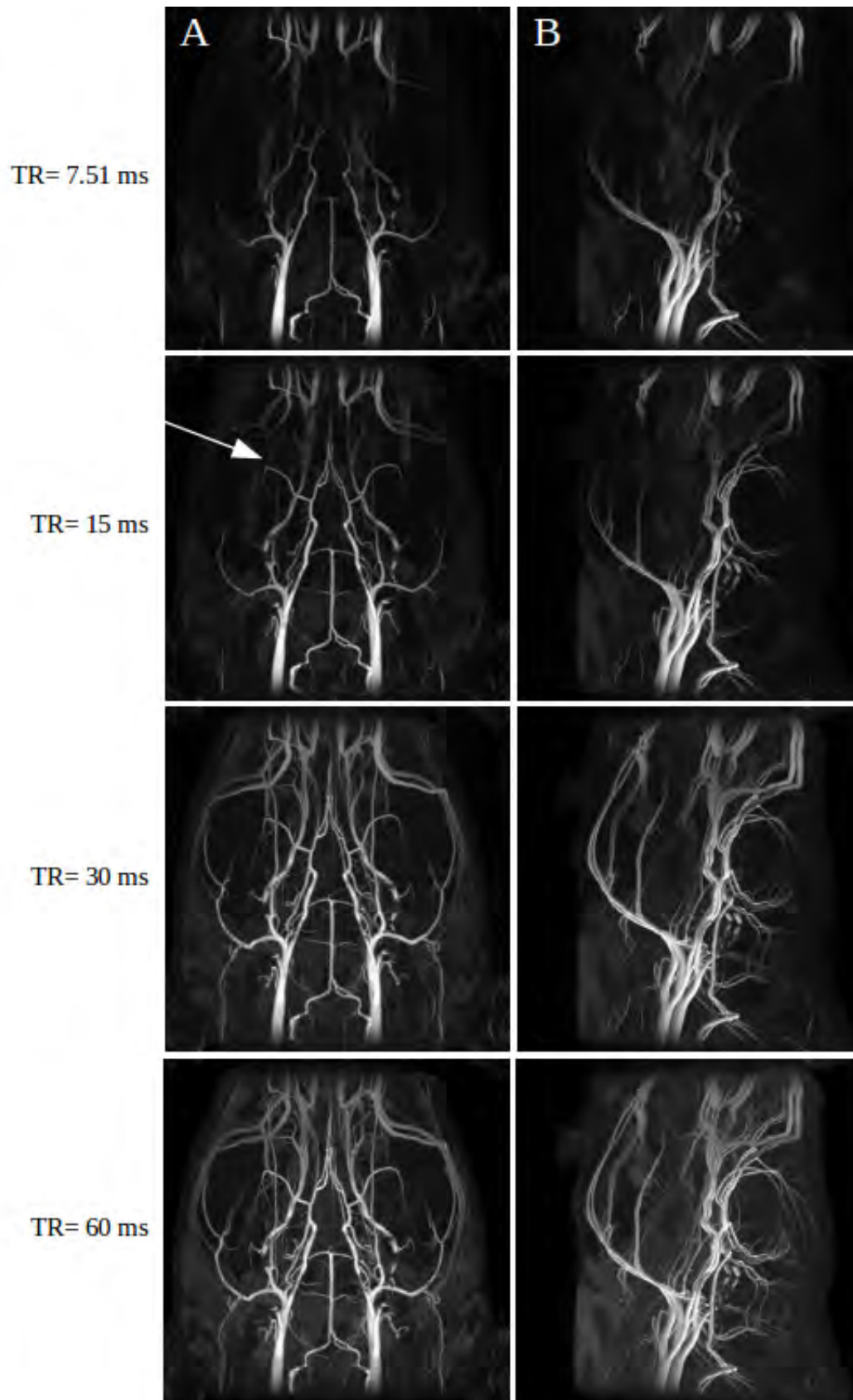


Figure 3.4: MR angiograms in Fisher 344 at four different repetition times (TR= 7.51, 15, 30, 60 ms) at a resolution of 125 μm in axial view (A) and sagittal projection (B).

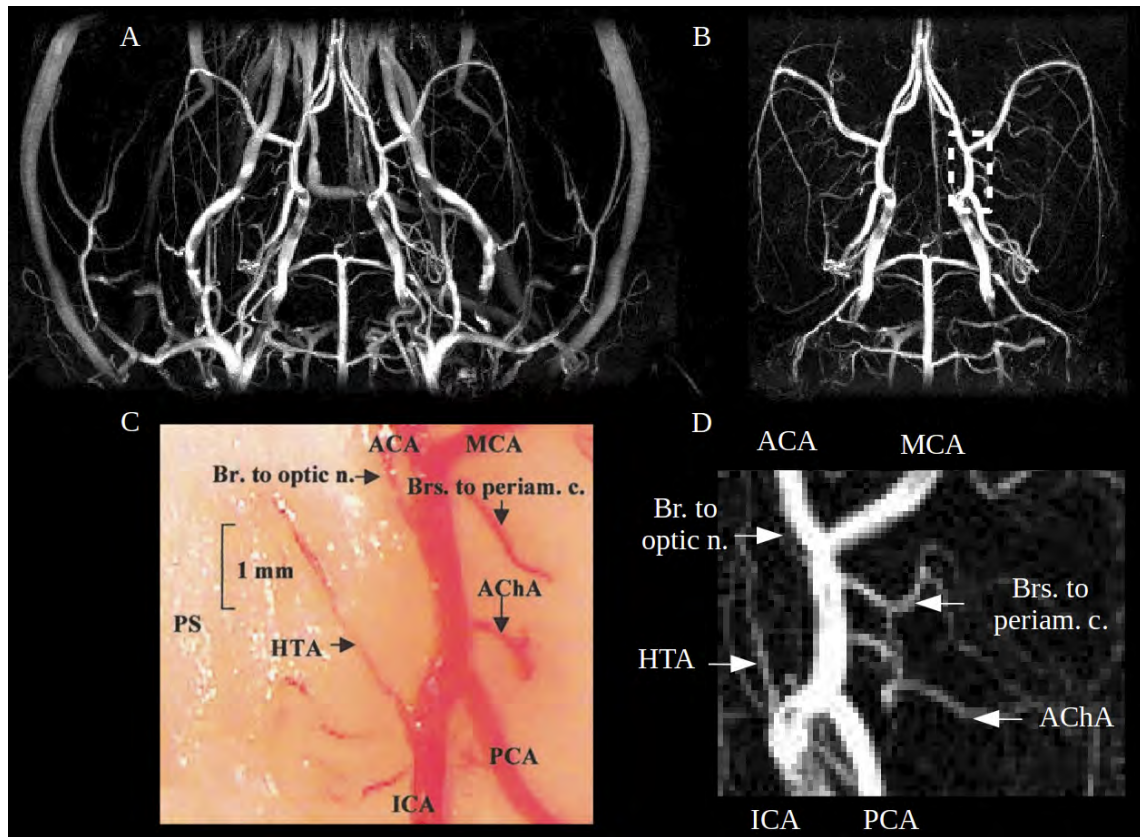


Figure 3.5: MR angiogram of the Fisher 344 rat, before (A) and following the removal of the extracranial signal on the height of the cranium (B) prior to applying the maximum intensity projection. The angiogram is acquired within 100 min with a resolution of $62.5 \mu\text{m}$. The post-processing not only simplifies the appearance but allows the direct identification of the smaller vessels branching from the circle of Willis. The lower two images compare the histological image for vessel identification (C from [64]) with a zoomed section (D) of the MRA. *Note:* internal carotid artery (ICA), posterior cerebral artery (PCA), middle cerebral artery (MCA), anterior cerebral artery (ACA), hypothalamic artery (HTA), anterior choroidal artery (AChA) branches off the peri-amygdoidal complex (Brs to periam. c.) and to the optical nerve (Br. to optical n.)

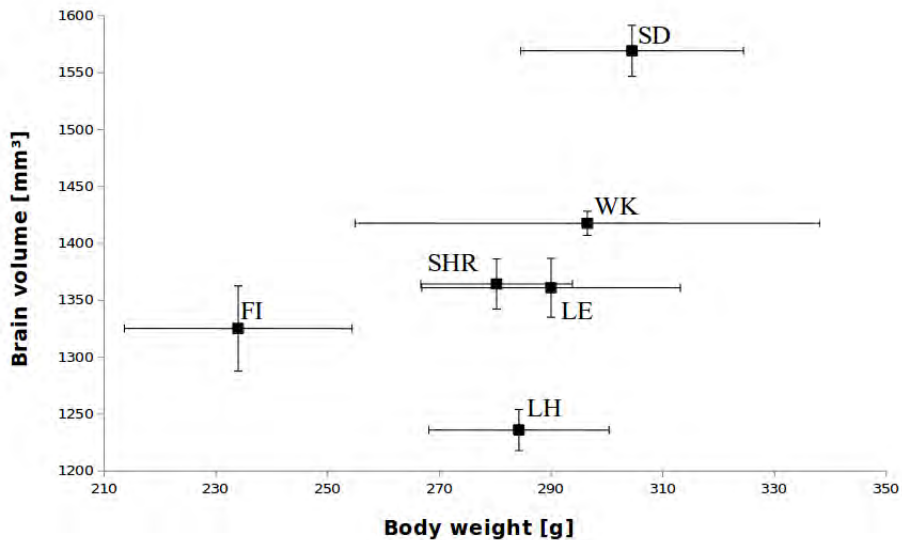


Figure 3.6: Total cerebral volumes determined by MRI versus body weight in six different rat strains: Sprague Dawley (SD), Wistar Kyoto (WK), Spontaneous hypertensive (SHR), Long Evans (LE), Fisher 344 (FI), Lister Hooded (LH).

rat (right side) and a long additional parallel vessel additional supplying the MCA territory in one Long Evans (LE) rat.

Frequent cerebro-vascular abnormalities of the MCA

To investigate the cerebro-vascular abnormality in a larger set of animals, we acquired a 5-minute angiogram with a reduced resolution of $250 \mu\text{m}$, 24 hours following a 60-minute transient ischemia ($n = 70$). Out of these, 45 animals had an infarct, an MRA examination and survived more than 24 hours, as lethargic animals were euthanized. The average volume of the infarct size was $192 \text{ mm}^3 \pm 119 \text{ mm}^3$ as determined by T2-weighted MRI (figure 3.8 A).

Although the resolution was reduced, it was still possible to observe the previously described vessel abnormalities. Six of the 45 animals had a double MCA, thus making a single thread MCA occlusion challenging, resulting in an average infarct size of $49 \text{ mm}^3 \pm 52 \text{ mm}^3$. In these animals, the lesions were significantly smaller affecting the hypothalamus and the internal capsule, indicating an occlusion of the HTA and AChA [64]. If these animals are removed from the study, the average infarct size increases to $216 \text{ mm}^3 \pm 110 \text{ mm}^3$ with a slightly reduced standard deviation. Ultra-high resolution angiograms 24 hours after reperfusion are displayed for SD rat (figure 3.9 A) and for SHR (figure 3.9 B), demonstrating the complete re-canalization of the MCA, the HTA and the AChA. For the SHR rat, the ACA of the affected hemisphere shows no signal intensity.

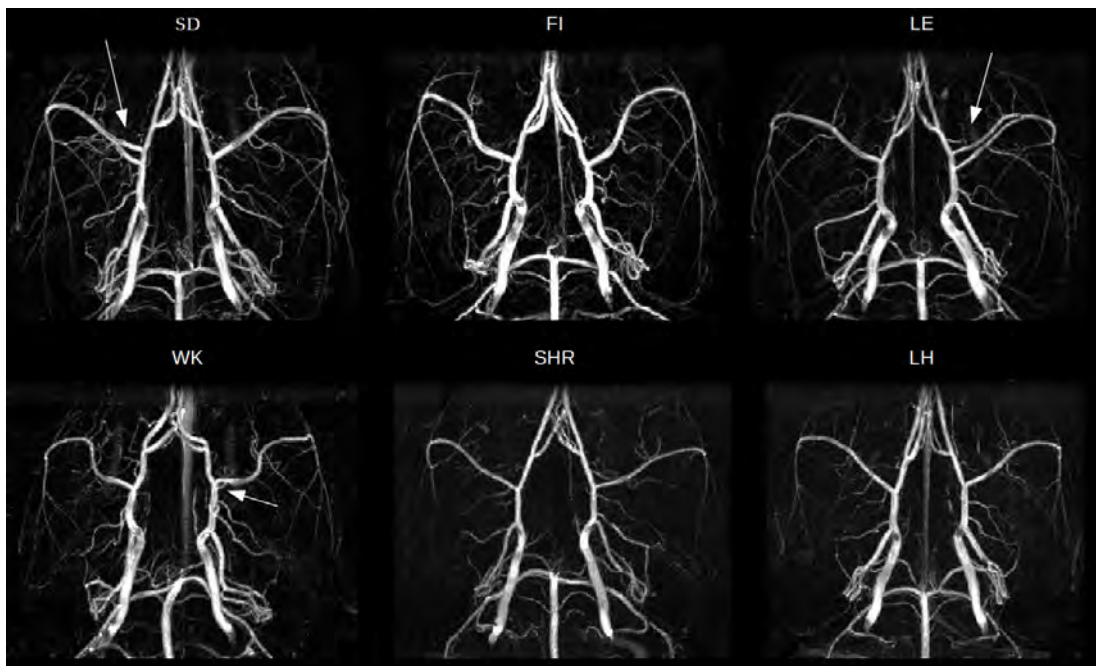


Figure 3.7: MR angiograms of six different rat strains: Sprague Dawley (SD), Wistar Kyoto (WK), Spontaneous Hypertensive Rats (SHR), Long Evans (LE), Fischer 344 (FI), Lister Hooded (LH). The displayed MRAs show in detail the anatomy of the cerebro-vascular system. The LE rat has an abnormal long pair of middle cerebral arteries (MCA) on the right, the WK has a close-range double branching MCA on the right, and the SD, a well separated double branching MCA on the left side.

3.4 Discussion

The high resolution TOF MRA benefits from the 40-mm resonator, which provides a high SNR with sufficient homogeneity over the sensitive volume, and from the increase in T1 at higher field. The anatomical reference, centring the slice selective MRA acquisition protocol at bregma, is suitable for all rat strains studied.

As the saturation of the stationary tissue depends on the flip angle and the TR, a nominal flip angle of 30 degree was chosen to visualize distal branches of the posterior, anterior and middle cerebral arteries [56]. The dependence of the in-flow delay should be similar for all rat strains, although the SHR strain potentially requires slightly longer TR. As vital parameters, like blood pressure and the partial pressure of CO₂, were not continuously assessed, this dependence would require detailed examination in a larger set of animals. It is important to note here that as we have used 50% oxygen and 50% nitrogen as the anaesthetic carrier gas, hyperoxia causes vasoconstriction and lowers the cerebral blood flow (CBF) [65][66], subsequently resulting in a decrease in T1 and an increase in T2 in mice [67].

Having said this, despite the increasing importance of MRA in clinical studies, the method is not widely used in animal experiments. This is mainly because it was

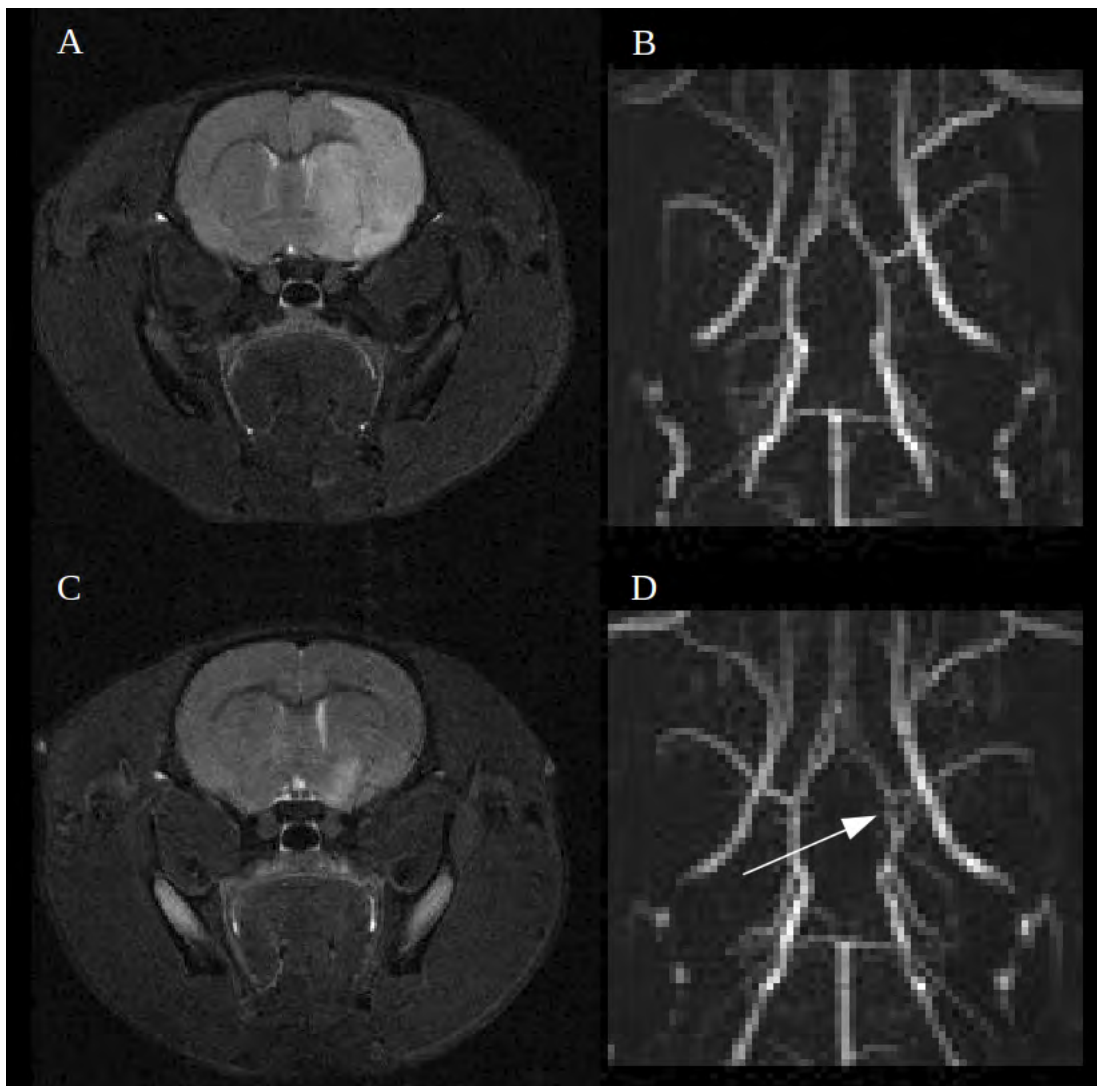


Figure 3.8: The top row displays a single slice MR image (A), reflecting a large infarct from an animal with regular MCA as can be seen in the angiogram (B). The bottom row displays a small focal lesion (C) of an animal that had a double MCA (D) as indicated by an arrow.

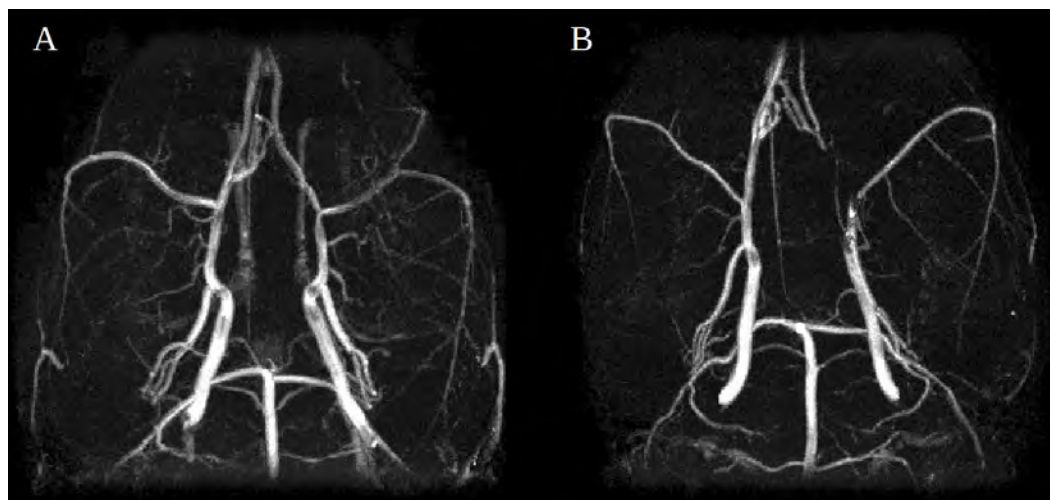


Figure 3.9: High resolution angiograms 24 h following a transient MCAO of a SD (A) and SHR rat (B) can be obtained despite the presence of a large vasogenic oedema.

observed that the use of contrast agent should be avoided when studying the process of arterial occlusive disorders [56]. As a trend, MRA in rodents is often performed using 2D multi-slice protocols, resulting in low resolution angiograms, [68][69] sufficient to visualize the occlusion side. Hereby, studies exploring the use of MRA in the detection and characterization of models of intracerebral aneurysm have been reported for mice [70]. Conversely, as demonstrated here at 11.7 T, an increase in field strength shall not only help IN a general increase in observable signal, but also offer the opportunity for an improved contrast in TOF-MRA due to an increase in the T1 relaxation times of the stationary signal arising from within the brain.

A 3D GEFC sequence was successfully optimized to identify even smaller vessels branching off from the circle of Willis. The centre of the FOV can be adjusted to yield the highest CNR for a specific vessel. Therefore, TOF MRA can be done at 24-48 hours after strokes, without the use of contrast agent. Roughly 13% of our animals have a 'double branched' MCA, which is in general agreement with previously reported values for SD rats [71].

Naturally, MRA can be used to pre-screen the batches of animals that might be subjected to MCAO. The pre-screening protocol has the advantage that outliers can be identified, and thus, only animals that meet the inclusion criteria would be subjected to an MCAO. A main disadvantage of protocols that pre-screen animals using MRA is that the study entails an additional session of anaesthesia prior to commencing the study. This additional step might increase the complexity of the scheduling, require an additional imaging session, and may add variability in the outcome and influence additional readout parameters like behaviour baseline. Importantly, the execution of MRA at the same time as the MR infarct size determination added an extra 5 minutes to the imaging session in our case to detect severe cerebral vessel abnormalities.

3.5 Conclusion

To sum up, we have successfully demonstrated the potential to acquire high-resolution MRAs on a case-by-case basis to reveal in detail the cerebrovascular system in a subgroup of animals and potentially identify compromised re-perfusion. Several imaging protocols of 3D flow compensated gradient-recalled echo sequence were utilized to evaluate the influence of the parameter settings on the spatial and temporal resolution. If the MRA acquisition protocol centres a suitable FOV at the bregma as anatomical reference, all major brain arteries of the rat can be visualized. The

characterised TOF-MRA protocols are suitable to be used without a contrast agent, to produce high-resolution angiograms at 11.7T. Flow compensated angiograms of Sprague Dawley, Wistar Kyoto, Lister Hooded, Long Evans, Fischer 344 and spontaneous hypertensive rats strains were obtained with a resolution of up to $62 \mu\text{m}^3$. Thus, the method is suitable to successfully detect one source of variability in the cerebro-vasculature subjected to transient MCAO. This finding might lead to a refinement in the study design to aid the development of novel therapeutics.

Chapter 4

Functional brain imaging

This chapter describes the two functional MRI (fMRI) studies on the blood oxygenation level dependent (BOLD) contrast. The chapter begins by a short introduction about neuroimaging techniques, and describes the mechanism underlying the BOLD contrast studied by fMRI at high field. In a second part, potential differences between α - and β -D-glucose have been investigated through an fMRI study. And finally, a new cine FLASH method is presented to improve the spatial and the temporal resolution in a functional research at 11.7T.

4.1 Functional imaging

4.1.1 Neuro-imaging techniques

Functional imaging techniques detect neuronal activity and brain function with a certain degree of invasiveness, and have a certain temporal and spatial resolution [73]. These techniques enable us to determine when and where neural activity in the brain is associated with a particular cognitive task. Non-invasive functional neuroimaging techniques, defined as techniques that produce images of brain without requiring surgery or any direct contact with the inside of the body, are available and are categorized into two main classes.

The first category of methods directly measures electrical activity associated with neuronal firing, such as electroencephalography (EEG) and magnetoencephalography (MEG) (figure 4.1). EEG is an electrophysiological monitoring method to record electric potential linked to the activity generated by an ensemble of neuronal cells. MEG allows us to record magnetic fields produced by electrical currents occurring in the brain, which is useful for mapping brain activity. These techniques provide excellent temporal resolution with a limited spatial resolution.

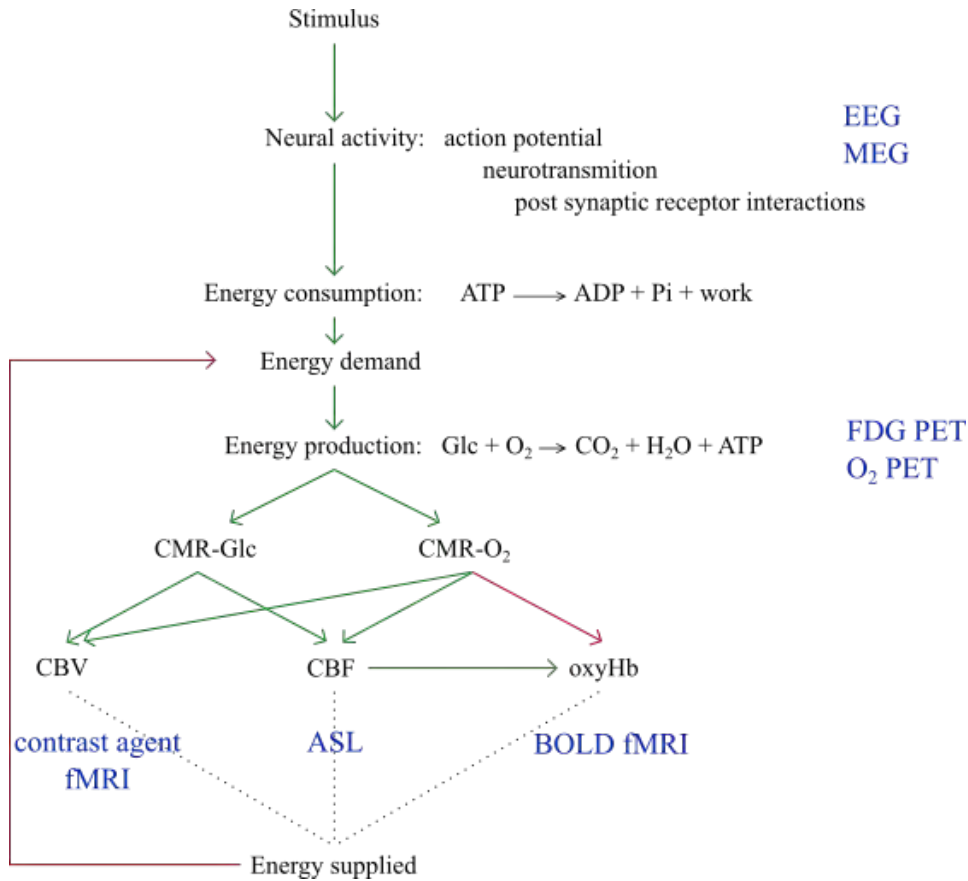


Figure 4.1: Schematic neuronal activity in response to a stimulus, and neuro-imaging techniques that were able to detect it. Neuronal activity might be detected by electroencephalography (EEG) and magnetoencephalography (MEG) as electrical activity. Following a stimulus, an energy consumption is induced by the neuronal activity, leading to an increase in energy production, principally glucose oxidation, and increase in cerebral metabolic rates of glucose consumption (CMR_{glc}) and cerebral metabolic rate of oxygen consumption (CMR_{O₂}). Due to a wide choice of radioactive tracers, positron emission tomography (PET) may measure these physiological phenomena. As glucose and O₂ must be supplied by the blood to the area of interest, cerebral blood volume (CBV) and cerebral blood flow (CBF) increase. Various MR methods are available. CBF can be measured by arterial spin labeling (ASL) methods while CBV is usually measured through the use of contrast agents. Due to local changes in blood oxygenation during activation, blood oxygenation level dependent (BOLD) might be utilized as endogenous functional contrast in functional MRI (fMRI) (figure adapted from [1] and [72]).

The second class consists of methods for indirectly measuring neuronal activity, such as positron emission tomography (PET), functional MRI (fMRI), and spectroscopic imaging (SI). These methods are based on the principle that neural activity is supported by increased local blood flow, and metabolic activity by the active population of neurons. In PET technique, the local increase in blood flow is measured through the injection of radioactive tracers such as $^{15}\text{O}_2$, an unstable oxygen molecule form that emits one positron to return to the stable form $^{16}\text{O}_2$. The use of 2-deoxy-2-[fluorine-18]fluoro- D-glucose (^{18}F -FDG) has emerged as a powerful and sensitive imaging tool for the detection of some brain diseases [74]. In a PET scan, the biggest advantage is the wide choice of radioactive tracers to measure physiological phenomenon such as CBF, cerebral blood volume (CBV), cerebral metabolic rate of oxygen consumption (CMRO_2) and cerebral metabolic rates of glucose consumption (CMRglc). Some major drawbacks of these invasive techniques, however, are the cost of PET facilities (camera associated with a cyclotron to produce the radioactive tracers) and the poor temporal resolution (on the order of one minute).

Various brain imaging methods are available in MRI that can measure metabolic parameters such as CMRglc and CMRO_2 and hemodynamic parameters as CBF and CBV. CBF is most commonly measured by arterial spin labeling (ASL) methods in which the water spins in the carotid arteries are perturbed, reducing T1 of the cerebral region of interest. CBV can be measured by contrast agents in which the signal from the blood compartment is eliminated. MR-SI might also be an alternative. Metabolic imaging might be possible by measurements of relative concentrations of compounds containing ^1H , ^{13}C or ^{31}P . The structure of the molecule is then resolved according to the resonance frequency in the spectrum. However, the spatial and temporal resolutions achieved are really poor.

Nowadays, fMRI technique is probably the most widely used brain functional imaging technique due to its relatively high spatial and temporal resolution to observe patterns of neuronal activity across the entire brain. Furthermore, when compared with other imaging modalities, fMRI can be entirely non-invasive. Three main complementary methodologies for fMRI can be identified. First, resting state fMRI uses correlations in the temporal fluctuations in a fMRI time series to deduce brain connectivity and to explore the brain network [75]. Diffusion imaging may also possible to provide input for tractography algorithms used for the reconstruction of the complex axonal fiber architecture [76]. Task based fMRI identifies functional areas in the brain related to a stimulus. fMRI techniques enables *in vivo* monitoring of CBF and two indices of energy metabolism: glucose and oxygen consumption [77].

Dependence of functional network: influence of anaesthesia

The choice of an anaesthetic is critically important as it influences not only the animal's physiology but also some artefacts due to motion and stress [78]. Indeed, motion artefact is an inherent problem in fMRI studies as it can input distortion of the image and generate changes in signal intensity that can be wrongly interpreted as changes in brain activity induced by a stimulus. Conscious imaging is possible mainly in studies conducted to understand the neurobiology of the brain activity behaviour involving cognition and emotion. During the imaging session, different methods have been developed to restrain animals [78] [79]. However, to minimise motion artefact, anaesthetics might be used although it depresses the neuronal activity during the MR experiment.

Functional MRI experiments are performed under sedation or light anaesthesia although specific care must be taken to prevent animal movement, suffering and stress while allowing stimulatory paradigms. Indeed, each anaesthetic has a characteristic effect on both neural activity and on hemodynamics parameters. Recently, Haensel et al. published a review describing anaesthetic regime (induction and maintenance) and their effect on physiological parameters [80]. In preclinical rodent experiments, anaesthetics and/or sedatives, such as isoflurane, halothane, α -chloralose, urethane, pentobarbital, propofol and medetomidine, have been used for both induction and maintenance purposes.

Isoflurane is the mostly used inhalation anaesthetic in laboratory animals [81] as it shows potential for longitudinal exams. At a higher dose, isoflurane as vasodilatory agent may increase the CBF baseline and influence the neurovascular interactions. Widely used for anatomical imaging in rodents, isoflurane can also be used for fMRI studies at low concentrations, obtaining an average BOLD change during forepaw stimulation of around 2%–3% [82]. Like isoflurane, halothane is known for its vasodilatory properties, resulting in increased baseline CBF. Despite this effect, it is one of the most commonly used inhalation anaesthetics in *in vivo* studies [80].

In preclinical neuroscience research, α -chloralose was a widely used anaesthesia for fMRI studies in the rat. However, it is not suitable for longitudinal experiments as it requires the animals to be intubated and mechanically ventilated; so the experiment should then be terminal as the product is carcinogenic [83]. Urethane might

also be appropriate to study neurotransmitter systems due to its limited actions on several receptor types [84]. Besides its carcinogenic nature, urethane presents some disadvantages in the form of hyperventilation or lowering of heart rate and blood pressure. Barbiturates, such as pentobarbital, might have a profound effect on brain functioning [85]. They are known to depress cerebral glucose metabolism as well as respiratory and cardiovascular function, thus decreasing the CBF. Propofol might also be used for fMRI according to the adequate requirement levels of anaesthesia to minimise alteration network of functional connectivity [86].

Nowadays, medetomidine is gaining in popularity as an anaesthetic for rodents in fMRI since it is also suitable for longitudinal studies [83]. Signal changes during forepaw stimulation are similar to those observed under isoflurane, which is on the order of 2%–4%, and therefore, there appears to be a wider range of acceptable anaesthetic depths [83]. Providing sedation, this analgesic and relaxation agent can change the baseline of physiological conditions such as bradycardia and increased blood pressure that might affect the fMRI responses [87]. As anaesthesia with isoflurane produces hyperglycemia, a sedation with medetomidine is then preferred in case of fMRI [88]. The protocol described in the following chapters is designed to be applied in the future to follow the functional recovery following cerebral ischemia in rats. We thus decided to implement the anaesthetic mode with medetomidine.

4.1.2 BOLD functional MRI

As a non-invasive fMRI technique, local changes in blood oxygenation during activation might be utilized as endogenous functional contrast [89]. This phenomenon is called BOLD contrast and was introduced by Owaga et al. [90]. In the following section, some basic principles related to the BOLD effect are explained in order to fully understand the methods presented in this work.

Magnetic properties of haemoglobin

The basics of BOLD contrast depends on local change of magnetic susceptibilities due to the rate of oxygenation of the haemoglobin.

Blood can be approximated as a two-compartment system containing plasma and red blood cells. Red blood cells contain haemoglobin with four heme groups associated by an iron, a histidine unit and potentially the presence of a molecule of oxygen (figure 4.2). The main function of haemoglobin is to transport oxygen through the vascular network and two states are possible, oxyhaemoglobin (bound with oxy-

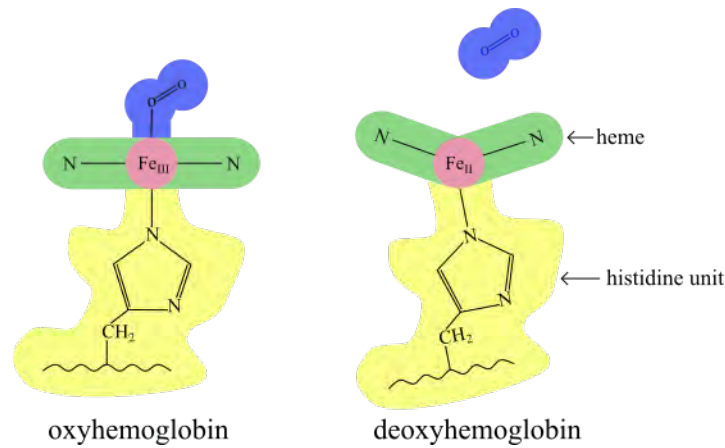


Figure 4.2: Schematic diagram of oxyhaemoglobin and deoxyhaemoglobin with the oxygen O_2 bounding, the heme groups and the attached histidine unit.

gen) or deoxyhaemoglobin. The oxygen content changes the local susceptibility in the blood. In fact, haemoglobin in the deoxygenated form is more paramagnetic with a lower magnetic susceptibility than the rest of the tissue [6]. However, the haemoglobin in the oxygenated form has the same susceptibility as of the tissue (more diamagnetic).

Within a magnetic field, microscopic field inhomogeneities are created around the deoxyhaemoglobin and around blood vessels containing deoxyhaemoglobin leading to an attenuated MR signal. The spin dephasing in deoxyhaemoglobin is bigger than in oxyhaemoglobin leading to a shorter T_2/T_2^* of the tissue and decrease in the MR signal amplitude. When haemoglobin is bound to oxygen, the local magnetic field gradient is reduced as the susceptibility of the blood becomes similar to the tissue. The MR signal amplitude increases by 1-4% as the T_2/T_2^* of oxyhaemoglobin is bigger. This change creates a small MRI signal increase. The BOLD strength depends on B_0 , and the higher magnetic susceptibility of deoxyhaemoglobin compared to oxyhaemoglobin raises about 1% per tesla (T) [6]. The utilisation of higher magnetic field may enable the measurement of BOLD changes in the capillaries network.

The hemodynamic response function (HRF)

As neural activity is not a direct measure, the classical approach to estimate the brain activity is through the energetic demand and the increase of blood flow. The most common functional MRI (fMRI) use has been to localise areas within the brain that are activated in response to a certain task. Some images will be taken while stimulation is applied and some will be taken with the subject at rest. The BOLD contrast exploits the differences in magnetic susceptibility of oxyhaemoglobin and deoxyhaemoglobin as a result of increased CBF during stimulation.

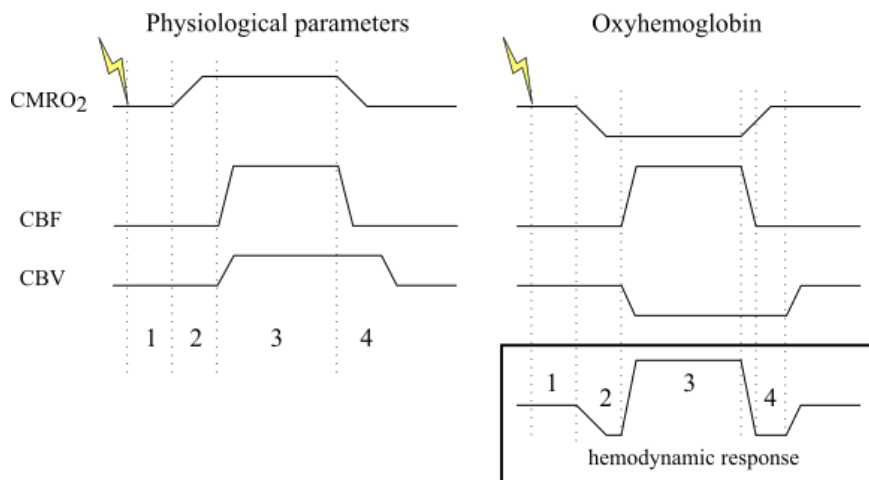


Figure 4.3: Physiology of the blood oxygenation level dependent (BOLD) effect depending on the metabolic rate of oxygen consumption ($CMRO_2$), the cerebral blood flow (CBF), the cerebral blood volume (CBV) and their effects on the concentration of deoxyhaemoglobin and the hemodynamic response. (1) represents the energy consumption due to the neurotransmission, (2) the initial 'dip', (3) the so called BOLD response and (4) the signal undershoot (figure adapted from [6]).

The complete physiology of the BOLD response is beyond the scope of this thesis, although several excellent literature reviews have been published [89][91][92]. In the first approximation, the physiology of the BOLD effect can be simplified and depends on the following physiological parameters: the CBF, the CBV, the $CMRO_2$ and the CMR_{glc} . Figure 4.3 adapted from [6] shows the effect of neuronal activation on physiological parameters and their influence on the signal intensity:

1. First, neuronal activation requires energy. Neuronal activity might be defined as an electrical passage across the cell membrane of the axon and is called the action potential. When the neuron is activated, this impulse causes neurotransmitters to be released by the terminal buttons, this process is called neurotransmission. Then, the equilibrium state must be re-established to be ready for another action potential. Also, the intra-extracellular ion balance must be rebuilt, and the neurotransmitters must be recycled. The restoration of the equilibrium state leads to an increase in energy consumption and needs an increase in energy production mainly by the oxidation of glucose.
2. The energy production leads to an increase in CMR_{glc} and an increase in $CMRO_2$. More oxygen is consumed due to the activity of mitochondria in the 'activated' neurons. The concentration of deoxyhaemoglobin is increased leading to a slight shortening of the transverse relaxation times T_2/T_2^* . In BOLD fMRI, this leads to a signal reduction called the initial 'dip'. Unfortunately, these changes are really small, and thus, the small 'dip' cannot be

reliably detected.

3. This increased demand must be supplied by the blood, leading to an increase in the CBF and the CBV to deliver more blood to the site of neuronal activation. CBF increases while $CMRO_2$ stays equal in the same area. In response to a stimulus, the relative amount of deoxyhaemoglobin inside red blood cells decreases, reducing the disturbance of the magnetic field. The relative concentration of oxyhaemoglobin increases, leading to an increased signal intensity in T_2/T_2^* weighted images. As energy substrates are provided through the circulation, CMR_{glc} and $CMRO_2$ would increase in parallel.
4. After the peak, the BOLD response decays. $CMRO_2$ and CBF then return to their baseline values. The relaxation of CBV is slower. During a certain time, there is still an increase of relative concentration of deoxyhaemoglobin. This results in a signal undershoot of a few tens of seconds.

The so-called BOLD contrast is typically positive when comparing an ‘activated’ state with a ‘baseline’ state. The BOLD signal is a function of various intra- and extravascular contributions, the magnetic field strength, echo-time, pulse sequence, blood vessel size and orientation.

Several by-products of neural activity are dependent on neuronal and glial metabolism, for example lactate has vasoactive effects and is supposed mediators of coupling. Formed with a certain delay (few seconds) after the initiation of neuronal activity, the coupling neuronal activity with CBF is unlikely to be exclusive. Neurotransmitters, especially glutamate (Glu), cause neurons and astrocytes to activate a chain of intracellular events, for example, causing the neuronal release of nitric oxide (NO), probably a key element in coupling [72]. Further, this neurotransmitter feed-forward controls constriction and dilation of the blood vessels.

An increase in blood flow in response to a specific stimulus is referred to as a hemodynamic response function (HRF). A linear combination of one or two gamma functions is used to model the rise of the HRF and the undershoot after 10-30 seconds usually. Assuming a same HRF for all the voxels is usually not appropriate [93]. HRFs shape across subjects and brain regions may vary in shape or magnitude because of factors such as vasculature network, differences in neural activity, haematocrit concentrations or baseline of CBF. True response may be faster/slower or with a smaller/bigger undershoot.

4.2 Differences between α and β glucose through an fMRI study

Although comprising only about 2% of the body weight, the brain consumes almost 20% of the total energy through oxygen and glucose blood supply. Neural activity may be modulated by metabolism-dependent mechanisms [74]. During neuronal activity, additional glucose can be processed anaerobically through glycolysis rather than through the tricarboxylic acid (TCA) cycle and oxidative phosphorylation [77]. Functional studies are often performed using FDG-PET to measure changes in glucose uptake and consumption. In the first part of this chapter, we investigated and compared the influence of the two main D-glucose anomers, α - and β -D-glucose, on the BOLD response by fMRI.

4.2.1 Coupling of neural activity, blood flow and energy metabolism

Glucose metabolism

In the brain, glucose is entirely oxidised to carbon dioxide (CO_2) and water through sequential processing by glycolysis (figure 4.4 A), the tricarboxylic acid (TCA) pathways (figure 4.4 B) and the associated oxidative phosphorylation (figure 4.4 C). The brain concentration of glucose is around 1 mmol L^{-1} which produces between 30 and 36 adenosine tri-phosphate (ATP) per molecule of glucose [6]. ATP is a small molecule which transports chemical energy within cells for metabolism.

Correlations between the glucose metabolism close to the synapse and the HRF in the blood vessel remains unclear. The production of ATP through the pyruvate depends on the presence of oxygen [92]. Glucose can be metabolised in an aerobic environment to produce energy fuel through the neuronal glucose metabolism and the vascular oxygen supply. In anaerobic conditions, the glucose is delivered through the blood vessel. The increased proportion of oxyhaemoglobin is thus a consequence of an increase in CBV.

Pyruvate can also be converted to lactate by astrocytes, and subsequently transferred to neurons for oxidative metabolism [94]. In neurons, lactate is then reconverted to pyruvate through to oxidative metabolism. Lactate then becomes the major source of neuron energy metabolism even if this remains controversial [92].

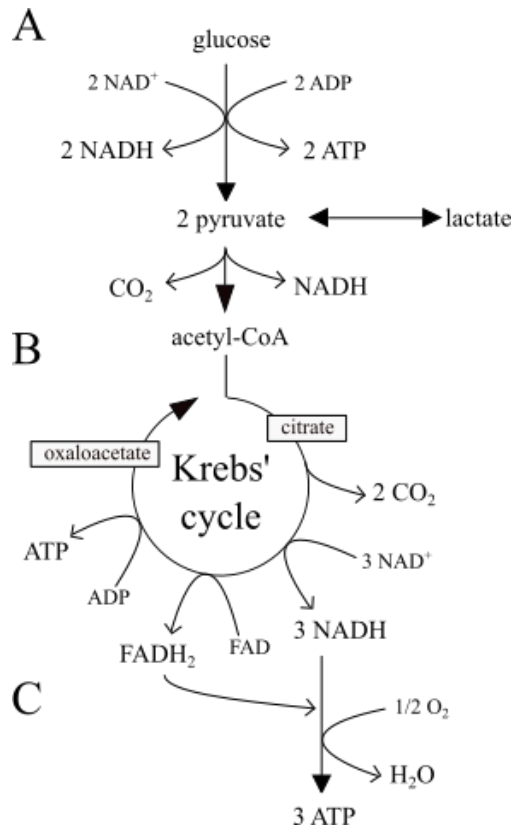


Figure 4.4: Glucose entirely oxidised to carbon dioxide (CO₂) and water through sequential processing by glycolysis (A), the cycle of Krebs (B) and the oxidative phosphorylation (C).

Anomeric form of glucose

Glucose exists in two configurations with an equilibrium of 36% for the α anomer and 64% for the β anomers but both forms are generally referred as D-glucose.

β -D-glucose is almost twice as abundant as α -D-glucose at anomeric equilibrium [95]. As it has been reported by Malaisse, the difference between α - and β -D-glucose metabolism differs as a function of temperature, concentration, metabolic pathway and cell types [95]. Thus, the glucose challenge by a specific D-glucose anomer might be solely explained by peripheral effect (*e.g.* liver, pancreas) rather than direct effect on neural activity response. Moreover, with respect to *in vitro* studies of rat adipocytes, the glycolytic pathway indicates an anomeric specificity with preference for α -D-glucose [96]. α -D-glucose is metabolised more efficiently than β -D-glucose when α -D-glucose and β -D-glucose are present together. Interestingly, in the *in vitro* rat brain cells study performed at 9°C, brain hexokinase displayed a higher affinity for β -D-glucose but a higher glycolytic pathway velocity for α -D-glucose [97]. Generally, studies with changes in glucose concentration have to consider if the observed effects are caused by glucose uptake and/or consumption.

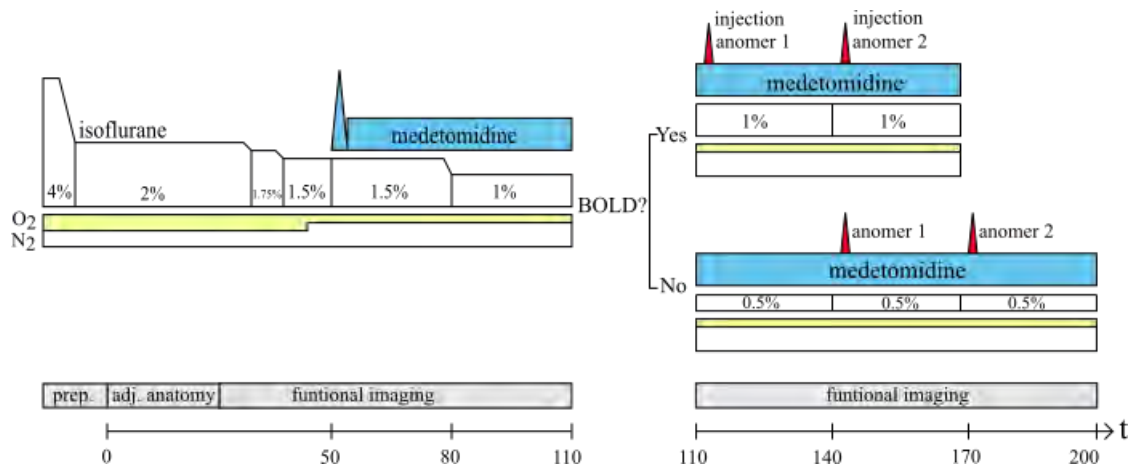


Figure 4.5: Typical work-flow of a fMRI experiment with injection of the two main anomers of D-glucose.

4.2.2 Method

All experiments were performed using a Bruker Avance 11.7 Tesla (500 MHz) described previously. The 40-mm ^1H resonator (Bruker GmbH, Karlsruhe, Germany) was used for signal transmission and reception. The schematic study protocol is illustrated in figure 4.5.

In vivo model: Animal preparation

Healthy male Sprague Dawley rats ($n=21$, 282-531g, Janvier Labs, Saint-Berthevin Cedex, France) were used for the experimental protocols. The animals were initially anaesthetized with 3-4% of isoflurane within the induction chamber. The tail vein was cannulated to inject anomers of D-glucose and to collect blood sample. The animal was then placed in sphinx position in an MRI-compatible cradle, with the head of the anaesthetized animal carefully secured by tooth and ears stereotactic fixations.

For administration of medetomidine, an infusion line was subcutaneously inserted into the animal's flank. As medetomidine increases the renal clearance, a sanitary napkin was placed under the animal to absorb urine. Two silver electrodes were inserted under the skin in each of the forepaws. The rectal temperature was kept at $37 \pm 2^\circ\text{C}$ and spontaneous respiration was maintained to under 90 breath per minute. Isoflurane (2%) in 50% oxygen and 50% nitrogen was delivered via a nose cone, and the animal was brought to the MR room and positioned in the magnet isocenter.

Imaging protocol

Once the animal was placed in the scanner, the MRI session starts with high resolution scans were acquired (15 minutes) for the adjustment of anatomy. The MRI session started with automated parameter adjustments for reference pulse gain and resonance frequency, a global shim (x, y, z, and z2). A pilot scan followed by a fast scout scan using a self-gated FLASH sequence of three 1-mm thick slices in axial, sagittal, and coronal orientations was performed. Two RARE scans in axial and coronal orientation were acquired for anatomical references (TE = 12 ms, TR = 3000 ms, FOV = 40 mm, matrix = 256 * 256, spectral width = 50 kHz, slice thickness = 1 mm, 28 continuous slices, RARE factor = 8). The slice offset of the position of the somatosensory cortex was identified 5 mm posterior to the rhinal fissure [98]. One axial 1-mm slice was acquired. For acquisition of the fMRI scans, SE-EPI was performed with an in-plane resolution of $625\mu\text{m}^2$ (TE = 30 ms, TR = 3000 ms, FOV = 40 mm, matrix = 64 * 64, spectral width = 200 kHz). To produce the electrical pulses (6 Hz, 3.0 mA, 0.3 ms width), the program triggered by a pulse generator was utilised and interfered between the pulse program by a transistor transistor logic (TTL) outputs.

During the transition from a pure isoflurane anaesthesia to a final anaesthetic protocol, individual short fMRI scans were acquired. Short scans consisted of three blocks of 30 seconds without stimulation, 30 seconds with forepaw stimulation and 30 seconds without stimulation, leading to a total acquisition time of almost six minutes per scan. Between short scans with electrical stimulation, the isoflurane percentage was decreased to 1.5% and the O₂:N₂ gas mixture was changed from (50:50) to (30:70).

Thereafter, long scans of fifteen blocks of 30 seconds forepaw stimulation followed by 90 seconds resting condition were then acquired, leading to a total acquisition time of 30 minutes per scan. Concurrently, with the first long scan, a 0.1 mg kg⁻¹ medetomidine (Domtor, Esteve) was injected subcutaneously in a 500 μl bolus, followed by a constant infusion at 1 mL h⁻¹. A second long scan with electrical stimulation was then performed while the isoflurane percentage was decreased to 1%. If a BOLD response was detected, one anomer D-Glucose was injected intravenously at the concentration of 10 mmol in 0.5 mL. If no clear BOLD response was detected, a third long scan with electrical stimulation was then performed while the isoflurane percentage was decreased to 0.5%. The two main anomers α - and β -D-glucose were injected alternatively and in a random fashion leading to two sets of experiments:

- 1: injection of α -D-glucose followed by 2: injection of β -D-glucose.

- 3: injection of β -D-glucose followed by 4: injection of α -D-glucose.

Data processing

Activation maps were obtained using the FUN tool of ParaVision 5.1 (figure 4.6). Prior to any further processing, stimulation-induced activation maps indicated the difference between experimental fMRI data acquired during stimulation versus the resting periods, on a pixel-by-pixel basis. As shown in figure 4.6, the top left shows an original SE-EPI image, and on the top right, the activation map is displayed. It highlights the difference between the average signal intensities between rest and stimulation. As the two first images of the time series are potentially not reaching the steady state, they were discarded. The time series of the activated pixels of the somatosensory cortex were extracted and were averaged for each fMRI experiment in every animal.

To improve the statistical power for each animal, five consecutive images were averaged (figure 4.7). This resulted in a reduction from 40 to 8 data points. To obtain the percentage change, the intensity S_3 of data point 3 is subtracted to the intensity S_n of data point n according to:

$$\Delta_{BOLD} = \frac{S_n - S_3}{S_3} * 100 \quad (4.1)$$

For statistical comparison, Δ_{BOLD} is calculated for $n = 4$. The first stimulation Δ_{BOLD} was then set to 1 to normalise all subsequent stimulation blocks. As signal intensity of stimulation bloc two is severely affected by the glucose anomers, the data was discarded. To statistically compare the four groups, a two-way analysis of variance (repeated ANOVA) followed by Tukey or Fisher's post-hoc test. Statistical significance was taken at $p < 0.05$.

4.2.3 Results

None of the twenty one animals displayed a BOLD response under deep anaesthesia with 1.5-2% isoflurane. All animals showed a robust response prior to the injection of the glucose anomer. Several of the animals required a lower isoflurane of 0.5%. The group time courses were averaged as displaced in figure 4.7.

The average HRF is also shown in figure 4.8. In none of the groups, an onset of the peak could be identified three seconds after the start of the stimulation. Subsequently, the HRF showed a peak six to nine seconds after the start with the sub-

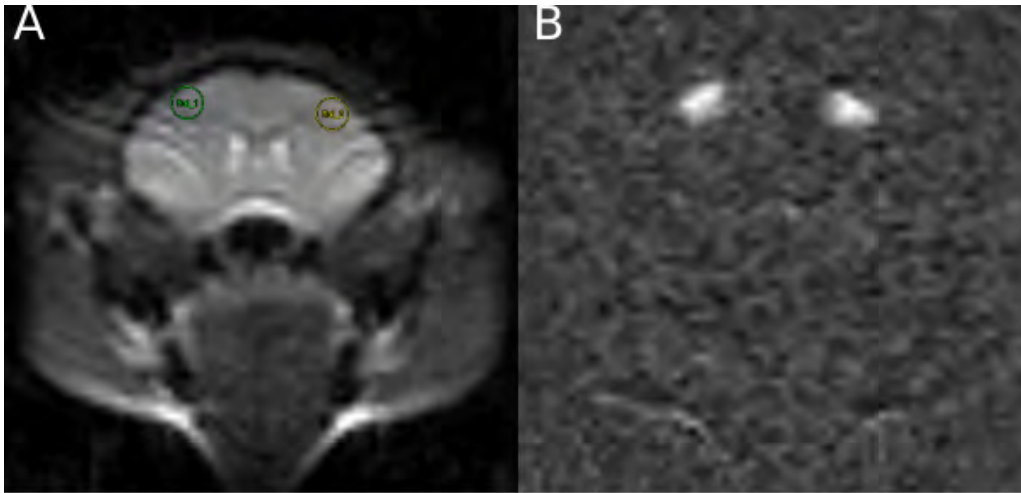


Figure 4.6: An original SE-EPI image (A) and its corresponding activation map obtained using the FUN tool of ParaVision 5.1 (B). The stimulation-induced activation maps indicates the difference between experimental fMRI data acquired during stimulation versus the resting periods, on a pixel-by-pixel basis.

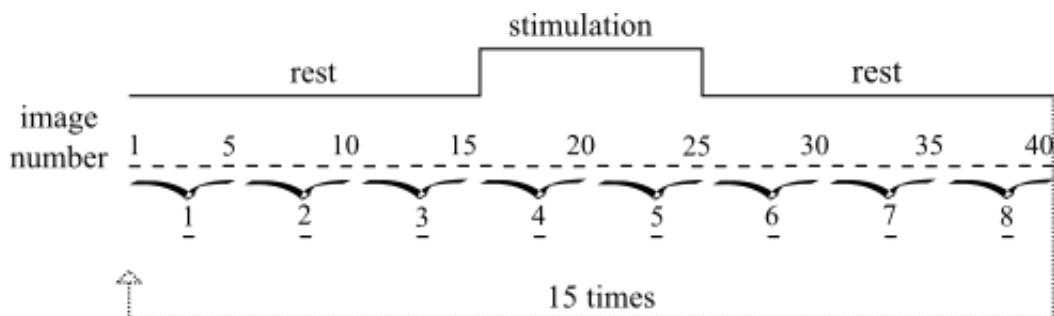


Figure 4.7: Typical workflow of a fMRI analysis to estimate the effect of the two main anomers of D-glucose on the BOLD response

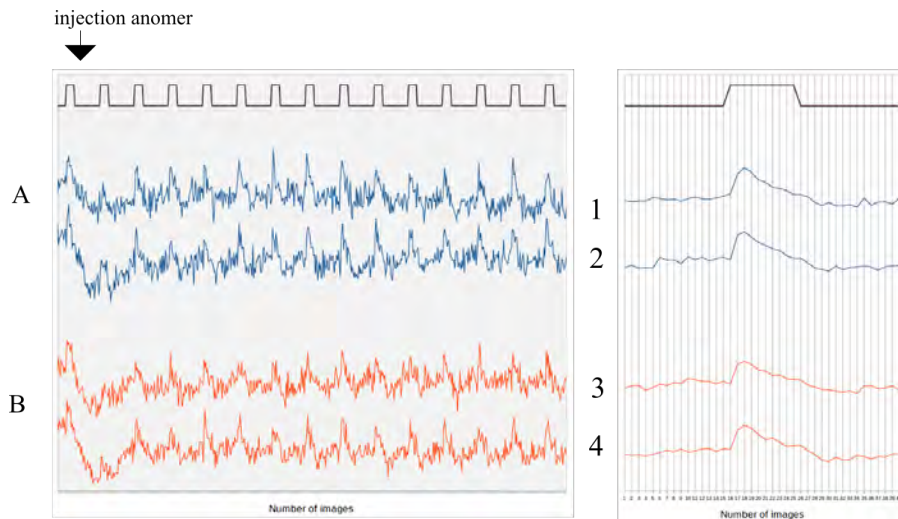


Figure 4.8: Similar blood oxygenation level dependent (BOLD) response observed after injections of D-glucose anomers. α -D-glucose (group 1) was first administered followed by β -D-glucose (group 2). In a second set of experiments, β -D-glucose (group 3) was first infused followed by α -D-glucose (group 4).

sequent decline to the baseline during continuous stimulation. A slight undershoot of the signal intensity could be identified. The somatosensory cortex stimulation produced all signal changes between 0.5% and 1.8% signal intensity. Normalising the signal change to one allowed four potential signal alterations following the injection of glucose. As the intravenous injection of glucose resulted in a lower baseline intensity, inner constant baseline was reached at stimulation block 3 (figure 4.8).

In figure 4.9 A, the BOLD response of the first injection of a glucose anomer is displayed (group 1 and 2). Figure 4.9 B shows the average BOLD response following the second injection of glucose (group 3 and 4). As can be seen, the first injection of α glucose results in an increase of the BOLD response (group 1) whereby the initial injection of β glucose results into a lower BOLD (group 2). The response to the injection 1 was highly significant ($p < 0.05$). The significant differences between the group is less clear if considering the individual time points after administration. Significant values could be obtained at p values. Thus, given the variability of the data, the duration of the effect cannot be established. No significant differences in any other comparison could be observed ($p > 0.05$). However if the injection of β -D-glucose is followed by a second injection of α (30 min), an increase in the BOLD response can be observed. A contrary trend can be observed if the α -D-glucose injection is followed by a β injection (30 min later). The mean BOLD response in both experiments had a characteristic response peak at approximately 3 seconds after the stimuli.

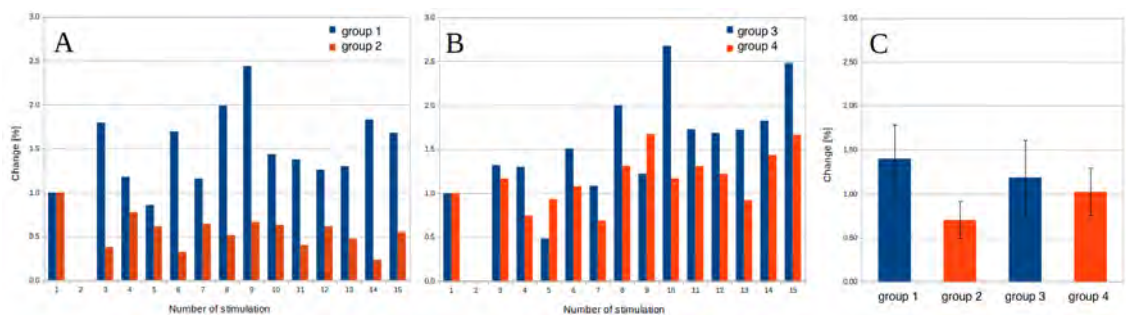


Figure 4.9: BOLD response normalised to the signal obtained through the first stimulation in the experiment. In the first set of experiments (A) α -D-glucose (group 1) was first administered followed by β -D-glucose (group 2). In a second set of experiments (B), β -D-glucose (group 3) was first infused followed by α -D-glucose (group 4). All the normalised intensity are averaged accordingly (C).

4.2.4 Discussion

This study deployed a SE-EPI method to observe the BOLD effect. As we have conducted the study at 11.7T, the magnetic field is usually distorted in the brain area, in brain-tissue interface, causing artefact in GE-EPI images. Moreover, SE-EPI is sensitive to change in oxygen concentration in capillaries, whereas GE-EPI suffers from large vessels' contributions. A major drawback of SE-EPI is its reduced sensitivity to BOLD contrast. Likely, SE-EPI exhibits lower susceptibility to physiological fluctuations, especially to the respiratory contributions, leading to lower field variations related to thorax motion [99]. Furthermore, at high magnetic field, SE-EPI for fMRI study is preferable [91].

The amplitude of the BOLD response is influenced by the stimulation frequency [87]. In our study, we chose to stimulate the forepaws (6 Hz, 3.0 mA, 0.3 ms width) under a mixture of medetomidine-isoflurane anaesthesia. The frequency of the stimulus under medetomidine should be similar as that under isoflurane [100]. As the HRF depends on the stimulus duration and frequency in the forepaws stimulation model, this frequency yielded consistent response. In fact, for a 30 seconds stimulus duration, the HRF should be largest at frequencies of 8-12 Hz during the earliest period whereas the responses should be largest at frequencies of 6-8 Hz during the later stimulus periods [82].

In the current study, we were able to significantly detect the changes in the BOLD response in animals anaesthetized with medetomidine following the administration of D-glucose anomers. Significant BOLD signal was observed after forepaws stimulation within the somatosensory cortex. It appears that an injection of α -D-glucose increases the BOLD response whereas the injection of β -D-glucose decreases the BOLD response. Importantly, due to practical considerations, the experimental

protocol was designed keeping in mind the following constraints:

- To ensure solubility to either anomers in 0.5 mL of saline, we decided to inject the same amount of glucose and not adjust the concentration according to the body weight.
- The study of 21 animals was performed over three weeks in a single 'batch' of animals, resulting in a large variation of the body weight, from 282 g to 531 g.
- During an experimental day, we were able to acquire two full data sets. As the animals had free access to food and water, the baseline glucose levels may vary substantially. Indeed, the values following the induction of anaesthesia was 97 ± 36 .
- As blood sampling is potentially influences the MRI experiments, no additional blood sample was taken prior to the injection of the D-glucose anomer. Hereby, the fluctuation in glucose levels caused by the complex anaesthetic transition to isoflurane to medetomine. We are aware that the glucose levels are unknown but random. Also, although the required glucose sample was 10-20 μL , the volume to be extracted from the animal placed in the center of the magnet was 700 μL .

Despite the potential large variations in baseline glucose, differences between α and β could be identified. Additional studies can be conducted to reduce the above potential variabilities. Hereby, a faster MR protocol for fMRI with respect to the anaesthetic regimen might be most promising. Having said this, the observed difference between groups may currently only be proven with respect to these specific anaesthetic conditions. Futures studies will show if a selective effect on the BOLD response could be observed with different anaesthetic protocols and in a conscious rat. Ultimately, one might speculate that the difference is translatable to human fMRI.

The HRF observed at the baseline and following the administration of glucose yielded a late onset peak response. To explore this aspect on the neurovascular coupling, we performed a high resolution fMRI study using the cinematographic FLASH (chapter 4.3).

4.3 Cinematographic FLASH

As observed in the study and as described previously, with a temporal resolution of three seconds, the BOLD response of the forepaws stimulation has a late onset

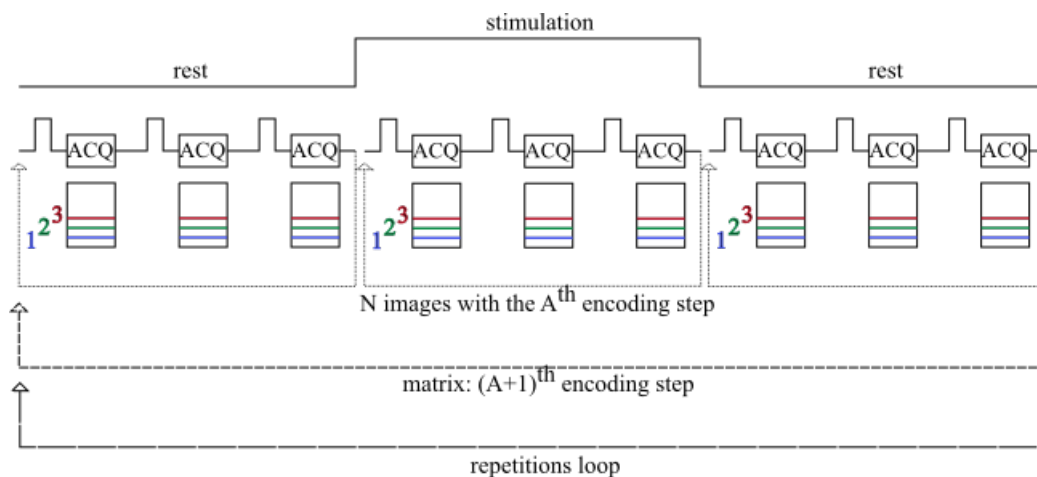


Figure 4.10: Schematic outline of the CINE acquisition used for fMRI at high temporal resolution of TR. Data acquisition is synchronized to the stimulation cycle.

peak response that cannot be sustained over the whole duration of the stimulation. To confirm our first impression of the HRF under this anaesthetic condition, we implemented a cinematographic fMRI experiment. The implementation required a revised programming of the automatic execution of the stimulation directly from the MR pulse program. As the method is sensitive to B_0 fluctuations, the data is often filtered using a low pass in the time domain. Thus, in addition to the MR experiment, we simulated the influence of commonly used filters on the peak shape.

Previously, faster peak response times were reported during single and multiple stimulation regimen under different anaesthetic conditions [101] [102]. Thus, this study was required to confirm the delayed response observed in the previous section. Furthermore, in collaboration with the imaging analysis platform, the HRF was determined in individual pixels, with an improved spatial and temporal resolution of up to $250\mu\text{m}$ and 100 ms.

4.3.1 Method

Cinematographic FLASH

The method presented combines a FLASH sequence with a cine acquisition similar to those developed by Merboldt et al. [21]. Cine FLASH allows a high temporal and a high spatial resolution to detect consistent signal change. The principle of data acquisition is shown in figure 4.10.

The same k-space line of N images is acquired every repetition. The TR defines the temporal resolution of the image separation. Following the acquisition of the

first line of N images, the phase-encoding gradient is incremented. These loops are repeated to cover the full k -space matrix. In theory, the temporal resolution can be in order of a few milliseconds while yielding a resolution usually obtained in high resolution MR scans [21].

However, a TR of 100 ms, a FOV of 32 mm, a data matrix of 128 and 200 images requires an acquisition time of more than one hour. For initial experiments, it might be wise to sacrifice the spatial resolution by decreasing the number of phase-encoding steps. In practice, the temporal resolution should be sufficient to detect the time course of the potential signal changes. However, a necessary increase in temporal resolution should be avoided to prevent system instabilities and handling of enormous data sets. The overall experimental duration thus depends on the number of phase-encoding steps required to ensure the desired spatial resolution and on the duration of the rest period required to ensure a consistent stimulation response.

As the experimental duration to observe a single HRF is very long, system instabilities, movements and B_0 frequencies oscillations might produce artefacts that can not be easily explained.

Animal preparation

Three healthy male Sprague-Dawley rats (360-430g, Janvier Labs, Saint-Berthevin Cedex, France) were used for this experimental protocol. The animals were initially anaesthetized with isoflurane (4-5% for induction and 2% during the set-up) in a mixture of $O_2:N_2$ gases (30:70) delivered to the nose cone for spontaneous respiration throughout the experiment. The head of the anaesthetized animal was carefully secured by Bruker stereotactic fixations in sphinx position. The rectal temperature was kept at $\pm 37^\circ\text{C}$, and the respiration was maintained under 90 breath per minute .

A bolus of 1 mL of medetomidine (Domtor, Esteve) at a concentration of 0.1 mg kg^{-1} was injected subcutaneously. The isoflurane supply was decreased slowly until 0% and a continuous subcutaneous infusion of medetomidine of $0.1 \text{ mg kg}^{-1} \text{ h}^{-1}$ was started to preserve the sedation.

For stimulation-induced fMRI study, electrical stimulation was applied simultaneously to both forepaws using two needle electrodes inserted under the skin and connected to a current stimulation triggered by a pulse generator.

Imaging protocol

All MRI measurements were performed on the 11.7 T magnet described previously with a 40-mm volume coil. Thirty-two consecutive axial slices were acquired with TE of 20 ms, 1 mm slice thickness, a matrix of 128 and a FOV of 32*32 mm² by using a standard RARE sequence. Using the same sequence parameters, sixteen consecutive coronal slices were acquired in order to adjust the slice in the somatosensory cortex. The homogeneity of the magnetic field was optimized within a voxel of 32 mm³ containing the cortical region of interest by a standard PRESS sequence.

Centred on the somatosensory cortex, a FLASH sequence was then acquired with a TR of 100 ms, a FOV of 32 mm and a matrix of 64 or 128, leading to a spatial resolution of 0.5 mm to 0.25 mm. A flip angle of 20° should be close to the Ernst angle for expected T1 values between 1500 ms and 2000 ms. The choice of TE equal to 10 ms was a compromise between diamagnetic and paramagnetic contrast due to haemoglobin within a blood vessel. However, the influence of TE within cine FLASH fMRI was examined. The influence of the cold head during fMRI study was also investigated. The system was switched off during one scan without interfering with the helium pressure.

Each cine FLASH fMRI consisted of 200 images acquisition (rest: 80 without electric stimulation, stimulation: 40 with electric stimulation and rest: 80 without electric stimulation). The sequence is illustrated in figure 4.10. Within each cycle, the same k-space line was accumulated. When the phase encoding n was acquired for the 200 images, the gradient was incremented to the phase encoding $n + 1$. The temporal resolution between images corresponding to the TR namely 100 ms. Stimuli with a fixed pulse width of 300 μ s and a current of 2 mA were applied at a frequency of 9 Hz, based on the previous investigation of the BOLD response [100].

Data processing

Data were processed using Paravision 5.1, MATLAB (R2012B) and Origin. Prior to any further processing, stimulation-induced activation mapped the difference between experimental fMRI data acquired during stimulation versus the control periods on a pixel-by-pixel basis. Activation maps were obtained using the FUN tool of ParaVision 5.1. ROI of 12*12 pixels, or 24*24 pixels for high resolution images. Time courses of these activated pixels were averaged and a FT was then performed on their time courses.

ESTIMATES OF HRF ON STATISTICAL ANALYSES

Prior to any analysis, 1% percent ratio filter has been applied between the baseline and the supposed activated pixels where a peak should appear between image 80 and image 120. The rest of the pixel are set to zero. The HRF was then fitted by a gamma variate function defined by:

$$y(t) = K * (t - t_0)^A * \exp\left(-\frac{t - t_0}{B}\right) \quad (4.2)$$

with $t > t_0$ where t_0 is the starting point of the fitted curve, K is the constant scale factor, A and B are gamma variate parameters characterising the increased and decreased slopes. Non-linear least-squares fitting of the fMRI response using the Levenberg–Marquardt method provided estimates of the model parameters. To measure the goodness of the fit, we defined a coefficient R^2 from the regression analysis. However, as the fitted parameters are almost meaningless, we were interested in some output images as displayed in figure 4.11 [93]. The area under the curve (AUC) defined the quantity of vessels within the brain and corresponded to CBV. The time to onset (M1) characterised the first momentum of the curve of the fitting curve. The time to peak (TTP) defined as the time to reach the peak. From this parameters, we can defined the mean transit time (MTT) as:

$$MTT = \frac{M1}{AUC} \quad (4.3)$$

The parameter *cbf* modelling the cerebral blood flow can be defined as:

$$cbf = \frac{AUC}{MTT} = \frac{AUC^2}{M1} \quad (4.4)$$

INFLUENCE OF BAND-PASS FILTERS

We then estimated the influence of low-pass and band-pass filters on the fitting of the HRF by the gamma variate. As a general shape of the response, a Gauss, a Block and a Gamma functions were assumed. Three sets of 200 continuous points function estimated the HRF with a specific shape. Low-pass and band-pass filters were then applied to these simulated HRF. Simulations were used to examine the effect of variations in the HRF curves on fitting procedure. A similar fitting with the gamma variate function was then been done.

4.3.2 Results and Discussion

A high resolution FLASH image obtained in a cinematographic mode (figure 4.12 B) shows an improvement in resolution when compared to the single-shot acquisi-

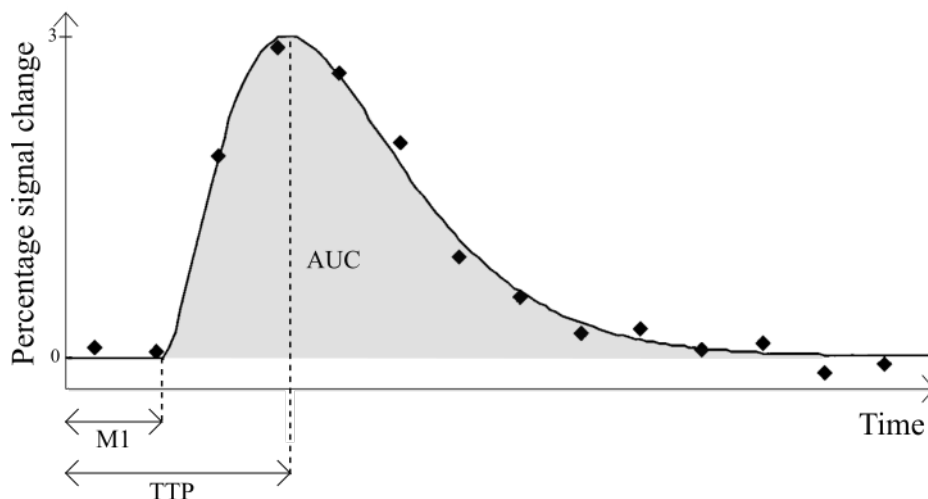


Figure 4.11: Three estimated parameters: time to onset (M1), mean transit time (MTT) and area under the curve (AUC) based on the least mean square of gamma fitting of the hemodynamic response function (HRF) (figure adapted from [93]).

tion described in section 4.2 (figure 4.12 A). Under a medetomidine anaesthesia, the rats exhibited normal activation in the somatosensory cortex during stimulation of the forepaws. The difference map was obtained by subtracting the average mean from baseline images (image 5 to image 80, and image 140 to image 200), and the corresponding average mean from activated images (image 90 to image 120). The time course of the 'activated' pixels is illustrated in figure 4.13.

Unfortunately, as can be seen in figure 4.13, large artificial periodic noise contaminated the time course. This periodic oscillation was previously attributed to physiological noise, mainly respiratory motion [21]. To confirm the source of the artefact, the time series were transform by FT and the frequency distribution shows four peaks. Respiratory and cold head frequency are identifiable at 1.1-1.2 Hz, and 1.41 Hz respectively (figure 4.14). To identify the cause of the system imperfection, the cold head was switched off in one experiment. Indeed, as can be seen in figure 4.14, the most intense peak disappears. Therefore, the B_0 oscillation caused by the cold head vibrations are in the same order of magnitude as the physiological noise in our system at 11.7T using this MRI protocol.

Independently, the average time course of the activated pixel within the somatosensory cortex indicates an underlined peak at around image 113 (table 4.1). As fMRI data are extremely noisy data, it is important to minimize noise in order to interpolate the amplitude and timing of the HRF. Model of hemodynamic functions (Block, Gauss and Gamma) have been assumed (figure 4.15). Usually, a band-pass filter is used to remove these periodical artefacts found in fMRI data without removing the signal of interest. Filtering fMRI data with a temporal pass

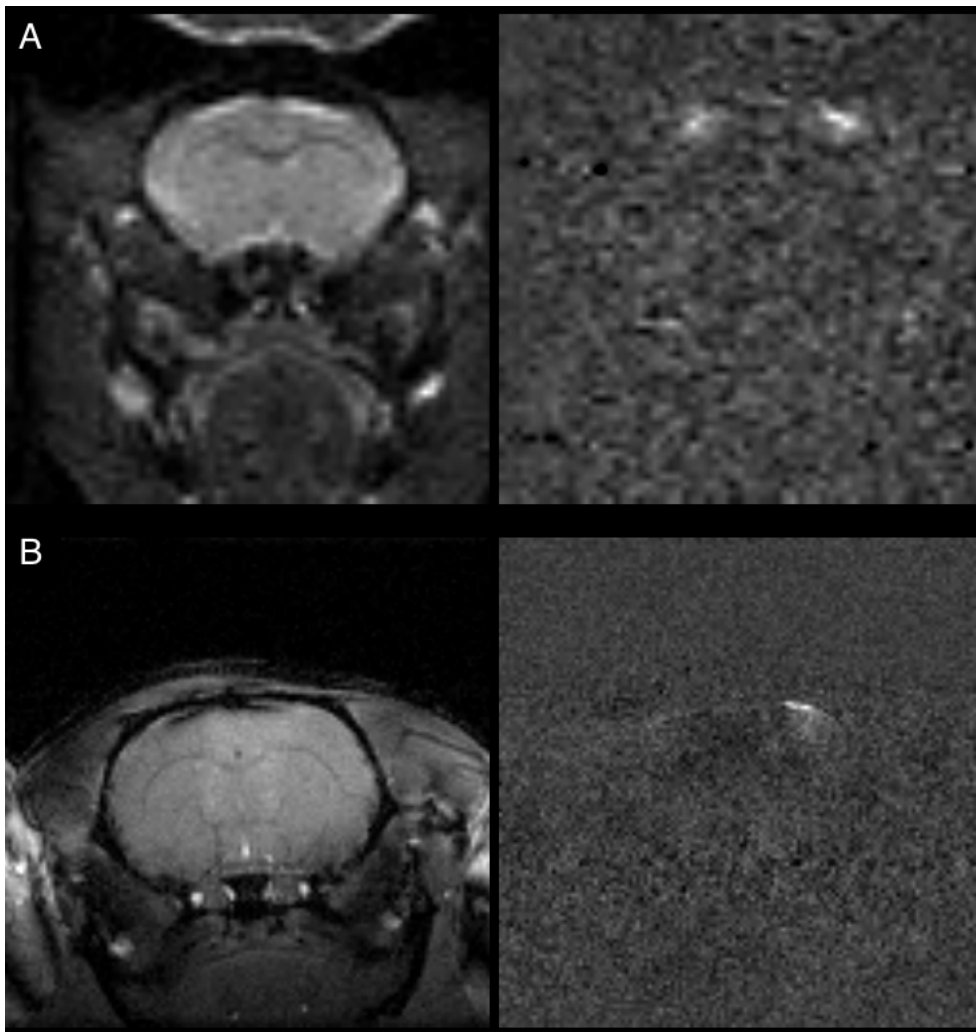


Figure 4.12: Comparison between an original SE-EPI image (A) and its corresponding activation map obtained using the FUN tool of ParaVision 5.1; and a cine FLASH (B) acquired with a spatial resolution of $250 \mu\text{m}$ and a temporal resolution of 100 ms between events. Some pixels are clearly 'activated'.

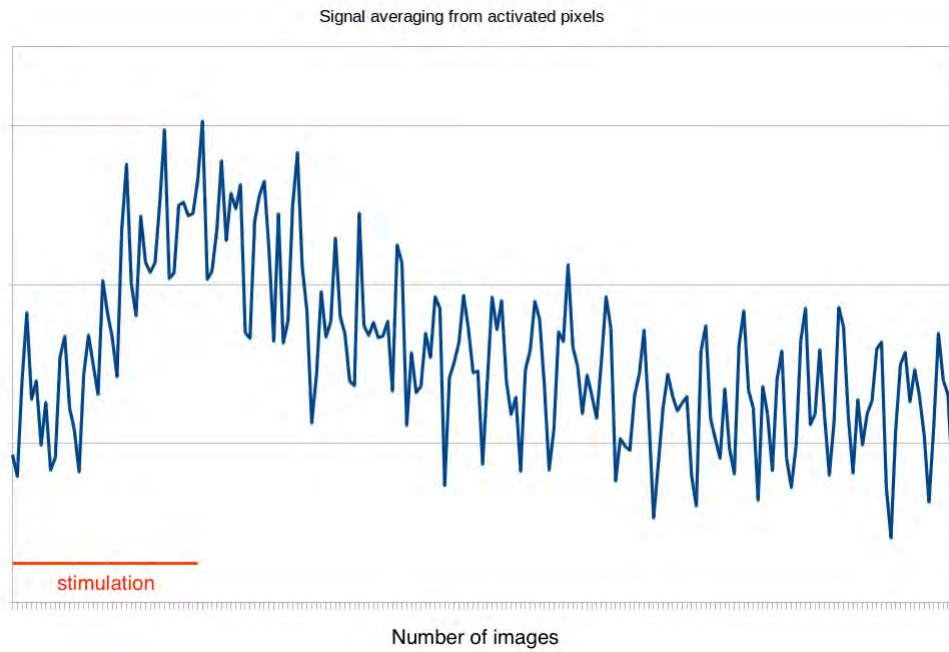


Figure 4.13: Typical time course of the 'activated' pixels obtained with the implemented cine FLASH sequence.

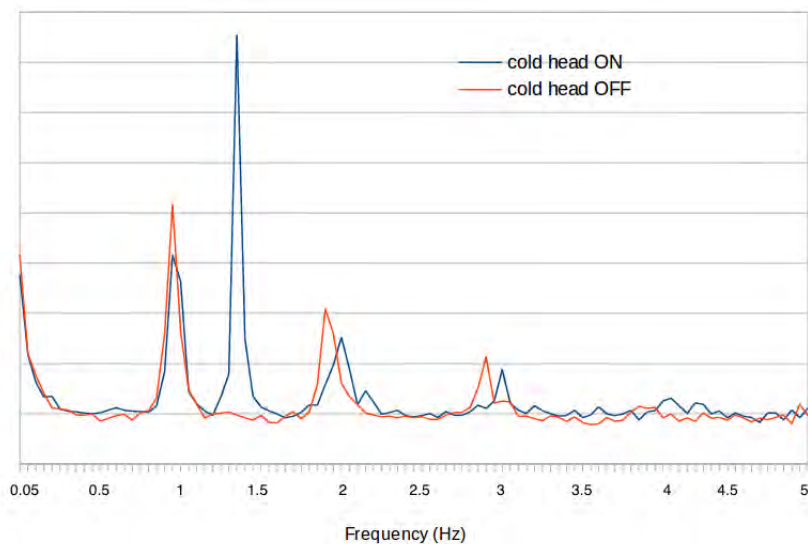


Figure 4.14: Frequency distribution after Fast Fourier Transform of cine FLASH time series acquired at high resolution. A new phase error appears: the cold head frequency (data acquired switching on and off the cold head).

filter is a good idea since high temporal frequencies are not stimulus-dependent noise. Low-pass filters are used to remove artefacts induced by respiration of the animals. Cardiac waveforms could be filtered with a band-pass filter. To familiarise ourselves to a potentials constraints of the fitting, we performed simulation on different peak functions and filters. As can be seen in figure 4.15, gamma variate fit is suitable to determine a correct HRF of functions like Gauss or Gamma variate peak. Fitting a Block response does not reflect the HRF shape. Thus, as the fitting will naturally reduce the errors by obtaining a asymmetric function, it is required to confirm the absence of a block response by filtering the time course data. For this, we simulated four different Gauss function, four different Block function and four different Gamma functions and subjected to low pass and band pass filters derived from the frequency distribution of our experiment (figure 4.14). The pulse shape is only marginally altered up to the removal of frequencies above 0.06 Hz.

To be able to identify the peak shape and for quantification, we decided to determine the HRF by a gamma variate fitting. The high resolution image was fitted on a pixel-by-pixel basis. Within the somatosensory cortex, we were able to identify forty-two pixels which showed a robust variation from baseline applying the following thresholds as the peak intensity should be above 1.5% above baseline and the peak high between images 80 and 160. Figure 4.16 shows the results of all 42 HRF derived at the resolution of $250 \mu\text{m}$. As can be seen, the magnitude, the start of the peak and the peak width differs. To highlight the differences, the figure 4.16 shows the coloured maps overlaid the original black and white image displaying the following parameters: t_0 , M1, TTP, AUC, cbf and MTT. The average values and the standard deviation of the 42 pixels of the derived parameters are listed in table 4.1. Importantly, the observed main signal changes occur only on few pixels with signal change of around 50%, indicating in-flow contribution from large vessels. The spatial distribution of the large signal changes is mainly confirmed to the layer on the cortex. We were not able to identify a consistent layer-specific response as reported in the literature [102][103].

Importantly, no direct biological conclusion of the signal behaviour should be made as the HR scan has been obtained in only one animal and thus this study has a pilot character. Nevertheless, we can confirm the results obtained in chapter 4.2 that the stimulation protocol under medetomine anaesthesia leads to a peak onset of 101 ms (table 4.1). This is substantially longer than the BOLD signal changes in the somatosensory cortex of the rat 600 ms after stimulation [101] and 800 ms following stimulation in α -chloralose anaesthetised rats [103].

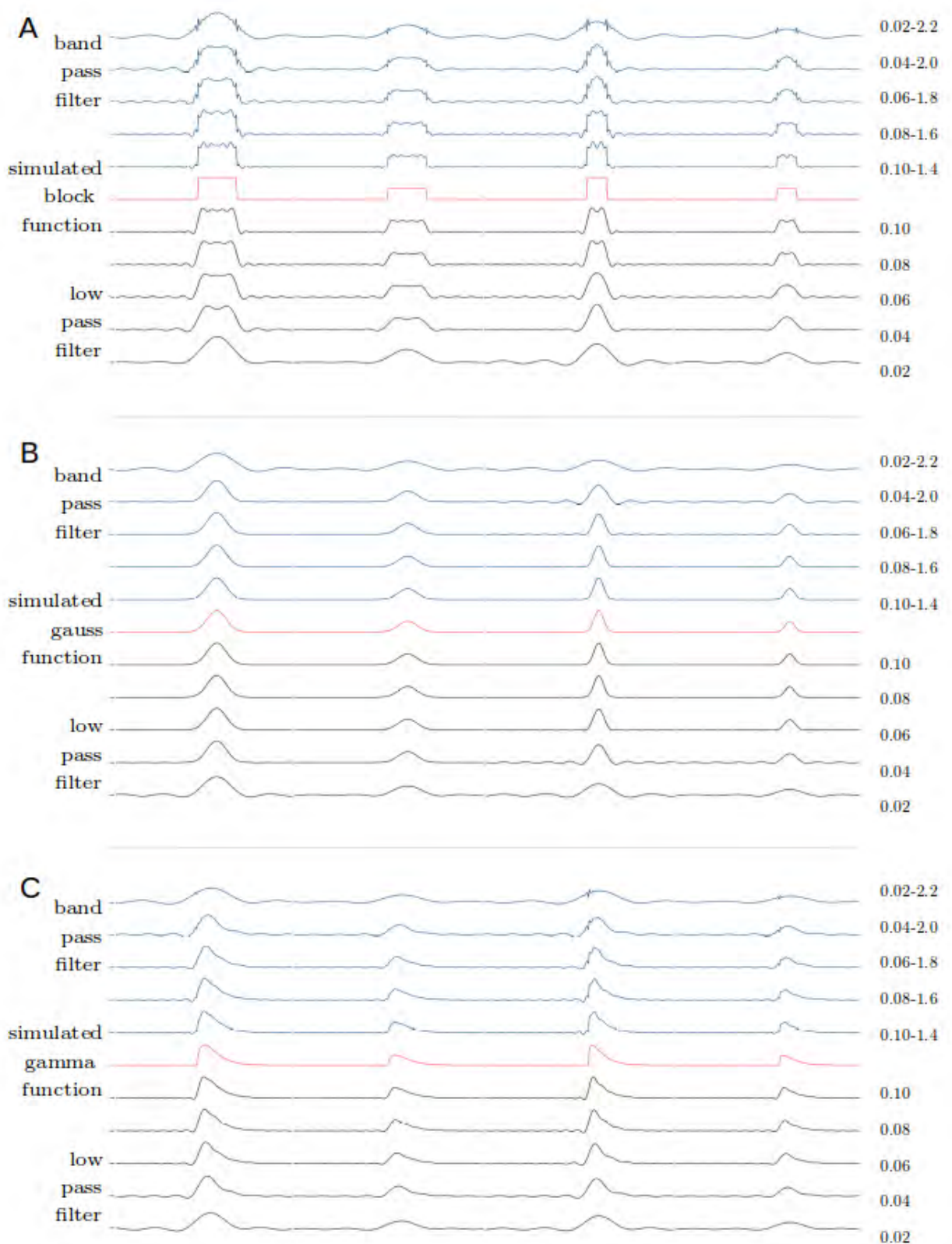


Figure 4.15: Simulated Block (A), Gauss (B) and Gamma (C) functions through the application of band-pass and low-pass filters.

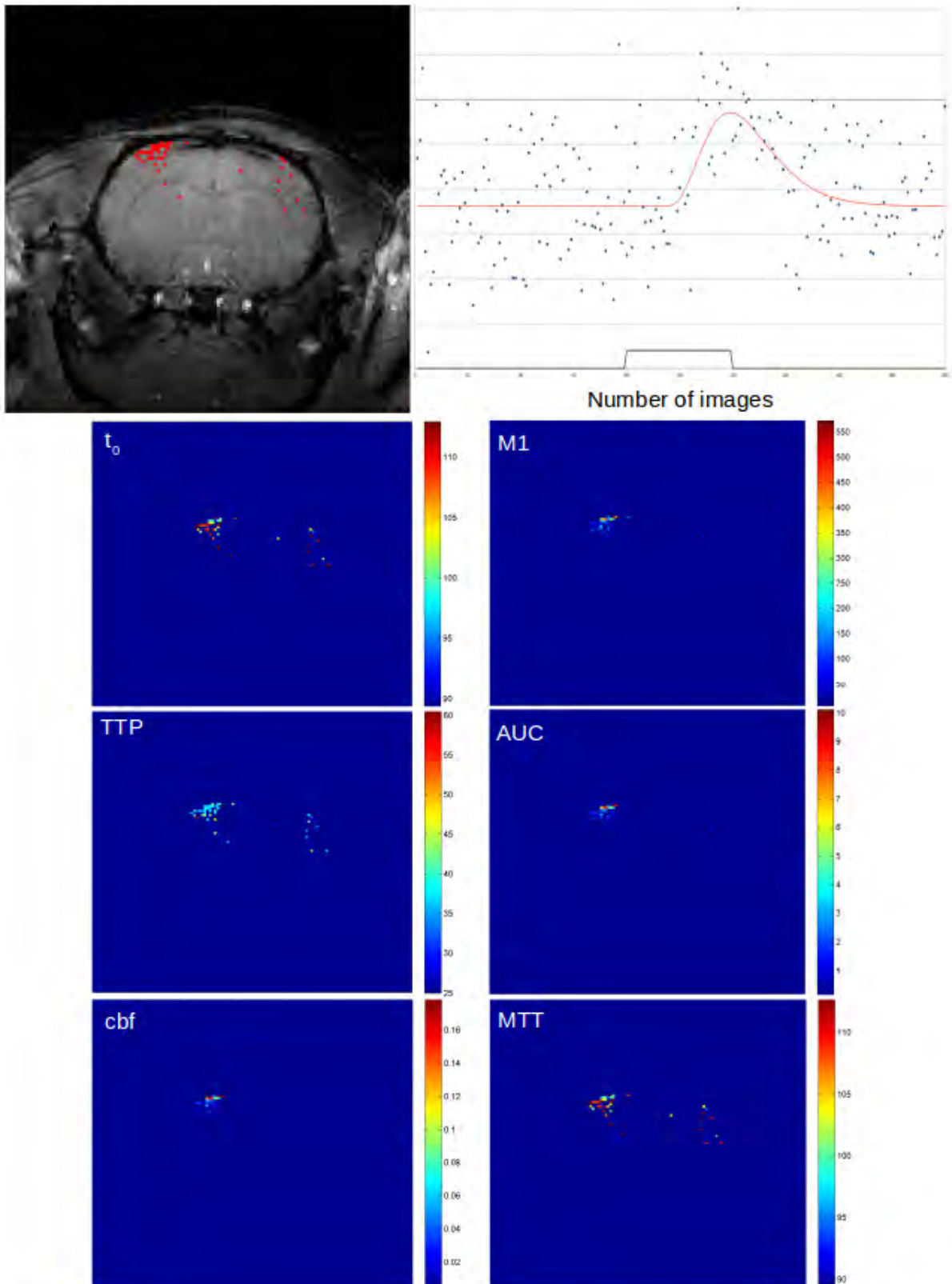


Figure 4.16: 42 pixels 'activated' identified by the cine FLASH sequence at 11.7T. The image top left displays a resolution of $250 \mu\text{m}$ overlaid by the pixels. On the top right, the data from one pixel is displayed showing a delay between the start of the simulation and the peak function. The profile is not sustained over the stimulus duration. To highlight the differences, the following parameters t_0 , M1, TTP, AUC, cbf and MTT are mapped on a pixel-by-pixel basis. *Note:* t_0 is the starting point of the fitted curve; M1 is the time to onset; TTP is defined as the time to peak; AUC is the area under the fitted HRF by the gamma variate; cbf is a parameter modelling the cerebral blood flow; the MTT is defined as mean transit time.

	t0	M1	TTP	AUC	cbf	MTT
	starting	time to	time to	area under	estimation of	mean transit
	point	onset	peak	the curve	CBF	time
mean	101.1	125.7	113.8	2.32	0.04	50.1
StD	20.8	124.0	23.2	2.32	0.04	13.2

Table 4.1: Fitting parameters of the 42 pixels averaged from the high resolution scan obtained with the cine FLASH method.

4.4 Conclusion

To sum up, we successfully studied the BOLD response changes under the influence of acute hyperglycemia by the two main anomers of D-glucose. However, the HRF observed at the baseline and following the administration of glucose yielded a late onset peak response when compared to previous reported values for the anaesthetized rat. To explore this aspect on the neurovascular coupling, we performed a high resolution fMRI study using the cine FLASH with an improved spatial and temporal resolution. The cine FLASH method is highlighting phase errors caused by movements or B_0 fluctuations and the time series data has to be post-processed.

Bibliography

- [1] R.A. de Graaf. *In Vivo NMR Spectroscopy, 2nd Edition: Principles and Techniques*. 2007.
- [2] P. Mansfield. Multi-planar image formation using NMR spin echoes. *Journal of Physics C: Solid State Physics*, 10(3):L55–L58, 1977.
- [3] J. Hennig, A. Nauerth, and H. Friedburg. RARE imaging: a fast imaging method for clinical MR. *Magnetic Resonance in Medicine*, 3(6):823–833, 1986.
- [4] M.A. Bernstein, K.F. King, and X.J. Zhou. *Handbook of MRI Pulse Sequences*. 2004.
- [5] R.W. Brown, Y.-C. N.Cheng, E.M. Haacke, M.R. Thompson, and R. Venkatesan. *Magnetic Resonance Imaging: Physical Principles and Sequence Design*. 2014.
- [6] M. Filippi, editor. *fMRI Techniques and Protocols*. 2016.
- [7] E. L. Hahn. Spin Echoes. *Physical review*, 80(4):580–594, 1950.
- [8] B. Shah, S.W. Anderson, J. Scalera, H. Jara, and J.A. Soto. Quantitative MR imaging: physical principles and sequence design in abdominal imaging. *RadioGraphics*, 31(3):867–880, 2011.
- [9] I.L. Pykett and R.R. Rzedzian. Instant images of the body by magnetic resonance. *Magnetic Resonance in Medicine*, 5(6):563–571, 1987.
- [10] R.A. de Graaf, P.B. Brown, S. McIntyre, T.W. Nixon, K.L. Behar, and D.L. Rothman. High magnetic field water and metabolite proton T1 and T2 relaxation in rat brain in vivo. *Magnetic resonance in medicine : official journal of the Society of Magnetic Resonance in Medicine / Society of Magnetic Resonance in Medicine*, 56(2):386–394, 2006.
- [11] A. Haase, J. Frahm, D. Matthaei, W. Hanicke, and K. D. Merboldt. FLASH imaging. Rapid NMR imaging using low flip-angle pulses. *Journal of Magnetic Resonance*, 67(2):258–266, 1986.
- [12] R.E. Burgess, Y. Yu, A.M. Abduljalil, A. Kangarlu, and P.M.L. Robitaille. High signal-to-noise flash imaging at 8 Tesla. *Magnetic Resonance Imaging*, 17(8):1099–1103, 1999.
- [13] A. Haase. Snapshot FLASH MRI. Applications to T1, T2 and Chemical Shift Imaging. *Magnetic Resonance in Medicine*, 13:77–89, 1990.
- [14] S. Nekolla, T. Gneiting, J. Syha, R. Deichmann, and A. Haase. T1 Maps by K-Space Reduced Snapshot-FLASH MRI. *Journal of Computer Assisted Tomography*, 16(2):327–332, 1992.
- [15] S. Hamrouni-Chtourou. *Approches variationnelles statistiques spatio-temporelles pour l'analyse quantitative de la perfusion myocardique en IRM*. PhD thesis, 2012.
- [16] T. Nagele, D. Petersen, U. Klose, W. Grodd, H. Opitz, E. Gut, J. Martos, and K. Voigt. Dynamic contrast enhancement of intracranial tumors with snapshot-FLASH MR imaging. *AJNR. American journal of neuroradiology*, 14(1):89–98, 1993.
- [17] A.L. Lopez Kolkovsky. *1H and 31P NMR Spectroscopy for the study of brain metabolism at Ultra High Magnetic Field from Rodents to Men. Université Paris Sud - Paris XI (NNT: 2015PA112080, tel-01194657)*. PhD thesis, 2015.
- [18] R. Deichmann, H. Adolf, U. Nöth, S. Morrissey, C. Schwarzbauer, and A. Haase. Fast T2-mapping with snapshot FLASH imaging. *Magnetic Resonance Imaging*, 13(4):633–639, 1995.
- [19] R. Deichmann and A. Haase. Quantification of T1 values by snapshot FLASH NMR imaging. *Journal of Magnetic Resonance*, 612:608–612, 1992.

- [20] A.J. Bakermans, D. Abdurrachim, R.P.M. Moonen, A.G. Motaal, J.J. Prompers, G.J. Strijkers, K. Vandoorne, and K. Nicolay. Small animal cardiovascular MR imaging and spectroscopy. *Progress in Nuclear Magnetic Resonance Spectroscopy*, 88-89:1-47, 2015.
- [21] K.D. Merboldt, G. Kruger, W. Hanicke, A. Kleinschmidt, and J. Frahm. Functional MRI of human brain activation combining high spatial and temporal resolution by a CINE FLASH technique. *Magnetic Resonance in Medicine*, 34(6):639-644, 1995.
- [22] C.B. Ahn, J.H. Kim, and Z.H. Cho. High-Speed Spiral-Scan Echo Planar NMR Imaging - 1. *IEEE Transactions on Medical Imaging*, 5(1):2-7, 1986.
- [23] D.C. Look and D.R. Locker. Time Saving in Measurement of NMR and EPR Relaxation Times. *Review of Scientific Instruments*, 41(2):250-251, 1970.
- [24] J. Hennig. Multiecho Imaging Sequences with Low Refocusing Flip Angles. *Journal of Magnetic Resonance*, 78:397-407, 1988.
- [25] D.G. Norris, P. Börnert, T. Reese, and D. Leibfritz. On the application of ultra-fast RARE experiments. *Magnetic Resonance in Medicine*, 27(1):142-164, 1992.
- [26] R.V. Mulkern, S.T.S. Wong, P. Jakab, A.R. Bleier, T. Sandor, and F.A. Jolesz. CPMG imaging sequences for high field in vivo transverse relaxation studies. *Magnetic Resonance in Medicine*, 16(1):67-79, 1990.
- [27] D.G. Norris. Ultrafast Low-Angle RARE: U-FLARE. *Magnetic Resonance in Medicine*, 17:539-542, 1991.
- [28] D.G. Norris and P. Börnert. Coherence and Interference in Ultrafast RARE Experiments. *Journal of Magnetic Resonance*, 105:123-127, 1993.
- [29] P. Börnert, D.G. Norris, H. Koch, W. Dreher, H. Reichelt, and D. Leibfritz. Fast perfluorocarbon imaging using 19-F U-FLARE. *Magnetic Resonance in Medicine*, 29:226-234, 1993.
- [30] W. Dreher and D. Leibfritz. Improved proton spectroscopic U-FLARE imaging for the detection of coupled resonances in the rat brain in vivo. *Magnetic Resonance Imaging*, 17(4):611-621, 1999.
- [31] I. Markuerkiaga, S. Plaza-García, D. Padro, and T. Reese. Assessment of a gradient thermostat unit: Implications to field alterations at a 11.7 Tesla preclinical system. *International Journal of Scientific & Engineering Research*, 6(11):649-656, 2015.
- [32] N. Weiskopf, J. Suckling, G. Williams, M.M. Correia, B. Inkster, R. Tait, C. Ooi, E.T. Bullmore, and A. Lutti. Quantitative multi-parameter mapping of R1, PD*, MT, and R2* at 3T: A multi-center validation. *Frontiers in Neuroscience*, 7:1-11, 2013.
- [33] M.H. de Miguel, H.N. Yeung, M. Goyal, J.W. Noh, A.M. Aisen, S.H. Phan, and R.C. Wiggins. Evaluation of Quantitative Magnetic Resonance Imaging as a Noninvasive Technique for Measuring Renal Scarring in a Rabbit Model of Antiglomerular Basement Membrane Disease. *Journal of the American Society of Nephrology*, 4:1861-1868, 1994.
- [34] A.P. Crawley and R.M. Henkelman. A comparison of one-shot and recovery methods in T1 imaging. *Magnetic Resonance in Medicine*, 7(1):23-34, 1988.
- [35] J.K. Barral, E. Gudmundson, N. Stikov, M. Etezadi-Amoli, P. Stolca, and D.G. Nishimura. A Robust Methodology for In Vivo T1 Mapping. *Magnetic Resonance in Medicine*, 64(4):1057-1067, 2010.
- [36] A. Hellerbach, V. Schuster, A. Jansen, and J. Sommer. MRI Phantoms - Are There Alternatives to Agar? *PLoS ONE*, 8(8), 2013.
- [37] P.A. Bottomley, T.H. Foster, R.E. Argersinger, and L.M. Pfeifer. A review of normal tissue hydrogen NMR relaxation times and relaxation mechanisms from 1-100 MHz: dependence on tissue type, NMR frequency, temperature, species, excision, and age. *Medical physics*, 11(4):425-48, 1984.
- [38] R. Rajendran, S.K. Lew, C.X. Yong, J. Tan, D.J.J. Wang, and K.H. Chuang. Quantitative mouse renal perfusion using arterial spin labeling. *NMR in Biomedicine*, 26(10):1225-1232, 2013.

- [39] M. Bilgen, B. Al-Hafez, N.E.J. Berman, and B.W. Festoff. Magnetic resonance imaging of mouse spinal cord. *Magnetic Resonance in Medicine*, 54:1226–1231, 2005.
- [40] V. Callot, G. Duhamel, and P.J. Cozzone. In vivo mouse spinal cord imaging using echo-planar imaging at 11.75 T. *Magnetic Resonance Materials in Physics*, 20:169–173, 2007.
- [41] R.F. Busse, H. Hariharan, A. Vu, and J.H. Brittain. Fast spin echo sequences with very long echo trains: Design of variable refocusing flip angle schedules and generation of clinical T2 contrast. *Magnetic Resonance in Medicine*, 55:1030–1037, 2006.
- [42] C.J. Hardy and H.E. Cline. Spatial localization in two dimensions using NMR designer pulses. *Journal of Magnetic Resonance*, 82:647–654, 1989.
- [43] W. Dreher, E. Busch, K. Bockhorst, M. Meier, and D. Leibfritz. Single-shot Multislice U-FLARE Imaging. Application to Functional MRI. *Proc. Intl. Soc. Mag. Reson. Med.*, page 1220, 2001.
- [44] D.G. Norris, P.J. Koopmans, R. Boyacioglu, and M. Barth. Power Independent of Number of Slices (PINS) radiofrequency pulses for low-power simultaneous multislice excitation. *Magnetic Resonance in Medicine*, 66:1234–1240, 2011.
- [45] D.G. Norris, R. Boyacioglu, J. Schulz, M. Barth, and P.J. Koopmans. Application of PINS radiofrequency pulses to reduce power deposition in RARE/turbo spin echo imaging of the human head. *Magnetic Resonance in Medicine*, 71:44–49, 2014.
- [46] S.C.L. Deoni. Quantitative Relaxometry of the Brain. *Topics in Magnetic Resonance Imaging*, 21(2):101–113, 2010.
- [47] Y. Ding, R.P. Mason, R.W. McColl, Q. Yuan, R.R. Hallac, R.D. Sims, and P.T. Weatherall. Simultaneous measurement of tissue oxygen level-dependent (TOLD) and blood oxygenation level-dependent (BOLD) effects in abdominal tissue oxygenation level studies. *Journal of Magnetic Resonance Imaging*, 38:1230–1236, 2013.
- [48] W. Shin, H. Gu, and Y. Yang. Fast high-resolution T1 mapping using inversion-recovery look-locker echo-planar imaging at steady state: Optimization for accuracy and reliability. *Magnetic Resonance in Medicine*, 61(4):899–906, 2009.
- [49] J. Wang, W. Mao, M. Qiu, M.B. Smith, and R.T. Constable. Factors influencing flip angle mapping in MRI: RF pulse shape, slice-select gradients, off-resonance excitation, and B0 inhomogeneities. *Magnetic Resonance in Medicine*, 56(2):463–468, 2006.
- [50] M. Han, K. Chiba, S. Banerjee, J. Carballido-Gamio, and R. Krug. Variable Flip Angle 3D Fast Spin-Echo Sequence Combined with Outer Volume Suppression for Imaging Trabecular Bone Structure of the Proximal Femur. *Journal of Magnetic Resonance Imaging*, 41(5):1300–1310, 2016.
- [51] H.Y. Carr. Steady-State Free Precession in Nuclear Magnetic Resonance. *Physical review*, 112(5):1693–1701, 1958.
- [52] D. Ma, V. Gulani, N. Seiberlich, K. Liu, J.L. Sunshine, J.L. Duerk, and M.A. Griswold. Magnetic resonance fingerprinting. *Nature*, 495(7440):187–192, 2013.
- [53] Y. Gao, Y. Chen, D. Ma, Y. Jiang, K.A. Herrmann, J.A. Vincent, K.M. Dell, M.L. Drumm, S.M. Brady-Kalnay, M.A. Griswold, C.A. Flask, and L. Lu. Preclinical MR fingerprinting (MRF) at 7 T: Effective quantitative imaging for rodent disease models. *NMR in Biomedicine*, 28:384–394, 2015.
- [54] R.L. Sacco, S.E. Kasner, J.P. Broderick, L.R. Caplan, J.J. Connors, A. Culebras, M.S.V. Elkind, M.G. George, A.D. Hamdan, R.T. Higashida, B.L. Hoh, L.S. Janis, C.S. Kase, D.O. Kleindorfer, J.M. Lee, M.E. Moseley, E.D. Peterson, T.N. Turan, A.L. Valderrama, and H.V. Vinters. An updated definition of stroke for the 21st century: A statement for healthcare professionals from the American heart association/American stroke association. *Stroke*, 44(7):2064–2089, 2013.
- [55] Z. Starosolski, C.A. Villamizar, D. Rendon, M.J. Paldino, D.M. Milewicz, K.B. Ghaghada, and Ananth V. Annappagada. Ultra High-Resolution In vivo Computed Tomography Imaging of Mouse Cerebrovasculature Using a Long Circulating Blood Pool Contrast Agent. *Scientific Reports*, 5(1):10178, 2015.

- [56] T. Reese, D. Bochelen, A. Sauter, N. Beckmann, and M. Rudin. Magnetic resonance angiography of the rat cerebrovascular system without the use of contrast agents. *NMR in biomedicine*, 12:189–196, 1999.
- [57] M.A. Bernstein, X.J. Zhou, J.A. Polzin, K.F. King, A. Ganin, N.J. Pelc, and G.H. Glover. Concomitant Gradient Terms in Phase Contrast MR: Analysis and Correction. *Magnetic Resonance in Medicine*, 39:300–308, 1998.
- [58] G. Figueiredo, C. Brockmann, H. Boll, M. Heilmann, S.J. Schambach, T. Fiebig, M. Kramer, C. Groden, and M.A. Brockmann. Comparison of digital subtraction angiography, micro-computed tomography angiography and magnetic resonance angiography in the assessment of the cerebrovascular system in live mice. *Clinical Neuroradiology*, 22(1):21–28, 2012.
- [59] L. Belayev, O.F. Alonso, R. Busto, W. Zhao, and M.D. Ginsberg. Middle Cerebral Artery Occlusion in the Middle Cerebral Artery Occlusion in the Rat by Intraluminal Suture. *Stroke*, (27):1616–1623, 1996.
- [60] S. Liu, G. Zhen, B.P. Meloni, K. Campbell, and H.R. Winn. Rodent Stroke Model Guidelines for Preclinical Stroke Trials (1st Edition). *Journal of experimental stroke & translational medicine*, 2(2):2–27, 2009.
- [61] M. Fisher, G. Feuerstein, D.W. Howells, P.D. Hurn, T.A. Kent, S.I. Savitz, and Eng H. Lo. Update of the stroke therapy academic industry roundtable preclinical recommendations. *Stroke*, 40(6):2244–2250, 2009.
- [62] H.L.M Cheng, N. Stikov, N.R. Ghugre, and G.A. Wright. Practical medical applications of quantitative MR relaxometry. *Journal of Magnetic Resonance Imaging*, 36(4):805–824, 2012.
- [63] G. Pastor, M. Jiménez-González, S. Plaza-García, M. Beraza, D. Padro, P. Ramos-Cabrera, and T. Reese. A general protocol of ultra-high resolution MR angiography to image the cerebro-vasculature in 6 different rats strains at high field. *Journal of Neuroscience Methods*, 2017.
- [64] Z. He, T. Yamawaki, S. Yang, A. L. Day, J. W. Simpkins, H. Naritomi, and W. I. Rosenblum. Experimental model of small deep infarcts involving the hypothalamus in rats : changes in body temperature and postural reflex. *Stroke*, 30(12):2743–2751, 1999.
- [65] E. Rostrup, P.B. Toft, and K. Gardet. Human Brain Induced by Hypo- and Hyperoxia. *NMR in Biomedicine*, 8:41–47, 1995.
- [66] N.A. Watson, S.C. Beards, N. Altaf, A. Kassner, and A. Jackson. The effect of hyperoxia on cerebral blood flow: A study in healthy volunteers using magnetic resonance phase-contrast angiography. *European Journal of Anaesthesiology*, 17(3):152–159, 2000.
- [67] H. Uematsu, M. Takahashi, H. Hatabu, C.-L. Chin, S.L. Wehrli, F.W. Wehrli, and Toshio Asakura. Changes in T1 and T2 observed in brain magnetic resonance imaging with delivery of high concentrations of oxygen. *Journal of computer assisted tomography*, 31(5):662–5, 2007.
- [68] T. Gerriets, E. Stolz, M. Walberer, C. Müller, C. Rottger, A. Kluge, Manfred Kaps, Marc Fisher, and Georg Bachmann. Complications and pitfalls in rat stroke models for middle cerebral artery occlusion: A comparison between the suture and the macrosphere model using magnetic resonance angiography. *Stroke*, 35(10):2372–2377, 2004.
- [69] F. Chauveau, T.-H. Cho, M. Perez, M. Guichardant, A. Riou, P. Aguetaz, M. Picq, M. Lagarde, Y. Berthezène, N. Nighoghossian, and M. Wiart. Brain-targeting form of docosahexaenoic acid for experimental stroke treatment: MRI evaluation and anti-oxidant impact. *Current neurovascular research*, 8(2):95–102, 2011.
- [70] H. Makino, K. Hokamura, T. Natsume, T. Kimura, Y. Kamio, Y. Magata, H. Namba, T. Katoh, S. Sato, T. Hashimoto, and K. Umemura. Successful serial imaging of the mouse cerebral arteries using conventional 3-T magnetic resonance imaging. *Journal of cerebral blood flow and metabolism : official journal of the International Society of Cerebral Blood Flow and Metabolism*, 35(9):1523–1527, 2015.
- [71] Y. Wang-Fischer, R. Prado, and L. Koetzner. *Manual of Stroke Models in rats (chapter 4)*. CRC Press, 2008.

- [72] D. Attwell, A. Buchan, S. Charpak, M. Lauritzen, B. MacVicar, and E. Newman. Glian and neuronal control of brain blood flow. *Nature*, 468(7321):232–243, 2011.
- [73] S. A. Bunge and I. Kahn. Cognition: An Overview of Neuroimaging Techniques. *Encyclopedia of Neuroscience*, pages 1063–1067, 2010.
- [74] P. Mergenthaler, U. Lindauer, G.A. Dienel, and A. Meisel. Sugar for the brain : the role of glucose in physiological and pathological brain function. *Trends in Neurosciences*, 36(10):587–597, 2013.
- [75] M.P. van den Heuvel and H.E. Hulshoff Pol. Exploring the brain network : A review on resting-state fMRI functional connectivity. *European Neuropsychopharmacology*, 20(8):519–534, 2010.
- [76] H. Johansen-Berg and M.F.S. Rushworth. Using diffusion imaging to study human connective anatomy. *Annual review of neuroscience*, 32:75–94, 2009.
- [77] M.E. Raichle and M.A. Mintun. Brain Work and Brain Imaging. *Annual Review of Neuroscience*, 29(1):449–476, 2006.
- [78] C.F. Ferris, M. Febo, F. Luo, K. Schmidt, M. Brevard, J.A. Harder, P. Kulkarni, T. Messenger, and J.A. King. Functional magnetic resonance imaging in conscious animals: A new tool in behavioural neuroscience research. *Journal of Neuroendocrinology*, 18(5):307–318, 2006.
- [79] J.V. Liu, Y. Hirano, G.C. Nascimento, B. Stefanovic, D.A. Leopold, and A.C. Silva. fMRI in the awake marmoset: Somatosensory-evoked responses, functional connectivity, and comparison with propofol anesthesia. *NeuroImage*, 78:186–195, 2013.
- [80] J.X. Haensel, A. Spain, and C. Martin. A systematic review of physiological methods in rodent pharmacological MRI studies. *Psychopharmacology*, 232(3):489–499, 2015.
- [81] T. Wu, J. Grandjean, S.C. Bosshard, M. Rudin, D. Reutens, and T. Jiang. Altered regional connectivity reflecting effects of different anaesthesia protocols in the mouse brain. *NeuroImage*, 149(February):190–199, 2017.
- [82] T. Kim, K. Masamoto, M. Fukuda, A. Vasquez, and S.-G. Kim. Frequency-dependent neural activity, CBF and BOLD fMRI to somatosensory stimuli in isoflurane-anesthetized rats. *NeuroImage*, 52:224–233, 2010.
- [83] K.A. Williams, M. Magnuson, W. Majeed, S.M. LaConte, S.J. Peltier, X. Hu, and S.D. Keilholz. Comparison of alpha-chloralose, medetomidine and isoflurane anesthesia for functional connectivity mapping in the rat. *Magnetic Resonance Imaging*, 28(7):995–1003, 2010.
- [84] K. Hara and R.A. Harris. The anesthetic mechanism of urethane: the effects on neurotransmitter-gated ion channels. *Anesthesia and analgesia*, 94(2), 2002.
- [85] I.-Y. Choi, H. Lei, and R. Gruetter. Effect of Deep Pentobarbital Anesthesia on Neurotransmitter Metabolism in vivo: On the Correlation of Total Glucose Consumption with Glutamatergic Action. *Journal of Cerebral Blood Flow & Metabolism*, 22(11):1343–1351, 2002.
- [86] X. Liu, S. Pillay, R. Li, J.A. Vizueté, K.R. Pechman, K.M. Schmainda, and A.G. Hudetz. Multiphasic modification of intrinsic functional connectivity of the rat brain during increasing levels of propofol. *NeuroImage*, 83:581–592, 2013.
- [87] R. Weber, P. Ramos-Cabrera, D. Wiedermann, N. van Camp, and M. Hoehn. A fully noninvasive and robust experimental protocol for longitudinal fMRI studies in the rat. *NeuroImage*, 29:1303–1310, 2006.
- [88] E.D. Brăslășu, C. Brădălan, M. Cornilă, I. Săvulescu, R. Cojmaletă, and M.C. Brăslășu. Normal Blood Glucose in White Wistar Rat and Its Changes Following Anesthesia. *Lucrări Științifice Medicină Veterinară*, XL(7):120–123, 2007.
- [89] P.A. Bandettini. *Temporal Resolution and Spatial Resolution of fMRI*, volume 1. Published by Elsevier Inc., 2015.
- [90] S. Ogawa, T.M. Lee, A.R. Kay, and D.W. Tank. Brain magnetic resonance imaging with contrast dependent on blood oxygenation. *Proc. Natl. Acad. Sci USA*, 87:9868–9872, 1990.

- [91] S.-G. Kim and S. Ogawa. Biophysical and physiological origins of blood oxygenation level-dependent fMRI signals. *Journal of cerebral blood flow and metabolism*, 32(7):1188–1206, 2012.
- [92] C.W. Tyler and L.T. Likova. The Neuro-Metabolic Underpinnings of fMRI BOLD Dynamics. In *Advanced Brain Neuroimaging Topics in Health and Disease - Methods and Applications*. 2014.
- [93] F.M. Miezin, L. Maccotta, J.M. Ollinger, S.E. Petersen, and R.L. Buckner. Characterizing the hemodynamic response: effects of presentation rate, sampling procedure, and the possibility of ordering brain activity based on relative timing. *NeuroImage*, 11:735–59, 2000.
- [94] P.J. Magistretti and L. Pellerin. Astrocytes Couple Synaptic Activity to Glucose Utilization in the Brain. *News in Physiological Sciences*, 14(October):177–182, 1999.
- [95] W.J. Malaisse. Anomeric specificity of D-glucose metabolism study in rat and human erythrocytes. *Advances in Biological Chemistry*, 02(01):1–9, 2012.
- [96] F. Malaisse-Lagae and W.J. Malaisse. Anomeric specificity of D-glucose metabolism in rat adipocytes. *European journal of biochemistry / FEBS*, 158(3):663–6, aug 1986.
- [97] W.J. Malaisse and F. Malaisse-Lagae. Anomeric specificity of d-glucose metabolism in rat brain cells. *Brain Research*, 419(1–2):147–155, 1987.
- [98] G. Paxinos, C. Watson, M. Pennisi, and A. Topple. Bregma, lambda and the interaural midpoint in stereotaxic surgery with rats of different sex, strain and weight. *Journal of Neuroscience Methods*, 13(2):139–143, 1985.
- [99] D. Raj, D.P. Paley, A.W. Anderson, R.P. Kennan, and J.C. Gore. A model for susceptibility artefacts from respiration in functional echo-planar magnetic resonance imaging. *Physics in Medicine and Biology*, 45:3809–3820, 2000.
- [100] F. Zhao, T. Zhao, L. Zhou, Q. Wu, and H. Xiaoping. BOLD Study of Stimulation-Induced Neural Activity and Resting- State Connectivity in Medetomidine-Sedated Rat. *NeuroImage*, 39(1):248–260, 2008.
- [101] A.C. Silva and A.P. Koretsky. Laminar specificity of functional MRI onset times during somatosensory stimulation in rat. *Proceedings of the National Academy of Sciences of the United States of America*, 99(23):15182–15187, 2002.
- [102] A.C. Silva, A.P. Koretsky, and J.H. Duyn. Functional MRI impulse response for BOLD and CBV contrast in rat somatosensory cortex. *Magnetic Resonance in Medicine*, 57(6):1110–1118, 2007.
- [103] X. Yu, D. Glen, S. Wang, S. Dodd, Y. Hirano, Z. Saad, R. Reynolds, A.C. Silva, and A.P. Koretsky. Direct imaging of macrovascular and microvascular contributions to BOLD fMRI in layers IV-V of the rat whisker-barrel cortex. *NeuroImage*, 59(2):1451–1460, 2012.

Géraldine PASTOR

Birth date: March 28, 1986

Nationality: French

Present professional position data

Institution: CIC biomaGUNE, MRI platform, Paseo miramón 182, San Sebastián, 20009, Gipuzkoa, Spain

Email: gpastor@cicbiomagune.es

Academic background

2012-2017 PhD student at CIC biomaGUNE institute, Donostia-San Sebastian, Spain

2009 - 2011 Master degree in Chemistry and Catalysis at Université Lyon Claude Bernard, UCBL, Villeurbanne, France

2006 - 2009 Undergraduate degree encompassing Chemistry and Physics, UCBL, Villeurbanne, France

Employment Record

11/2015 Platform specialist MRI

02/2012 - 11/2015 PhD student at the Molecular Imaging group under the supervision of Torsten Reese, Donostia-San Sebastian, Spain

02/2011- 06/2011 Student Master 2 at Institute for materials, Ruhr Universität, Bochum, Germany

04/2010 - 08/2010 Student Master 1 at Functional Nanostructured Materials Department, Ircelyon – CNRS, Villeurbanne, France

Publications

Fast T1 and T2 mapping methods: the zoomed U-FLARE sequence compared with EPI and snapshot-FLASH for abdominal imaging at 11.7 Tesla

Pastor G., Jiménez-González M., Plaza-García S., Beraza M., Reese T., Magnetic Resonance Materials in Physics, Biology and Medicine, 30, pp 299-307, 2017

An experimental procedure to study the diffusion of nanoparticles by MRI

Plaza-García S., Jiménez-González M., Pastor G., Reese T., Ramos-Cabrer P., Science Letters Journal, 5, pp 231-237, 2016

An Iron Oxide Nanocarrier for dsRNA to Target Lymph Nodes and Strongly Activate Cells of the Immune System Cobaleda-Siles M., Henriksen-Lacey M., de Angulo A. R., Bernecker A., Vallejo V. G., Szczupak B., Llop J., Pastor G., Plaza-Garcia S., Jauregui-Osoro M., Meszaros L. K. and Mareque-Rivas J. C., Small, 10, pp 5054-5067, 2014

Hydrogen release through catalysed methanolysis of solid sodium borohydride

J. Hannauer, U. B. Demirci, G. Pastor, C. Geantet, J. M. Herrmann and P. Miele, Energy Environ. Science, 3, pp 1796-1803, 2010